

AD-A036 349

PURDUE UNIV LAFAYETTE IND PROJECT SQUID HEADQUARTERS
AN EXPERIMENTAL INVESTIGATION OF MIXING IN TWO-DIMENSIONAL TURB--ETC(U)
DEC 76 J H KONRAD
SQUID-CIT-8-PU

F/G 20/4

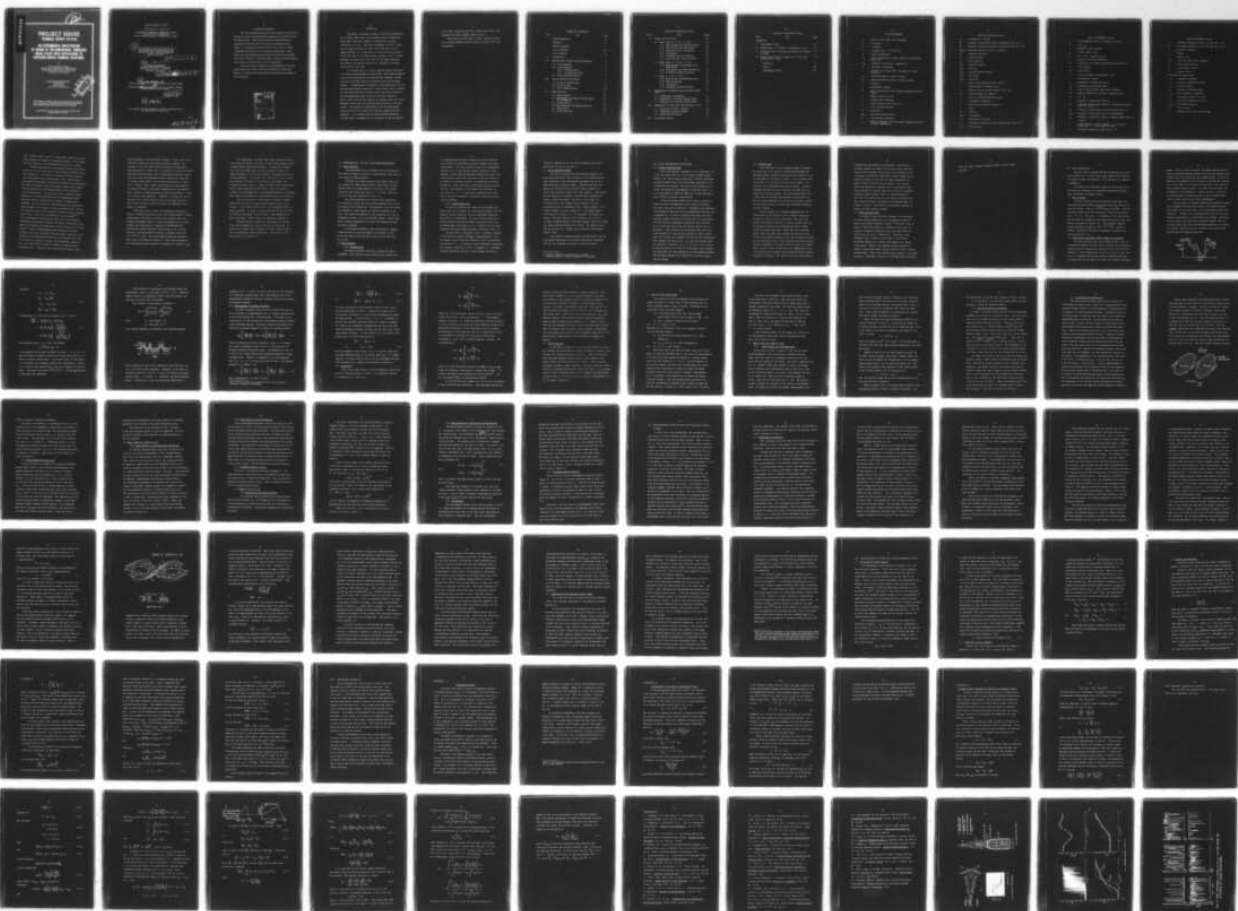
N00014-75-C-1143

NL

UNCLASSIFIED

1 OF 2

AD-A036349



ADA 036349

12

PROJECT SQUID

TECHNICAL REPORT CIT-8-PU

AN EXPERIMENTAL INVESTIGATION OF MIXING IN TWO-DIMENSIONAL TURBULENT SHEAR FLOWS WITH APPLICATIONS TO DIFFUSION-LIMITED CHEMICAL REACTIONS

BY

JOHN HARRISON KONRAD
GRADUATE AERONAUTICAL LABORATORIES
CALIFORNIA INSTITUTE OF TECHNOLOGY
PASADENA, CALIFORNIA

PROJECT SQUID HEADQUARTERS
CHAFFEE HALL
PURDUE UNIVERSITY
WEST LAFAYETTE, INDIANA 47907

DDC
DECEMBER
MAR 3 1977
RECEIVED

Project SQUID is a cooperative program of basic research relating to Jet Propulsion. It is sponsored by the Office of Naval Research and is administered by Purdue University through Contract N00014-75-C-1143, NR-098-038.

This document has been approved for public release and sale;
its distribution is unlimited.

Technical Report CIT-8-PU

P R O J E C T S Q U I D

A COOPERATIVE PROGRAM OF FUNDAMENTAL RESEARCH
AS RELATED TO JET PROPULSION
OFFICE OF NAVAL RESEARCH, DEPARTMENT OF THE NAVY

6 AN EXPERIMENTAL INVESTIGATION OF MIXING
IN TWO-DIMENSIONAL TURBULENT SHEAR FLOWS
WITH APPLICATIONS TO DIFFUSION-LIMITED
CHEMICAL REACTIONS.

7 Technical rept.

10 by

John Harrison/Konrad

Graduate Aeronautical Laboratories
California Institute of Technology
Pasadena, California

14 SQUID ~~14~~ CIT-8-PU

15 Work performed under

Contract No. ~~N00014-75-C-1143~~ NR-098-038 for Project SQUID

and

Contract No. ~~N00014-76-C-0260~~ for the Fluid Dynamics Program,
of the Office of Naval Research

12 131p.

11 December 1976

This document has been approved for public release and sale;
its distribution is unlimited.

1473

403 617.
1B

ACKNOWLEDGMENTS

The work reported here is part of the program of research on turbulent structure and mixing being conducted by the GALCIT Fluid Mechanics Group. I wish to thank Professor Anatol Roshko for suggesting the problem and for discussion and guidance of the research. The generous help and advice of Dr. Garry L. Brown of Adelaide University are also gratefully acknowledged. Many parts of the work benefited directly from ideas which he developed. I also wish to thank Drs. Paul Dimotakis, Coleman duPont Donaldson, G.M. Corcos, and Erik Storm for their suggestions.

This research was supported by the Department of the Navy under Contract No. 8960-1 for Project SQUID and Contract No. N00014-76-C-0260 for the Fluid Dynamics Program of the Office of Naval Research.

ACCESSION for	
YES	White Section <input checked="" type="checkbox"/>
NO	Diff Section <input type="checkbox"/>
UNAWARDED	<input type="checkbox"/>
JUSTIFICATION	
BY	
DISPOSITION/AVAILABILITY NOTES	
DISC.	REPROD. OF FILE
A	

ABSTRACT

The extent of molecular mixing in several two-dimensional free turbulent shear flows was measured using a concentration probe with a frequency response of 100 kHz and a spatial resolution of 0.1 mm. The flows investigated were (i) a shear layer in which the gases on either side of the layer are of unequal density, (ii) a shear layer in which the gases on either side of the layer are of equal density, and (iii) a wake in which the gases on either side of the wake are of unequal densities. The extent of mixing was measured as a function of Reynolds number for the first case.

It was found that at a critical Reynolds number the extent of molecular mixing sharply increased (25%). Power spectral density curves of the concentration time histories also indicated a marked increase in the high frequency fluctuations above this Reynolds number. A shadowgraph investigation of this phenomenon revealed that three-dimensional Taylor-type vortices whose axes of rotation are basically in the flow direction exist in the flow in addition to the two-dimensional large structures previously observed. These Taylor vortices were found to be unstable above the critical Reynolds number and were producing the increase in molecular mixing. The growth and development of the two-dimensional large structures were found to be basically unaffected by this instability. It is proposed that the fully developed turbulence of shear flows is maintained by a combination of the development

of the large structures and of the coupling between the large structures and these unstable Taylor vortices.

These data were also used to predict results for shear flows in which diffusion-limited chemical reactions have been incorporated.

TABLE OF CONTENTS

Part	Title	Page
	Acknowledgements	ii
	Abstract	iii
	Table of Contents	v
	List of Symbols	viii
	List of Figures	xii
I.	Introduction	1
II.	Experimental Facility and Instrumentation	5
	2.1 Flow Apparatus	5
	2.2 Instrumentation	5
	2.2a Pressure Data	5
	2.2b Concentration Data	6
	2.3 Data Acquisition System	7
III.	Data Acquisition Procedures	8
	3.1 Pressure Gradient Data	8
	3.2 Traverse Data	9
	3.3 Power Spectrum Data	10
IV.	Data Reduction	12
	4.1 Mean Profiles	12
	4.2 Intermittency and Mean Profiles within the Turbulence	12
	4.3 "Unmixedness"	14
	4.4 Determination of Dividing Streamline	18
	4.5 Entrainment	19
	4.6 Power Spectrum	21

TABLE OF CONTENTS (Cont'd)

Part	Title	Page
V.	Results and Discussion	22
5.1	Shear Layer ($r = 0.38$, $s = 7.0$)	23
5.1a	Mean Profiles and Spreading Rates	23
5.1b	RMS Concentration Fluctuations	25
5.1c	Intermittency and Entrainment	26
5.1d	Unmixedness	28
5.1e	Probability Density Functions	29
5.1f	Power Spectral Density Curves	30
5.2	Shear Layer ($r = 0.38$, $s = 1.0$)	31
5.2a	Mean Profiles, Intermittency and Entrainment	31
5.2b	Unmixedness and RMS Fluctuations	32
5.2c	Probability Density Functions	32
5.3	Wake ($r = 1.0$, $s = 7.0$)	32
5.3a	Mean Profile and Spreading Rates	32
5.3b	RMS Fluctuations	34
5.3c	Unmixedness	34
5.3d	Probability Density Functions	35
VI.	Photographic Investigation and Reynolds Number Effect	36
6.1	Photographic Investigation	37
6.2	Explanation of Reynolds Number Effect	42
6.3	Implications of Reynolds Number Effect	49
VII.	Applications to Chemically Reacting Shear Flows	52
7.1	Discussion of Toor's Analysis	52
7.2	"Equivalent Laminar Solution"	53
7.3	Results and Discussion	55
VIII.	Concluding Remarks	61

TABLE OF CONTENTS (Cont'd)

Part	Title	Page
Appendices		
A.	Concentration Probe	62
B.	Minimization of the Effect of Hydrostatic Forces	64
C.	Technique Used to Measure the Density of a Mixture of Gases	67
D.	A Derivation of Toor's Analysis for a Chemically Reacting Shear Layer	70
	References	76
	Figures	81
	Photographic Plates	103

LIST OF SYMBOLS

a^*	- speed of sound under sonic conditions
A	- a reactant
B	- a reactant
b	- constant in Eqs. 7.11 and 7.12
C	- molar concentration
C_H	- molar concentration of scalar species in nonreacting shear flow
C_P	- coefficient of pressure in Appendix B.
D	- coefficient of diffusivity
d	- thickness of vorticity layer connecting two large structures
d_1	- spacing between two Taylor vortices
d_2	- spacing between two pairs of Taylor vortices
f	- frequency
g	- gravitational constant
H	- ratio of velocities at two vertically separated points in helium
h	- height of column of fluid
K	- reaction rate coefficient
L	- scale of Taylor vortex (Eq. 6.4)
ℓ	- scale of large structure
M	- mixedness
M_∞	- freestream Mach number
N	- stoichiometric coefficient
N	- ratio of velocities at two vertically separated points in nitrogen (Appendix B)

LIST OF SYMBOLS (Cont'd)

P	- a product of a reaction
\tilde{P}	- integral of normalized product concentration (Eq. 7.7)
$\dot{\tilde{P}}$	- integral of normalized product concentration flux (Eq. 7.8)
$P_i[C_i]$	- probability density function for species i
P_o	- stagnation pressure
p	- static pressure
p_s	- static pressure
Re	- Reynolds number
Re_δ	- $\delta_\omega \Delta U / \nu_{N_2}$
Re_C	- critical Reynolds number
Re_C^+	- above Re_C
Re_C^-	- below Re_C
r	- ratio of freestream velocities (U_2/U_1)
r	- radial length in defining ω and ζ
S	- difference of two Froude numbers (Eq. B.6)
S_i	- Froude number for condition i
s	- ratio of freestream densities (ρ_2/ρ_1)
T	- temperature in Section 4
T	- total time of sample in Section 7
t	- time
U	- velocity
UM	- unmixedness
u'	- fluctuations in velocity
Ve	- entrainment velocity into the turbulent region (Eq. 4.15)
Vp	- probe voltage

LIST OF SYMBOLS (Cont'd)

\bar{v}	- mean tangential velocity in definition of ω and ζ
X	- $C_A - C_B$
x	- distance in flow direction
x_0	- virtual origin of flow
Y	- $(C_A - C_B + C_{Bo})/(C_{Ao} + C_{Bo})$
y	- distance in crossflow direction
y^*	- intersection of dividing streamline and traverse axis
Z_1	- $(C_A + C_P)/C_{Ao}$
Z_2	- $(C_B + C_P)/C_{Bo}$
α	- ratio of entrained reactants (Eq. 7.8)
γ	- intermittency function
γ_1	- probability of finding pure gas 1
γ_2	- probability of finding pure gas 2
γ^*	- ratio of specific heats under sonic conditions
Δh	- distance between two vertically separated points
ΔU	- $U_2 - U_1$
δ	- thickness of shear layer (also δ_w)
δ_C	- thickness of shear layer based on concentration profiles (Eqs. 5.1 and 5.3)
δ_U	- thickness of wake based on velocity profile (Eq. 5.4)
δ_{Vis}	- thickness of shear layer based on shadowgraphs
δ_w	- thickness of shear layer based on velocity profile (Eq. 5.2)
ζ	- vorticity
η	- nondimensional crossflow variable, $\eta = y/(x-x_0)$ for shear layer, $\eta = y/((x-x_0)*\theta)^{\frac{1}{2}}$ for wake
θ	- momentum thickness of wake ($\theta_1 + \theta_2 = \theta$)

LIST OF SYMBOLS (Cont'd)

θ_1	- momentum thickness of side 1 of wake (Eq. 4.10)
θ_2	- momentum thickness of side 2 of wake (Eq. 4.10)
ν	- kinematic viscosity
ρ	- density
ρ_A	- density of air
ρU^*	- mass flux under sonic conditions
Φ	- power spectral density
$\bar{\Omega}$	- mean angular velocity
ω	- angular velocity

subscripts and superscripts

$()_C$	- calibration conditions
$()_I$	- average in nonturbulent region
$()_L$	- laminar solution
$()_T$	- average in turbulent region
$()_T$	- test conditions in Appendix C
$()_1$	- freestream conditions on side 1
$()_2$	- freestream conditions on side 2
$()_0$	- freestream conditions
$(\bar{\quad})$	- time average
$(\quad)'$	- fluctuation away from time average

LIST OF FIGURES

1. Flow Geometry
2. Concentration Probe
3. Traverse Profiles; $r = 0.38$, $s = 7.0$
4. Time Histories of Concentration; $r = 0.38$, $s = 7.0$
5. RMS Fluctuations and Intermittency; $r = 0.38$, $s = 7.0$
6. Unmixedness; $r = 0.38$, $s = 7.0$
7. Probability Density Functions; $r = 0.38$, $s = 7.0$
8. Power Spectral Density Curves; $r = 0.38$, $s = 7.0$
9. Traverse Profiles; $r = 0.38$, $s = 1.0$
10. Time Histories; $r = 0.38$, $s = 1.0$
11. Unmixedness and RMS Fluctuations; $r = 0.38$, $s = 1.0$
12. Probability Density Functions; $r = 0.38$, $s = 1.0$
13. Traverse Profiles; $r = 1.0$, $s = 7.0$
14. Time Histories of Concentration; $r = 1.0$, $s = 7.0$
15. RMS Fluctuations and Intermittency; $r = 1.0$, $s = 7.0$
16. Unmixedness; $r = 1.0$, $s = 7.0$
17. Probability Density Functions; $r = 1.0$, $s = 7.0$
18. Chemically Reacting Shear Layer Profiles; $r = 0.38$,
 $s = 7.0$; Re_C^+
19. Chemically Reacting Shear Layer Profiles; $r = 0.38$,
 $s = 7.0$; Re_C^-
20. Chemically Reacting Shear Layer Profiles; $r = 0.38$,
 $s = 1.0$
21. Chemically Reacting Wake Profiles; $r = 1.0$, $s = 7.0$
22. Integral of Product versus Reynolds Number
23. Integral of Product Flux versus Entrainment Rates Ratio

I. INTRODUCTION

This experimental investigation had its prime motivation from a continuing effort at the California Institute of Technology directed toward the understanding of turbulent shear flows in general and turbulent and molecular mixing in such flows in particular.

Within this general framework, the mixing process in a two-dimensional turbulent shear layer produced by two fluids (both of equal and different densities) flowing parallel to each other at different velocities was studied (see Fig. 1). The aim was to determine the extent of molecular mixing within the layer and, further, to determine what, if any, effect Reynolds number has on the extent of the mixing. (The possibility, in fact probability, of such an effect is evident from Plate 1 which shows shadowgraphs of this flow at various Reynolds numbers. In all photographic plates, the flow direction is from left to right with the high speed side on top. The conditions for all photographs are listed with each plate.)

This flow geometry was chosen for several reasons. First of all, the flow is well documented both for the case when the two fluids are of equal density^{1,2} and for the case where the two fluids are of unequal densities^{3,4}. Secondly, this mixing process is similar to the process by which two reactants are mixed in many continuous-flow, nonpremixed chemical reactors or combustors. However, at present little analytical or experimental data are available which can be used to predict the extent of mixing, and

thus, reaction rates, even for a shear layer, much less for the often complex flow dynamics in practical reactors. For comparison, the mixing in a two-dimensional wake was also studied.

A further and possibly more important aim of this investigation was to shed some light on the continuing discussion among fluid mechanists concerning the fundamental phenomenological laws which govern free turbulent shear flows. Until recently it was thought that such flows consisted of two regions, one turbulent and the other nonturbulent, with the turbulent region being characterized by random three-dimensional motions and the presence of vorticity fluctuations. Viscous forces were continuously propagating these vorticity fluctuations into the nonturbulent region along the interface between the two regions (entrainment by nibbling). By this process the turbulent region was continuously being enlarged at the expense of the nonturbulent region. Due to the recent discovery of large coherent structure in many turbulent shear flows, a new view of turbulence is now emerging⁵⁻¹⁰. This view suggests "that with every shear flow is associated an identifiable characteristic structure and that the development of the flow is controlled by the interactions of these structures with each other¹⁰". Thus, an understanding of the development of these structures and their interactions with each other should give some insight into the actual physical processes in turbulent flows, such as entrainment, transport, mixing, noise production, gustiness, etc., and should lead to improved methods for analyzing and computing them. However, ideas concerning the forms of the

large structures in each flow differ greatly. In fact, this view of turbulence itself is far from being generally accepted. For example, it has been stated that the basically two-dimensional large structure of a shear layer as reported by Brown and Roshko³ and others cannot undergo vortex stretching and therefore cannot form part of the fully-developed energy cascade from mean flow to smallest eddies which is the essential characteristic of turbulence. Further, these isolated large structures when subjected to small perturbations would deform indefinitely by self-induction, thus, leading to a rapid breakdown to three-dimensionality. These are certainly valid arguments. Therefore, a further aim of this research was to reconcile these views of the large structure in shear flows and thus, to add to the basic understanding of the nature of turbulence.

With these goals in mind, the investigation proceeded as follows. Using an improved version of the Brown-Rebollo¹¹ concentration probe, the extent of mixing in the turbulent shear layer produced by parallel streams of high speed helium and low speed nitrogen was determined as a function of lateral position (y) and Reynolds number (Reynolds number based on ΔU , vorticity thickness, and the kinematic viscosity of nitrogen varied from 0.3×10^4 to 7×10^4). The experimental facility and instrumentation used are discussed in Section 2. The actual procedures for data acquisition and reduction are discussed in Sections 3 and 4.

For comparison, two other shear flows were also studied. In one flow, the extent of mixing in a shear layer between streams of equal density fluids was measured. For this flow, nitrogen was used as the high speed gas and a mixture of argon and helium arranged to have the same density as nitrogen was used as the low speed gas. In the other flow, the velocity of the nitrogen was adjusted to be equal to the velocity of the helium, thus reducing the shear layer to a wake, the wake of the splitter plate which initially separated the two fluids. Thus, the extent of mixing in an inhomogeneous, two-dimensional wake was investigated. The results and comparison of these three cases are in Section 5.

These measurements of the extent of mixing in turbulent shear flows revealed a strong Reynolds number effect on the mixing. It was felt that this was due to an instability within the large structures. In order to confirm this idea and also to study the three-dimensionality of these flows, a shadowgraph investigation was made. These results are presented in Section 6.

Although the flows studied are nonreacting, the results were used to predict the reaction rates for an interesting and useful case in which flows containing chemically reactive species can be successfully studied analytically. The results for the three cases are in Section 7.

II. EXPERIMENTAL FACILITY AND INSTRUMENTATION

2.1 Flow Apparatus

The experiments were performed in the Brown-Roshko³ flow facility designed to produce a turbulent shear flow between two streams of different gases.

Basically the facility consists of two supply lines, each one coming from eight 2000psi bottles, which supply two gas streams that are brought together at the exit of two nozzles which have been contracted down to 1" x 4" each. The overall size of the test section is 2" x 4" x 12".

The settling chambers and screens in the supply lines are sufficient to reduce the free stream turbulence level in the test section to less than 0.5%. The sidewalls of the test section are adjustable to help remove any pressure gradients in the flow. The entire test chamber can be pressurized up to ten atmospheres in order to vary the Reynolds number. Steady state flow is usually established in less than 500 milliseconds after the flow is initiated.

A traversing mechanism, which incorporates a digitally controlled motor to step the probes in increments of .001", moves the probes across the test section at up to 500 steps per second.

2.2 Instrumentation

2.2a Pressure Data

Two types of pressure data were required for this investigation: static pressure scans along the test section used

in minimizing the pressure gradients in the flow direction (see Section 3.1) and dynamic pressure profiles across the mixing layer. The static pressure scans were accomplished with the use of a fast pressure scanner (Scanivalve, type-W1260), a device which sequentially communicates each of the static pressure ports along both sides of the test section to the input of a pressure transducer (a Datametrics electronic manometer, 1014A, and Barocel differential pressure sensor, 511-10). The reference for the sensor was generally the static port at $x = 1''$. A pitot tube, connected to the same type of pressure transducer, was used to obtain the dynamic pressure profiles.

2.2b Concentration Data

In order to determine the extent of mixing within the shear layer and to compute the mean velocity profiles from the dynamic pressure profiles, the local composition within the layer had to be determined. For these measurements an improved version of the Brown-Rebollo aspirating probe¹¹ was developed, under the guidance of G.L. Brown, to meet the high frequency and small spatial resolution requirements (Fig. 2a).

The new probe is estimated to have a frequency response of 100 kHz and a spatial resolution of approximately 0.1mm. The signal to noise ratio was sufficient to detect concentration fluctuations of 1%. A complete account of the probe construction and response estimations is given in Appendix A. A standard constant temperature hot-wire circuit designed and built at

Caltech by Anthony Perry* and Brian Cantwell** was used to operate the hot wire in the probe.

2.3 Data Acquisition System

The short run times (the Brown-Roshko apparatus is a blow-down type facility with run times of 2-6 seconds) and the high frequencies of the experiments necessitated the use of a high-speed data acquisition system. Therefore, all data were taken (and reduced) with the GALCIT mobile computer controlled data acquisition system (the "Solo System"). This system has the capability of computer controlled data acquisition, reduction, storage and output. The heart of the system is a Hewlett-Packard 2100 computer (32K memory). The data acquisition itself is accomplished with a sixteen channel, 16 bit analog-to-digital converter capable of 5×10^5 single channel conversions per second or 4×10^5 sequential conversions per second. The data, before or after reduction, can be stored on either a Hewlett-Packard read/write magnetic tape deck, 7970E, or a Hewlett-Packard storage disc, 7901A. The output devices with the system are a Teletype and a Hewlett-Packard digital plotter, 7210A.

The required interfacing between the Solo System and the experimental apparatus will be briefly discussed in connection with the data acquisition procedures in the next section.

* Reader, University of Melbourne, Australia

** Research Fellow, California Institute of Technology

III. DATA ACQUISITION PROCEDURES

3.1 Pressure Gradient Data

One of the boundary conditions for the experiments was to have the shear flows in a zero pressure gradient region. However, any vertical fluid column has a "natural" hydrostatic pressure gradient equal to the fluid density multiplied by the gravitational acceleration. The effect of this gradient can of course be neglected in experiments in which the fluid is air or in experiments in which all fluids are of equal densities if care is taken in pressure measurements.

In this experiment, which had, in effect, a column of helium in direct communication with a column of nitrogen, this effect could not be neglected or eliminated, only minimized. (A discussion of this effect and the minimization procedure are in Appendix B.) In order to minimize this effect, the static pressure gradient along the test section had to be determined. This was done by sequentially sampling the static pressure ports on the side walls of the test section with the use of a Scanivalve. After allowing 250 milliseconds after each step of the Scanivalve for the pressure reading to reach a steady state, the pressure was sampled 1000 times in 250 milliseconds. The readings were then averaged for each port and the gradient calculated. The ports at $x = 2''$, $3''$, $4''$, $5''$, $6''$, $7''$ and $8''$ on one wall and at $x = 4''$ and $8''$ on the other were sampled. The side walls were then adjusted to give the optimal gradient. The side wall positions were different for each free stream velocity setting.

3.2 Traverse Data

The stated goal of determining the extent of mixing in the shear layer as a function of cross-stream position and Reynolds number required measuring the time histories of the concentrations of the gases at various x and y locations within the layer for a variety of free-stream conditions. The procedure for accomplishing this was as follows. The tank (ambient) pressure and the free-stream velocities were adjusted to the desired settings. The concentration probe and a pitot tube both mounted approximately one inch apart on the traversing mechanism were placed at a selected x station and then moved across the shear layer alternately sampling and then stepping.

The two probes were sampled sequentially for 150 milliseconds at each point at a rate of 80,000 readings per second for a total of 12,000 data points. They were then stepped .075 inches to the next y location (stepping rate was 0.5 inches per second for 150 milliseconds) where another 12,000 data points were taken. After each data acquisition period, while the probes were moving, the data were transferred from computer memory to disc, thus freeing the memory for the next batch of data. The six second run time limitation allowed a maximum of 21 points across the layer (1.5 inches). After each six second run, the data were automatically transferred from disc to magnetic tape and then back into computer memory for reduction. The reduced data were then stored on

magnetic tape and displayed on the plotter. Each traverse was then repeated four times and the mean values from each traverse were averaged. This process was repeated for four x locations, two different free-stream velocity settings and at ambient pressures of one, four and eight atmospheres for a total of nearly 25 million raw data points. The electronic interfacing between the computer and the experimental apparatus consisted of a master clock (set at the data acquisition frequency, usually 80 kHz) which was gated alternately to first allow the 12,000 pulses to go to the A/D converter and then divided (to 500 Hz) and gated to the stepping motor for, usually, 75 pulses. This allowed for alternately sampling at 80 kHz and then stepping at 500 Hz.

3.3 Power Spectrum Data

In order to reduce the time histories of concentration to power spectral density curves in a reasonable amount of time, a fast fourier transform routine^{12, 13} was used. This required 2^n data points taken at a frequency at least twice the maximum frequency of interest (always less than 25 kHz except for one run at $U_1 = 3000 \text{ cm/sec}$). Therefore, a data acquisition rate of 50 kHz was used with a cut-off filter, Krohn-Hite 3202A, set at 25 kHz on the output of the concentration probe. However, the computer memory limited the number of data points which could be reduced to 4096 ($\sim 80 \text{ msec}$ sampling time). This is not sufficient time, however, to give good resolution. Therefore, records of 16,384 data points were taken

(328 msec long), reduced in groups of 4096, and the results averaged.

IV. DATA REDUCTION

The first step in reducing the data acquired by the preceding procedures was to convert the voltage output of the concentration probe to molar concentrations. This procedure is explained in Appendix A.

Discussed in the following sections are the various ways that these time histories of concentration and dynamic pressure were converted to meaningful results.

4.1 Mean Profiles

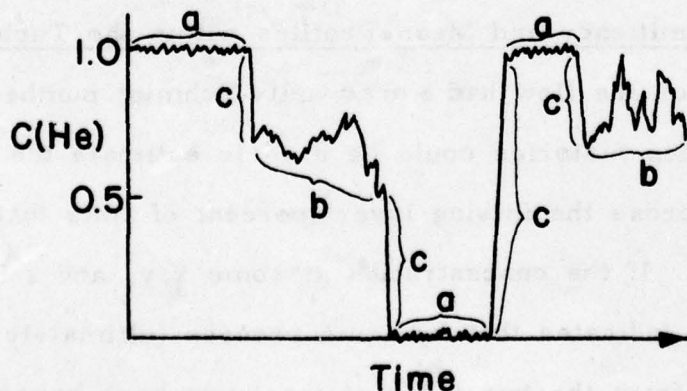
The first reduction process performed on the data was to ensemble average the data for each point across the mixing layer from each probe. This gave $\overline{\rho U^2}(y)/\rho_1 U_1^2$ and $\bar{C}(y)$. The concentration profiles were then converted to mean density profiles ($\bar{\rho}/\rho_1 = \bar{C} + (1 - \bar{C}) \rho_2/\rho_1$). An estimation of the velocity profile was found by dividing the mean dynamic pressure by the mean density and taking the square root. This procedure neglects several fluctuation correlations ($\overline{\rho'u'}$, $\overline{u'^2}$, $\overline{\rho'u'^2}$). However, Rebollo⁴ showed that the effect is negligible (at least for the case $\rho_2 U_2^2/\rho_1 U_1^2 = 1$).

4.2 Intermittency and Mean Profiles within the Turbulence

Since the flow had a near unity Schmidt number (ν/D), the concentration histories could be used to estimate the intermittency function across the mixing layer (percent of time that the fluid is turbulent). If the concentration at some x, y , and t is other than 0 or 1, it indicates that by some process (ultimately diffusion) the fluids from the two sides of the layer have become molecularly

mixed. However, since momentum will diffuse approximately the same as molecules (Schmidt number unity) this also indicates that vorticity will have diffused into the sampled region. If this is an indication of turbulence, then the percent of time that the concentration is other than 1 or 0 will give an estimation of the intermittency function across the layer. In actual fact three curves can be defined: (1) the probability of finding pure gas 1 (within 3%), (2) the probability of finding pure gas 2, and (3) intermittency (which is unity minus the two above probabilities).

This procedure of defining turbulent and nonturbulent regions also facilitated estimating mean values in the turbulent regions (subscripted T) and mean values in the nonturbulent regions (subscripted I). Actually, the concentration data were put into three different classifications as illustrated in the drawing. Data from (a) were used to find means in nonturbulent regions, data from (b) were used to find mean and fluctuating quantities in the turbulent regions, and data from (a), (b) and (c) were used to find overall mean and fluctuating quantities.



Thus, the following quantities were measured or calculated:

$\overline{C}(y)$ - ensemble average of concentration histories at each y location.

$\overline{\rho U^2}(y)/\rho_1 U_1^2$ - ensemble average of dynamic pressure histories at each y location.

$\overline{U}(y)/U_1$ - mean velocity profiles.

$\overline{C}(y)_I$ - average of concentration data in the nonturbulent regions (data within 3% of 1 or 0).

$\overline{C}(y)_T$ - average of concentration data in the turbulent regions.

$\gamma_1(y)$ - probability of finding pure gas 1 (within 3%).

$\gamma_2(y)$ - probability of finding pure gas 2

$\gamma(y)$ - Intermittency ($1 - \gamma_1 - \gamma_2$)

$()_T$ - various fluctuating quantities calculated from data in the turbulence (as explained above). These quantities will be described in the next section.

4.3 "Unmixedness"

One of the goals of this investigation, to determine the extent of mixing in a turbulent shear layer, required a "yardstick" with which to measure the extent of mixing. The definition of one such "yardstick" is $\sqrt{C'^2}$, the RMS fluctuation of the concentration, where

$$C' = C - \overline{C}. \quad 4.1$$

However, this quantity does not have a well-defined upper bound and, if the gases in the layer are perfectly unmixed (concentration data are always either 1 or 0), different values of \overline{C}

give different values of $\sqrt{C'^2}$. However, for comparison with other investigations, this quantity, along with $\left(\sqrt{C'^2}\right)_T$, were calculated where $C' = C_T - \bar{C}_T$, C_T being concentration data within the turbulence.

A more meaningful measure of the extent of mixing comes from chemical reaction rate estimations.* For the irreversible reaction



where A and B are reactants and P is the product, the following conservation equations can be derived¹⁴:

$$\frac{D C_A}{D t} = - K_1(T) C_A C_B \quad 4.3$$

$$\frac{D C_B}{D t} = - K_2(T) C_A C_B \quad 4.4$$

where $\frac{D}{D t}$ is the substantial derivative, K_i is a reaction rate, C_i is the concentration of species i, and T is temperature. This approach can be related to the present investigation if it is supposed that A is diluted in the helium and B in the nitrogen.

Then:

$$C_A = \bar{C}_A + C'_A = C_{A0} (C_{He}) = C_{A0} (\bar{C}_{He} + C'_{He}) \quad 4.5$$

and

$$C_B = \bar{C}_B + C'_B = C_{B0} (1 - C_{He}) = C_{B0} (1 - \bar{C}_{He} - C'_{He}),$$

where C_{i0} is the free stream concentration of species i.

* This measure of mixedness was suggested by Coleman duPont Donaldson.

Therefore,

$$C'_A = C_{Ao} C'_{He} ,$$

$$\overline{C}_A = C_{Ao} \overline{C}_{He} ,$$

$$C'_B = - C_{Bo} C'_{He} ,$$

$$\overline{C}_B = C_{Bo} (1 - \overline{C}_{He})$$

4.6

Combining Eq. 4.6 with the time average of Eq. 4.3 gives

$$\begin{aligned} \frac{D\overline{C}_A}{Dt} &= - \overline{K}_1 \left(\overline{C}_A \overline{C}_B + \overline{C'_A C'_B} \right) \\ &= - \overline{K}_1 \overline{C}_A \overline{C}_B \left(1 + \frac{\overline{C'_A C'_B}}{\overline{C}_A \overline{C}_B} \right) \\ &= - \overline{K}_1 \overline{C}_A \overline{C}_B \left(1 - \frac{\overline{C'^2_{He}}}{\overline{C}_{He} (1 - \overline{C}_{He})} \right). \end{aligned}$$

4.7

This assumes that $K'_i = 0$. Thus, the quantity

$$1 - \overline{C'^2} / \overline{C} (1 - \overline{C}) = M$$

is an indication of how well the fluids are mixed. If it is 1 ($C' \equiv 0$) then the fluids are perfectly mixed and the mean values (\overline{C}_i) can be used to estimate reaction rates. On the other hand, if this quantity is 0, the fluids are completely unmixed (the concentration is always 0 or 1) and the mean values give a very poor estimation of reaction rates. Therefore, the quantity $\overline{C'^2} / (1 - \overline{C}) \overline{C} = 1 - M$ (the unmixedness of the fluids) was calculated.

This definition of unmixedness will obviously amplify the experimental "noise" in measuring C as $\bar{C} \rightarrow 1$ or 0 . Therefore, another measure of unmixedness which avoids this problem and still has the proper limits was defined.

This measure of unmixedness is defined as

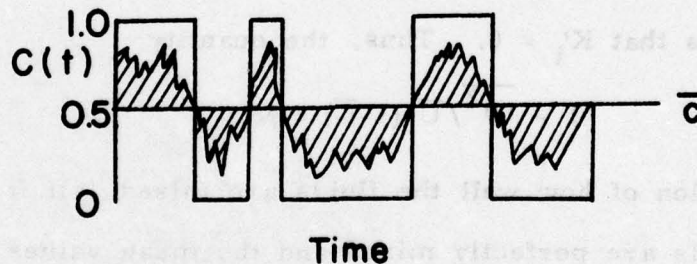
$$UM = \frac{t_1 \int_{t_1} (C - \bar{C}) dt_1 + t_2 \int_{t_2} (\bar{C} - C) dt_2}{t_1 \int_{t_1} (1 - \bar{C}) dt_1 + t_2 \int_{t_2} (\bar{C}) dt_2} \quad 4.8$$

where

t_1 = time when $C > \bar{C}$

t_2 = time when $C < \bar{C}$.

This integral definition is illustrated in the following drawing.



UM is actually the sum of the crosshatched areas divided by the sum of the areas of the rectangles. Obviously, if the fluids are perfectly mixed ($C(t) = \bar{C}$) $UM = 0$, and if the fluids are perfectly unmixed ($C(t) = 1$ or 0), $UM = 1$. Therefore, UM has the proper limits. Furthermore, it does not present any experimental

problems for $\bar{C} \rightarrow 1$ or 0.* As will be seen later in the discussion of a chemically reacting shear layer, this definition also has an interpretation relating the amount of product formed to the amounts of reactants entrained.

4.4 Determination of Dividing Streamline

In order to properly show all of the traverses for the various x locations in nondimensional form, a common reference point for all of the profiles has to be determined. This point is commonly taken to be the intersection of the dividing streamline with the y -axis of the data traverse. This point is found by combining the continuity and momentum equations to derive the following equation:

$$\frac{d}{dx} \int_{y^*}^{\infty} \frac{\bar{\rho}\bar{U}}{\rho_1 \bar{U}_1} \left(\frac{\bar{U}}{\bar{U}_1} - 1 \right) dy = \frac{d}{dx} \int_{-\infty}^{y^*} \frac{\bar{\rho}\bar{U}}{\rho_1 \bar{U}_1} \left(\frac{U_2}{\bar{U}_1} - \frac{\bar{U}}{\bar{U}_1} \right) dy \quad 4.9$$

where $()_1$ denotes free stream conditions on side 1, $()_2$ denotes free stream conditions on side 2 and y^* is the location of the dividing streamline intersection point. The application of Eq. 4.9 to find y^* for a shear layer having similarity properties is rather straightforward. However, in applying it to an inhomogeneous wake ($U_2 = U_1$, $\rho_2 \neq \rho_1$) more care must be taken. One possible approach is as follows. Let

$$\theta_1 = \int_{y^*}^{\infty} \frac{\bar{\rho}\bar{U}}{\rho_1 \bar{U}_1} \left(1 - \frac{\bar{U}}{\bar{U}_1} \right) dy, \quad \theta_2 = \int_{-\infty}^{y^*} \frac{\bar{\rho}\bar{U}}{\rho_1 \bar{U}_2} \left(1 - \frac{\bar{U}}{\bar{U}_2} \right) dy. \quad 4.10$$

Then, combining Eqs. 4.9 and 4.10 gives

* Ideas similar to these were suggested by Dr. Erik Storm of Lawrence Livermore Laboratory.

$$-\frac{d}{dx} \theta_1 = \left(\frac{U_1}{U_2}\right)^2 \frac{d}{dx} \theta_2, \quad 4.11$$

or

$$\frac{d}{dx} \theta_1 = -\frac{d}{dx} \theta_2, \quad (U_2 = U_1) \quad 4.12$$

θ_1 can be interpreted as the momentum defect on side 1 and θ_2 the momentum defect on side 2. Equation 4.12 states that if θ_1 increases (decreases), θ_2 must decrease (increase) by exactly the same amount. In other words, $\theta_1 + \theta_2 = \theta = \text{constant}$, as must be the case (the momentum defect for a wake is constant). If θ_1 and θ_2 are continuously changing, then one side of the wake must be continuously gaining momentum and the other side continuously losing momentum. As this situation can not continue indefinitely, Eq. 4.12 must be interpreted as

$$\frac{d}{dx} \theta_1 = -\frac{d}{dx} \theta_2 \equiv 0$$

$$\text{or} \quad \theta_1/\theta_2 = \text{const.} \quad 4.13$$

Since an estimate of the constant in Eq. 4.13 can be made from the initial boundary layers on the splitter plate, Eq. 4.13 together with Eq. 4.10 can be used to find y^* for the inhomogeneous wake. (This estimation of y^* neglects all fluctuation correlations.)

4.5 Entrainment

With today's large structure view of turbulence, entrainment becomes a difficult quantity to define. The traditional definition of entrainment for a shear layer,

$$\begin{aligned}
 Ve_1 &= \frac{d}{dx} \int_{y^*}^{y_1} \frac{\overline{\rho U}}{\rho_1} (y) dy \\
 Ve_2 &= \frac{d}{dx} \int_{y_2}^{y^*} \frac{\overline{\rho U}}{\rho_1} (y) dy
 \end{aligned}
 \tag{4.14}$$

where Ve_i is the entrainment velocity on side i and y_i is an arbitrarily chosen limit, raises two questions. 1. How should y_i logically be chosen? 2. Should the fluid which is within the bound of y_1 and y_2 , but has not yet become part of the turbulence, be part of the entrainment calculation? If the entrainment rate is to provide information as to the proportions and rate in which the two fluids on either side are entering the mixing layer and becoming "entangled" or mixed, then a suitable definition is needed. One such definition is

$$\begin{aligned}
 Ve_1 &= \frac{d}{dx} \int_{y^*}^{\infty} \gamma(y) \frac{(\overline{\rho U})_T}{\rho_1} dy \\
 Ve_2 &= \frac{d}{dx} \int_{-\infty}^{y^*} \gamma(y) \frac{(\overline{\rho U})_T}{\rho_1} dy
 \end{aligned}
 \tag{4.15}$$

where $\gamma(y)$ is the intermittency function and $(\overline{\rho U})_T$ is the average within the turbulence of the product of density and velocity. The complete derivation of this definition is given by Brown¹⁵. For this investigation $(\overline{\rho U})_T$ was approximated by $\bar{\rho}_T \bar{U}$.

It is not entirely clear whether Eq. 4.14 or Eq. 4.15 should be used to describe the entrainment. Both definitions describe the

amount of fluid which has crossed an arbitrary boundary. The limit used in Equation 4.14 is an overall boundary of the shear layer based on mean quantities and the limit used in Equation 4.15 is the boundary between the turbulent and nonturbulent regions. However, for clarity, the quantities calculated using Equation 4.15 will be referred to simply as the entrainment rates throughout the rest of this work. This is done since these rates are more meaningful in relation to the chemical analysis presented in Section 7 than the rates calculated using Equation 4.14. Further, entrainment into the turbulence is more in accord with the large structure view of turbulence than is simply a gross measure of entrainment. The normalization was chosen so that entrainment rates can be compared directly without having to take differences in density into account.

4.6 Power Spectrum

As discussed in Section 3.3, four records of 4096 concentration readings each were taken at a rate of 50 kHz for various x and y locations and various free-stream velocities. These four records, after being put through a Hanning window, were reduced to four spectra using a fast fourier transform routine. These were then averaged to produce a single spectrum. This curve was then further reduced by averaging adjacent points within the curve. The averaging window (number of adjacent points to be averaged) was exponentially increased from one for the low frequency points to approximately 30 for the highest frequencies.

V. RESULTS AND DISCUSSION

The initial part of this investigation was to measure the extent of mixing for a shear layer of fixed parameters for as wide a Reynolds number range as possible. Following are the parameters which were kept constant:

- (a) A two-dimensional shear layer between high-speed helium and low-speed nitrogen ($s = \frac{\rho_2}{\rho_1} = 7.0$)
- (b) $p(x) = \text{constant}$ (p being static pressure)
- and (c) $r = U_2/U_1 = 0.38$.

Following are the parameters which were changed in order to vary the Reynolds number:

- (a) U_1 (and thus U_2): 1000, 2000 and, for $P_0 = 1 \text{ atm.}$, 3000 cm/sec.
- (b) P_0 (ρ_1 and ρ_2): 1, 4 and 8 atmospheres
- and (c) x : 2, 3, 4 and 5 inches.

After these data were taken, two other cases were investigated. In order to determine what, if any, effect the inhomogeneity of the flow has on the mixing, the mixing in a constant density shear layer was measured ($r = 0.38$, $s = 1.0$) and compared to the previous results. For this case, the high-speed gas was nitrogen and the low-speed gas a mixture of argon and helium arranged to have the same density as nitrogen. (See Appendix C for a discussion of the method used to measure the density of the gas mixture.) The concentration probe was able to resolve the concentration of nitrogen in this mixture to within 4%. For this case $P_0 = 4 \text{ atm.}$, $U_1 = 1000 \text{ cm/sec.}$ and $x = 4 \text{ inches.}$

The third case investigated was a wake, but not a wake in the usual sense of the word. This case was actually the investigation of the wake produced by the splitter plate which initially separates the two fluids. The flow was obtained simply by settling U_2 equal to U_1 ($r = 1.0$, $s = 7.0$). This case was investigated to compare the mixing in a wake to that of a shear layer. Since the structure of a wake is quite different from that of a shear layer, the mixing process may be different. For this case $U_1 = U_2 = 2000\text{cm/sec.}$, $P_o = 1\text{ atm.}$, and $x = 2, 3, 4, 5$ and 6 inches.

In the following sections are the results for, first of all, the inhomogeneous shear layer, then the homogeneous shear layer, and, finally, the wake.

5.1 Shear Layer ($r = 0.38$, $s = 7.0$)

5.1a Mean Profiles and Spreading Rates

First of all, in order to acquire a "feel" for the extent of the fluctuations in the concentration of helium within the shear layer, the probe was continuously traversed across the layer from the nitrogen to the helium. The result is shown in Figure 3a. Similar results were obtained by Brown and Roshko. Several questions were immediately raised by this curve. Why do the fluctuations appear to be larger on the nitrogen side than on the helium side? Why does the concentration appear to spend a large amount of the time near $C = 0.8$? The answers to these questions are discussed in the section on entrainment rates. As observed by Brown and Roshko, shadowgraphs of the

flow at various Reynolds numbers (Plate 1a, c, e, g) show that large structures exist in the shear layer and these structures appear to be entraining the pure free-stream fluid in such a way that it can exist in an unmixed state across the entire layer. Thus, large fluctuations in concentration are expected. This will be further discussed in Section 6.

Figure 3b shows the mean concentration profiles as described in Sections 3.2 and 4.2. A characteristic length can be defined, and thus a growth rate can be found, from this curve. If the "edges" of the layer are defined as the points $\bar{C} = 0.1$ and $\bar{C} = 0.9$ then

$$\delta_c = 0.147 (x - x_0) \quad 5.1$$

Brown and Roshko used $\bar{C} = 0.01$ and $\bar{C} = 0.99$ as the edges of the shear layer and, thus, their measured growth rate was somewhat larger.

Figures 3c and 3d are the mean dynamic pressure and the mean velocity profiles, respectively. Another length, one which can also be defined for homogeneous as well as inhomogeneous shear layers, can be found from Figure 3d. This length is the maximum slope thickness of the velocity profile or the vorticity thickness and is measured to be

$$\delta_w = 0.119 (x - x_0) \quad 5.2$$

This characteristic length will be used throughout the rest of this work and will be labeled δ .

Shown in Figure 4 are a few typical time histories of the concentration taken at various η locations in the layer. t is

the approximate size of the large structure for that x location.

It is important to note that these mean profiles were unaffected by varying the Reynolds number.

5.1b RMS Concentration Fluctuations

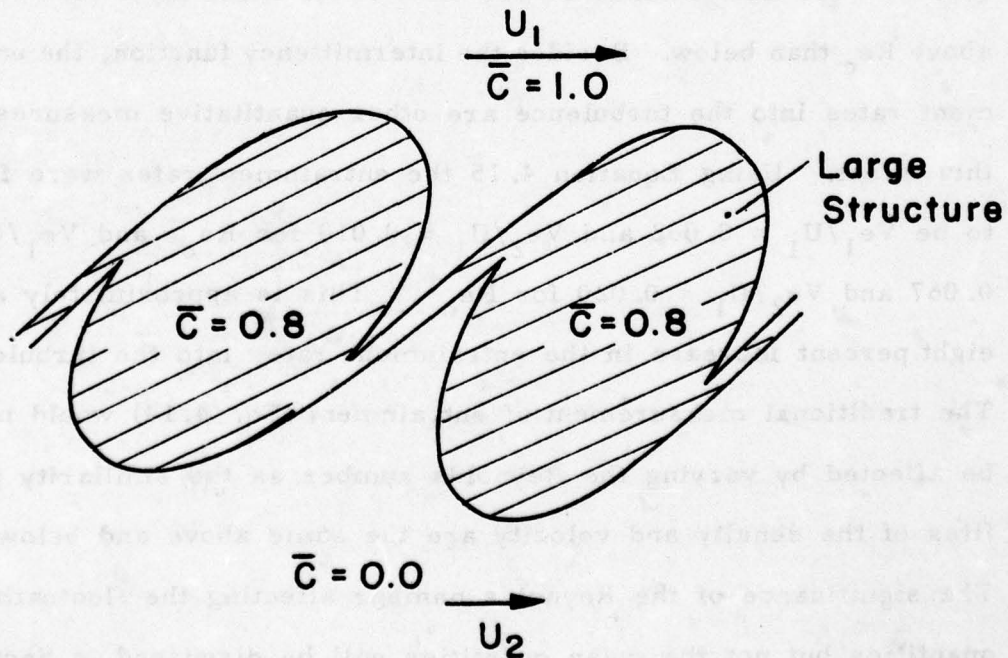
A rather surprising result was found when the fluctuating quantities were compared on similarity plots. Two curves were found for each quantity plotted, one for the profiles taken at Reynolds numbers less than 2×10^4 ($Re = \delta \Delta U / \nu_{N_2}$) and one for the profiles taken at Reynolds numbers greater than 2×10^4 . This Reynolds number will henceforth be called the "critical" Reynolds number (Re_c). Data curves above Re_c will be labeled Re_c^+ and those below will be labeled Re_c^- . This effect is shown for $\sqrt{C'^2}$ and $\left(\sqrt{C'^2}\right)_T$ in Figures 5a and b. The Re_c^- data are shown by the dashed curves. The fluctuations in concentration are always less above the critical Reynolds number than below. Data taken near Re_c fell between the two curves.

One thing to be noted in Figure 5a is that the nitrogen side appears to have a higher degree of fluctuations than the helium side. This will be partially explained in the discussion on entrainment. Two things should be noted about Figure 5b: the profile is flatter than that of Figure 5a and the Reynolds number effect is more pronounced for the turbulent zone calculation than for the calculation for the entire data record (hereafter called the normal calculation). These observations will be useful in determining why there is a Reynolds number effect in the first place. This will be discussed in Section 6.

5.1c Intermittency and Entrainment

This same Reynolds number effect can be observed in the intermittency similarity curves. Figure 5c-1 is the probability of finding pure nitrogen, Figure 5c-2 is the probability of finding pure helium and Figure 5c-3 is the intermittency function. The dashed curves are for the Re_c^- data. For the Re_c^+ data, the scatter may be judged from the plotted points; for all the Re_c^- data the scatter was smaller by about one half. It can be seen from Figure 5c-1 and 2 that below Re_c , the probability of finding pure gas is higher across the entire shear layer. Thus the intermittency function for Re_c^- is more narrow and reaches a lower maximum value than for Re_c^+ . Therefore, the pure fluid which is being engulfed into the shear layer is being entrained into the turbulence (being mixed molecularly) faster above Re_c than below. Pure fluid extends across most of the shear layer less often above Re_c than below. Besides the intermittency function, the entrainment rates into the turbulence are other quantitative measures of this effect. Using Equation 4.15 the entrainment rates were found to be $Ve_1/U_1 = 0.062$ and $Ve_2/U_1 = 0.019$ for Re_c^- and $Ve_1/U_1 = 0.067$ and $Ve_2/U_1 = 0.020$ for Re_c^+ . This is approximately an eight percent increase in the entrainment rates into the turbulence. The traditional measurement of entrainment (Eq. 4.14) would not be affected by varying the Reynolds number as the similarity profiles of the density and velocity are the same above and below Re_c . The significance of the Reynolds number affecting the fluctuating quantities but not the mean quantities will be discussed in Section 6.

Besides these increases in the entrainment rates, another important point to note is that over three times as much helium is being entrained as nitrogen. This fact accounts for several of the points brought out in earlier discussion. Due to this difference in entrainment rates, the large structures will have a mean concentration near 0.8. Thus the output from the concentration probe will, for a large percentage of the time, be near this value (as seen in Figs. 3a, 3b and 4). This also partially explains why the fluctuations are larger on the nitrogen side. On that side, as the large structures pass by the probe (see drawing) the concentration will fluctuate from approximately 0.8 to 0.0. On the helium side, however, the concentration will fluctuate from 0.8 to 1.0. This only partially explains the larger



fluctuations on the nitrogen side because, as can be seen from Fig. 5b, the turbulent zone calculations still give larger fluctuations on the nitrogen side than on the helium side, although the difference is not as great as in the normal calculations (Fig. 5a).

5.1d Unmixedness

Figure 6 shows the results of the unmixedness calculations. Figure 6a shows the results for the integral definition (Eq. 4.8) and Figure 6c shows the results for the chemical reaction rate definition. Figures 6b and 6d are the turbulent zone calculations for the unmixedness. As with the RMS calculations, the unmixedness values are always less above Re_c than below. Also, lower values are obtained and the Reynolds number effect is more pronounced for the turbulent zone calculations than for the normal calculations.

Several qualitative statements can be made from the data shown on these curves. Firstly, from Figure 6a, fluid which has been entrained in the usual sense (Eq. 4.14) is still in a relatively high state of unmixedness, has not become mixed on the molecular level, especially on the nitrogen side and below Re_c . If the nitrogen and helium were reactive with each other, much of the fluid within the layer would not react at the point at which it has been entrained; it would "swirl" around within the layer without having the opportunity to mix on the molecular level, and thus react. Of course, all of the fluid which is entrained will eventually react, but only a small portion of the total at any x location will have been reacted. Even the fluid

which has been entrained into the turbulence is in a high state of unmixedness (Fig. 6b).

Since information about the degree of unmixedness is not usually known,

$$\frac{DC_A}{Dt} = -\bar{K}_A \bar{C}_A \bar{C}_B$$

is sometimes used to calculate reaction rates instead of Eq. 4.7. It can be seen from Figure 6c that this calculation would be in error by at least 20%.

These qualitative results will be made more quantitative in Section 7 where these results are used to predict amounts of product in a chemically reacting shear layer.

5.1e Probability Density Function

A useful way of presenting the data in the time histories of the concentration is with probability density functions (P.D.F.'s). P.D.F.'s are simply graphs of the percentage of time that the concentration spends between two limits (normalized to give unity area under the curve). Shown in Figure 7 are the P.D.F.'s for various η locations across the layer. All values above 8.0 are not shown. It is rather interesting to note that all of the results concerning concentration presented thus far can be calculated from the P.D.F.'s. That is one of the reasons why at present a considerable amount of effort is being spent on trying to model the P.D.F.'s of scalar quantities in turbulent shear flows. One popular practice is to model them with a Gaussian distribution. As can be seen, at no point in this case do the

P.D.F.'s approach a Gaussian distribution.

The effect of the difference in entrainment rates can again easily be seen. The probability of finding the concentration between 0.8 and 0.9 is relatively high. The probability of finding pure gas across the layer is shown by the spikes on the ends of the curves. This particular set of curves is the average of four runs at $x = 4$ inches, $U_1 = 1000\text{cm/sec}$ and $P_o = 4$ atms. No attempt was made to average all of the P.D.F.'s above Re_c and all below Re_c because each set of runs measured the P.D.F.'s for different η locations. These P.D.F.'s will be used extensively in Section 7.

5.1f Power Spectral Density Curves

In order to gain more insight into the observed Reynolds number effect, spectra of the concentration fluctuations were obtained both above and below Re_c for various η locations. Shown in Figure 8a are curves obtained at $\eta = 0.0$. Curves marked (1) are for data below Re_c , curves marked (2) are for data near Re_c and curves marked (3) are for data above Re_c . Curves (1) and (3) show a marked difference in high frequency, small scale mixing that takes place above and below Re_c ; at $f\delta/\Delta U = 10$ the two sets of spectral curves are separated by more than two orders of magnitude. The spectrum above the critical Reynolds number is qualitatively similar to most high Reynolds number turbulent velocity spectra. It is significant that the low frequency end of the spectrum is the same above and below the critical Reynolds number. Thus, the overall

mechanics and development of the large structure is essentially unaltered by the increase in fine scale mixing above Re_c .

The differences in the spectrum for two η locations at the same Reynolds number is shown in Figure 8b. This comparison is indicative of the difference in RMS fluctuations for the two locations.

5.2 Shear Layer ($r = 0.38$, $s = 1.0$)

5.2a Mean Profiles, Intermittency and Entrainment

As with the nitrogen-helium shear layer in order to get a feel for the extent of unmixedness of this constant density shear layer, the concentration probe was continuously sampled while being traversed across the layer. The results are shown in Figure 9a. Again, the extent of the fluctuations of the concentration of nitrogen is quite large, but, in this case, the fluctuations are rather symmetric about the middle of the layer. This symmetry can more easily be seen in the mean concentration profiles shown in Figure 9b. Shadowgraphs of this flow are shown in Plate 2. The remarkably flat profile of the turbulent zone mean concentration is noteworthy. Similar results were obtained by Fiedler¹⁶ for the temperature profiles in a slightly heated shear layer. The intermittency and mean velocity profiles are shown in Figures 9c and d, respectively. The entrainment rates calculated for this case are $Ve_1/U_1 = 0.056$ and $Ve_2/U_1 = 0.042$. Thus, only slightly more nitrogen was being entrained than argon-helium mixture. A few of the time histories used in these calculations are shown in Figure 10.

5.2b Unmixedness and RMS Fluctuations

Due to instrumentation problems only one set of data was taken for this case ($Re = 2 \times 10^4$). As will be shown in Section 6, this is above the corresponding critical Reynolds number. The unmixedness profiles for this constant density shear layer are shown in Figures 11a and b. Like the nitrogen helium shear layer, these values are relatively large and always less for the turbulent zone calculations than for the normal calculations. The similarities in the profiles for the two cases (a minimum in the middle with larger maxima on the edges) along with the fact that the observed large structures for both cases are quite similar may indicate that the mixing processes involved are quite similar. In other words, the mixing process may be much more a function of r (U_2/U_1) than s (ρ_2/ρ_1). The RMS profiles are shown in Figure 11c.

5.2c Probability Density Function

The P. D. F. 's for this case are shown in Figure 12. The slight difference in entrainment rates is evidenced by the slight skewness of the P. D. F. 's toward the nitrogen side. They are otherwise apparently symmetric both in η and C . Again, a Gaussian fit to these P. D. F. 's would be hard to justify.

5.3 Wake ($r = 1.0$, $s = 7.0$)

5.3a Mean Profiles and Spreading Rates

The continuous traverse profile for this inhomogeneous wake is shown in Figure 13a. Even though the 0 to 1 fluctuations are not as pronounced as in the previous two cases, the concentration fluctuations are still large. The profile also appears to be surprisingly symmetric.

The mean concentration and velocity profiles are shown in Figures 13b and c. U_s is the maximum velocity defect. The scatter in the velocity profile is mainly due to the normalization. The scatter represents less than 1% of the free-stream velocity, but about 10% of U_s . This is only a rough estimation of the actual velocity profile since this calculation neglects all fluctuation correlations. For this case, several of these correlations (especially $\overline{\rho'u'}$) probably can not be neglected. However, no estimation of their importance can be made from these data. A shadowgraph of a wake at this Reynolds number is shown in Plate 3e.

Again, several lengths can be defined from these curves. If the mean concentration curve is used to define the growth rate and the "edges" of the wake are defined as $\overline{C} = 0.1$ and $\overline{C} = 0.9$ then for $\theta = \theta_1 + \theta_2 = 0.11$ inches,

$$(\delta_c/\theta) = 0.67 \left((x - x_0)/\theta \right)^{0.5} \quad 5.3$$

If the mean velocity profile is used to define the growth rate of the wake and the "edges" are defined as the intersections of the maximum slope lines of the velocity profile with the line

$(U_1 - \overline{U})/U_s = 0$ then

$$(\delta_U/\theta) = 1.06 \left((x - x_0)/\theta \right)^{0.5} \quad 5.4$$

The 0.5 exponent was suggested by similarity arguments for a homogeneous wake and these data closely fit this growth law.

Typical time histories of the concentration for various η locations are shown in Figure 14.

5.3b RMS Fluctuations, Intermittency and Entrainment

The RMS fluctuation curves are shown in Figures 15a and b. In contrast to the results for the previous cases, these profiles are relatively flat. The remarkably flat $(\sqrt{C'^2})_T$ profile indicates that within the turbulence the level of fluctuation is rather constant across the wake. The absolute level of fluctuations is slightly less than that obtained for the other two cases. In contrast to the case for the shear layer, the intermittency (Fig. 15c-3) is rather skewed to the helium side. This is probably due to the difference in entrainment rates for the two fluids. These entrainment rates were calculated to be

$$Ve_1/U_1 = 0.22 \left(\frac{\theta}{x - x_0} \right)^{0.5} \quad 5.5$$

and

$$Ve_2/U_1 = 0.16 \left(\frac{\theta}{x - x_0} \right)^{0.5}$$

Thus, for small x , the wake entrains fluid at a faster rate than the shear layer.

Other than this skewness to the helium side, this intermittency function is quite similar to those obtained for the other two cases. This is rather remarkable considering the difference in the large structure for the wake and the shear layer.

5.3c Unmixedness

The unmixedness profiles for the wake are shown in Figure 16. Again, the profiles are remarkably flat and the values of unmixedness are lower than for the shear layer (the fluids are more mixed on a molecular level). Since the unmixedness

profiles for the wake are dissimilar to the profiles for the shear layer, the mixing process involved is probably different for the two cases. This of course is expected considering the difference in the large structures for the shear layer and the wake. One conclusion which can be drawn from these unmixedness profiles and the entrainment rates is that, for small x , more product will be produced in the wake than in the shear layer if the two fluids are reacting. This is because more molecular mixing and more entrainment are occurring in the wake than in the shear layer. Of course, for large x , the entrainment for the shear layer is much larger than for the wake and thus more product is being produced in the shear layer. What is meant by "large" and "small" x will be shown in Section 7.

5.3d Probability Density Function

Typical P.D.F.'s for the inhomogeneous wake are shown in Figure 17. The P.D.F.'s are quite symmetric both in η and C . Again, as with the previous P.D.F.'s, a Gaussian fit would be hard to justify. As mentioned earlier, these results will be made more quantitative in Section 7 by applying the data to a case in which the amount of product produced in a reacting flow can be predicted given the behavior of scalar contaminants in a similar nonreacting flow.

Discussed in the next section is a photographic study undertaken to gain more understanding of the Reynolds number effect observed in the inhomogeneous shear layer. The other two cases were also studied to see if any evidence for a similar effect in each case could be found.

VI. PHOTOGRAPHIC INVESTIGATION AND REYNOLDS NUMBER EFFECT

A close look at the shadowgraphs of the nitrogen-helium shear layer at various Reynolds numbers reveals why this observed Reynolds number effect was somewhat expected. Shown in Plate 1a, c, e and g are shadowgraphs of this flow at various Reynolds numbers. The critical Reynolds number observed in the measurements occurs at the streamwise position approximately one-third of the total length along Plates 1c and 1e. (Henceforth, streamwise positions will be labeled as the fraction of the total length of the plate in question, i. e., this position will be labeled $x = 1/3$.) It is quite easy to discern a marked change in the qualitative appearance of the flow at this point. The large structures upstream of this point and at Reynolds numbers below Re_C are still evidently quite sharply defined, while downstream of this point and at Reynolds numbers above Re_C the structures exhibit much more three-dimensional fine scale. The sharpness of this transition suggests that this observed Reynolds number effect is caused by an instability of some kind. Since the overall behavior and development of the large structures are not greatly affected by this instability (the linear growth rate continuous through this transition and the observation of large structures persists at Reynolds numbers much above Re_C^{17}), it was felt that the instability was associated with the large structure itself rather than with the entire flow field. In order to reinforce these ideas, a photographic study of both the plan and side views of the shear

layer was undertaken. The results of this study are presented in the next section and discussed with regard to the Reynolds number effect in Sections 6.2 and 6.3.

6.1 Photographic Investigation

The simultaneous plan and side views for this investigation were obtained by using a beam splitter in the incident parallel light beam. Only half of the plan view width is shown.

Possibly the best way to understand what is happening as the shear layer develops and thus to see what is causing the Reynolds number effect is to follow the development of the shear layer photographically as the Reynolds number is increased past Re_C . (A good Reynolds number survey of the shear layer is shown in Fig. 20 of Brown and Roshko.) Shown in Plate 1a and b is the shear layer at a relatively low Reynolds number. The completely two-dimensional nature of these large structures is shown by the upstream portion of both the plan and side views. This initial roll-up is essentially due to a two-dimensional Helmholtz instability. The nonlinear growth of this instability leads to a rotational two-dimensional vortex flow with the vortices pairing and amalgamating (see Winant and Browand and Roshko). The downstream portion of Plate 1a and b shows the flow in an amalgamation state. This amalgamation process apparently produces some three-dimensionality. This three-dimensionality produced by pairing can be seen in the first few structures shown in Plate 1c, d, e and f (and Brown and Roshko Fig. 20d and e). However, high speed movies of this process and pictures of

structures after amalgamation show that the three-dimensionality quickly dies off leaving again an essentially two-dimensional structure, as evidenced by the plan views. By this pairing process the layer grows linearly (in a mean sense), with the vortices correspondingly increasing in scale.

However, another type of three-dimensionality begins to appear just upstream of the critical Reynolds number position. This three-dimensionality corresponds in the photographs to the appearance of longitudinal (streamwise) lines and a "dimpling" of the surface of the large structures (apparent on the upstream and downstream edges of the structure in the plan-view photographs). This phenomenon first appears at a Reynolds number ($\delta \Delta U / \nu_{N_2}$) of approximately 10^4 . A close examination of the plan-views suggests that the three-dimensionality is cellular in nature and that these structures begin as hairpin vortices (Plate 1f, $x = 1/3$). Downstream of the appearance of these cellular structures as they are being rolled up into the large structures, they seem to become unstable and produce the three-dimensional small scales within the large structures. This catastrophic instability of the cellular structures always first takes place within the large structure itself. This phenomenon occurs at what is being called the critical Reynolds number. Several other features are noteworthy. Once these cellular structures appear, they continue to appear in all downstream structures and, in fact, seem to be continuous through several structures if the structures are

approximately equal in size. Thus, once the cellular structures become unstable as they are being rolled up into the large structures, the large structures become characterized by a considerable amount of fine scale mixing, and the thin vorticity layers (braids¹⁸) connecting the large structures become characterized by stream-wise cellular structures.

At even larger Reynolds numbers (Plate 1g and h), the cellular structure instability propagates into the braids, thus causing much of the layer to be characterized by small scale, three-dimensional motions. Even though there is an increase in the amount of three-dimensionality above Re_C , the shear layer continues to grow at the same linear rate and the basically two-dimensional large structures continue to pair and grow. The significance of this will be explored in Section 6.3.

Before proceeding to a possible explanation of this phenomenon, the results of a similar photographic investigation of other shear flows will be presented. This investigation was undertaken to see if evidence for a similar instability in the shear flows could be found.

First of all, in order to verify that the instability is not caused by the density difference in the nitrogen-helium shear layer, the constant density shear layer was investigated. Shown in Plate 2 is a Reynolds number survey of this flow. The shadowgraph technique is still usable due to the difference in indices of refraction between nitrogen and the mixture of argon and helium.

The similarities between this case and the last are striking. Again, at the lower Reynolds numbers, the large structures are completely two-dimensional (Plate 2a and b, up to $x = 1/5$ and Plate 2c and d, up to $x = 1/10$). At a Reynolds number of approximately 0.5×10^4 , the cellular structures again appear, beginning as hairpin vortices. At a Reynolds number of about 1.5×10^4 , the cellular structures become unstable within the large structures producing an increase in fine scale mixing. The repetition of this process is clearly shown in Plate 2e and f. Here the cellular structures are quite clearly seen in the braid connecting the last two structures, both of which show fine scale mixing produced by the instability of the cellular structures within the large structures. The continued basic two-dimensional nature of the large structures is illustrated in Plate 2g and h. The spanwise correlation can clearly be seen in the plan view. The instability of the cellular structures within the braids can also be seen throughout much of Plate 2h. (The apparent freestream turbulence is due to slight cooling of the gas at this high pressure.) Again, it can be seen that the growth and development of the large structures, and thus the shear layer itself, are basically unaltered by this cellular structure instability.

The next case studied was that of the inhomogeneous wake. This case is quite different from the previous cases for several reasons: the Reynolds number of a wake is constant, the flow has large structures of opposite vorticity, the similarity growth laws are different, and it is not clear whether or not a wake has

an amalgamation process. However, in spite of these differences, the inhomogeneous wake exhibited a similar instability. One difference, of course, between the instabilities observed is that for the wake, since the Reynolds number is constant, if the cellular structure is not present when the wake develops, it will not appear later. Likewise, if the cellular structure is present anywhere, it will be present everywhere. Plate 3a and b shows the wake at a relatively low Reynolds number. The completely two-dimensional nature of the large structures is evident. Plate 3c and d shows the wake at a larger Reynolds number. Again, the basically two-dimensional nature of the large structures is seen; however, the three-dimensional cellular structure is now present throughout the flow. The spanwise correlation is still evident in the slightly higher Reynolds number wake shown in Plate 3e and f, but now, the cellular structure has become somewhat unstable. In Plate 3g and h, the cellular structure has become quite unstable. The spanwise correlation, however, is still remarkable. Thus, an instability similar to the one observed in the shear layer is present in the inhomogeneous wake.

The final case studied was a homogeneous wake. Plate 4a and b shows the wake before the cellular structure develops and Plate 4c and d shows the wake after the cellular structure has become unstable. Again, a large spanwise correlation is seen in both cases even though one has much more three-dimensionality. For comparison, the momentum thickness was greatly increased for the final photographs of this case. The cellular structure is

clearly shown in the upstream portion of Plate 4e.

6.2 Explanation of Reynolds Number Effect

To review what has been observed to this point, the concentration measurements showed that above a critical Reynolds number the amount of small scale mixing in the shear layer is substantially increased. The entrainment rates into the turbulence are also larger above Re_C . The intermittency profiles showed that above this Reynolds number the probability of finding pure fluid within the layer is reduced. Just before this increase in small scales occurs, cellular three-dimensional structures appear in certain portions of the large structures beginning as hairpin vortices. These structures become unstable as they are being rolled up into the large structures. Thus, the large structure itself has its own instability and above a critical Reynolds number this instability generates strong local three-dimensionality and a cascade to high wave-numbers within the basically two-dimensional large structure. This cellular structure instability propagates into the braids connecting the large structures thus producing small scale three-dimensionality throughout much of the layer. This cellular structure, with its associated instability, repeats itself at all Reynolds numbers above Re_C .

Any discussion of the physical characteristics of this instability associated with the large structures and the reasons for its continued appearance at a Reynolds number above the critical value is somewhat speculative at this stage, though much can be inferred from the photographs and concentration data. It

is useful, however, to construct a model which is at least consistent with these inferences, if only to provide a possible basis for further experiments. In addition, since the development of the large structure is essentially an unsteady process with far from simple geometrical features, some physical appreciation of the mechanisms involved will almost certainly be required before any analytical description can be fruitfully tackled.

Since this new structure is cellular in nature and appears to be associated with a secondary flow, it is more than likely that this instability arises basically from a Rayleigh type instability. Rayleigh¹⁹ showed that in a steady, inviscid, purely circulatory flow, with tangential velocity $\bar{v}(r)$, the radial equilibrium is unstable if the square of the circulation decreases outward. Since $\frac{d}{dr}(r^2 \bar{v}^2) = 2r^3 \bar{\omega} \bar{\zeta}$, where $\bar{\zeta} = \frac{1}{r} \frac{d}{dr}(r \bar{v})$ is vorticity and $\bar{\omega} = \bar{v}/r$ is angular velocity, this inviscid criterion for circulatory flow can also be expressed in the form

$$\bar{\zeta} \bar{\omega} < 0 \quad . \quad 6.1$$

In other words, the motion is unstable whenever the sense of the local rotation $\bar{\zeta}$ is opposite to the sense of the general rotation $\bar{\omega}$. Taylor²⁰ carried the analysis a step further and determined the effect of viscosity on the stability boundary both experimentally and theoretically.

Coles²¹, using dimensional arguments and balancing of terms in the equations of motion, showed that the viscous Taylor criterion can be written

$$\bar{\zeta} \bar{\omega} < - \frac{\nu^2}{2L^4} \quad 6.2$$

where $\bar{\Omega}$ is some appropriate characteristic or mean value for the angular velocity $\bar{\omega}(r)$ and L is a characteristic scale for the secondary flow. By using Taylor's data, he showed that if $\bar{\Omega}$ is approximated by

$$\bar{\Omega} = (\omega_1 + \omega_2)/2 \quad 6.3$$

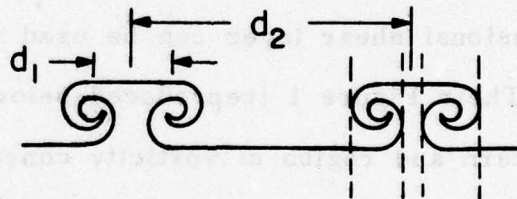
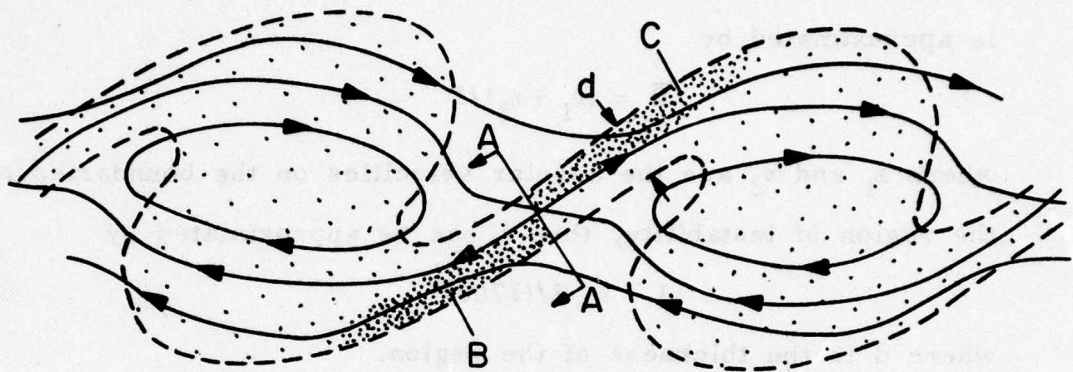
where ω_1 and ω_2 are the angular velocities on the boundaries of the region of instability, then L can be approximated by

$$L = d/(1708)^{\frac{1}{4}} \quad 6.4$$

where d is the thickness of the region.

In order to apply this criterion to the present case, some estimation of the terms involved must be made. The flow field calculations made by Corcos and Sherman of the inviscid roll-up of a two-dimensional shear layer can be used to make these estimations. Their Figure 1 (reproduced below) shows the streamline pattern and region of vorticity concentration (shaded area) for this roll-up process for a reference frame moving with the structures.

Since the regions marked B and C have vorticity of opposite sense to the general rotation within the regions, it is apparent that these regions meet the Rayleigh criterion (Eq. 6.1) for instability. Therefore, rough estimations of the terms in Eq. 6.2 will be made for these regions to determine the conditions required for these regions to also be unstable according to the Taylor criterion. All of the estimations to be made are quite rough and only made to see if a Taylor-type instability is consistent with the observed conditions within the large structures. What is

SENSE OF VORTICITY - 

SECTION A-A

suggested here is that the Taylor instability gives rise to hairpin vortices in which the "head" of the hairpin originates in the unstable region of a large structure and is connected to longitudinal vortex lines in the braid. Such a flow structure is shown schematically as Section A-A in the drawing. Two pairs of Taylor vortices are shown. Such a flow field would show up in the plan-view as several parallel lines (four are shown) running in the

streamwise direction in the braid. These lines would be produced by the interfaces between the two gases. If d is the thickness of the braid connecting the large structures, then the mean vorticity ($\bar{\zeta}$) can be approximated by $\Delta U/d$. Since the center of the braid is a stagnation point, ω_1 can be taken to be zero. Therefore, if the radius of curvature of the streamline on the edge of region B is taken to be $10d$, then ω_2 can be approximated as $-(\Delta U/2)/10d$. Thus, according to Eq. 6.3, $\Omega \approx -(\Delta U/2)/10d/2 = -\Delta U/40d$. Since the width of the region is $d/2$, L becomes $(d/2)/(1708)^{1/4}$. Upon inserting these approximations, Eq. 6.2 becomes

$$\left(\frac{\Delta U}{d}\right)\left(\frac{\Delta U}{40d}\right) > \frac{v^2}{2\left(\frac{d/2}{(1708)^{1/4}}\right)^4}$$

or

$$\frac{\Delta U d}{v} > 740 \quad . \quad 6.5$$

In Taylor's experiment it was found that the spacing between vortices (d_1) is approximately equal to the region thickness (d). From the photographs taken in this investigation, d_1 was found to be approximately one-tenth of the visual thickness of the layer (δ_{Vis}). Since δ_w is approximately one-half of δ_{Vis} , d/δ_w is approximately 0.2. Therefore, the Taylor criterion for instability becomes

$$\frac{\delta_w \Delta U}{v} > 0.4 \times 10^4 \quad . \quad 6.6$$

The closeness of this estimation of the point of onset of the Taylor instability to the observed point of onset is more coincidental than remarkable. Other equally valid estimations of the

terms involved would have obviously given different answers. However, what this does demonstrate is that the characteristics of the instability observed in this experiment are remarkably similar to the characteristics of the Taylor instability and that the conditions required for a Taylor instability are present in some regions of the large structures. It is also significant that the onset of the Taylor instability occurs at a lower Reynolds number in the homogeneous case than in the inhomogeneous case. The kinematic viscosity used for nondimensionalization in the inhomogeneous shear layer should actually be an average in some way of ν_{N_2} and ν_{He} rather than just ν_{N_2} . Thus, since any average of ν_{N_2} and ν_{He} will be larger than ν_{N_2} , a Reynolds number based on ν_{N_2} will be larger than a Reynolds number for the same conditions based on an average ν . Thus, the Reynolds number of the onset of the Taylor instability will appear to be higher if the Reynolds number is based on ν_{N_2} rather than an average ν . Plate 1f further demonstrates this kinematic viscosity dependence. The Taylor instability first appears on the nitrogen side of the large structure (region B) rather than on the helium side. This behavior is in accord with Eq. 6.6.

The large structure not only provides the conditions necessary for the development of this instability, but it also provides a mechanism to amplify it. Once the longitudinal vorticity produced by the Taylor instability is present in the braid, the vortex stretching due to the high strain rate in the plane of the braid (as shown in the drawing) strengthens this vorticity.

Apparently, as these Taylor vortex pairs, which have been strengthened by the stretching in the braid, are being rolled up into the large structure, the additional vortex stretching causes the pairs to precess around each other and eventually break up into small scale structures. As can be seen in the photographs, the generation of small scales is most apparent on the leading convex surface of the structure, on the high velocity side of the layer, and on the corresponding trailing surface on the low velocity side, which, from the above picture, is where the Taylor vortices are expected to break down. The precise mechanism by which these secondary flows break down to small scale motions is not entirely clear, but what is clear is that this motion is unstable in the sense that the vortex stretching in the braids and the Taylor instability in the large structures are coupled so that there is a strong mechanism which can transfer energy from the mean flow into three-dimensional motions.

Two final points concerning the spacing between pairs of Taylor vortices (d_2) should be noted. First of all, the downstream disturbance produced by the Taylor vortices in one braid is apparently sufficient to determine the positions of the vortices in the next braid. Since both braids are connected (in a sense) through one large structure, it is quite easy to see how this communication of position can take place. This upstream determination of the position of the vortices is seen in the photographs as the apparent continuation of the vortices through several large structures. The second point concerns the absolute value

of the spacing between the pairs of vortices. In the mean, d_2 was found to be approximately one-half δ_{vis} . However, the downstream influence just discussed is sufficiently strong so that d_2 changes in a stepwise manner. Thus, in some cases, d_2 is such that 40, 20, or 10 pairs can fit across the width of the layer (10 cm), and in other cases, 28, 14, or 7 pairs can fit. In other words, the spacing is constant until the point is reached at which approximately half the number of pairs across the layer is more stable. It is therefore apparent that the spacings between pairs of vortices is a function both of δ and the spanwise boundary conditions.

6.3 Implications of the Reynolds Number Effect

As a final comment on this three-dimensional instability, some of the important implications of this phenomenon will be pointed out.

As was discussed in the introduction to this work, the basically two-dimensional large structure observed in the shear layer was thought to not be able to undergo vortex stretching and therefore could not form a part of the fully-developed energy cascade from mean flow to smallest eddies, an essential characteristic of turbulence. Now, with the observed combination of production of Taylor vortices and vortex stretching, the process by which the large structure becomes a part (in fact, an indispensable part) of the cascade to small scales is clearly seen. This process is continuously repeated in the development of all large structures above the critical Reynolds number and is a

basic mechanism in the continued generation of three-dimensional turbulence energy. As evidenced by the pictures, there is little indication of a cascade to small scales below the critical Reynolds number. The high-wave-number energy in the power spectral density curves below Re_C comes from the sharp interfaces in the flow, not from small-scale spatial structures.

A further consequence of this phenomenon can be seen by what the three-dimensional instability does not do; it does not significantly affect the linear growth rate of the shear layer. This of itself is quite significant and demonstrates the fundamental role which the large structure plays. In the flow both above and below the critical Reynolds number, the Reynolds stress clearly derives from the large structure. However, above the critical Reynolds number, a further mechanism for the production of turbulence exists which is not at all related to the Reynolds stress. Thus, the Reynolds stress is not a complete measure of the production of turbulence energy.

As remarked earlier, the entrainment rates into the turbulence are increased by this instability phenomenon. Due to the breakdown of the Taylor vortices, the active, newly formed turbulence on the leading and trailing convex surfaces of the large structure evidently enhances the local entrainment rates at these surfaces. This reduces the penetration of irrotational fluid into the layer as can be seen from the intermittency plots. Thus, above the critical Reynolds number, the entrainment of the fluid into the turbulence is partially by "engulfment" due to the induced

velocity field of the large structure and the amalgamation process and partially by nibbling. The fact that the entrainment rate into the turbulence increased by only 8% above the critical Reynolds number suggests that nibbling is of lesser importance in the flow than engulfment.

The existence of these secondary instabilities helps to account for the large $\overline{v'w'}$ correlations which have been observed by some investigators³. A completely two-dimensional view of these large structures cannot account for these large correlations.

Finally, it is noted that all of these conclusions have been drawn from experiments on a mixing layer having a velocity ratio of $r = 1/\sqrt{7}$. There is no reason, however, to doubt that the results are applicable to mixing layers of any velocity ratio. The existence of large coherent structures in wakes at very high Reynolds numbers²² and the strong evidence of a similar instability in the homogeneous and inhomogeneous wakes shown in the photographs of these flows suggests that this instability may be an integral part of the production of turbulence energy in many other shear flows. *

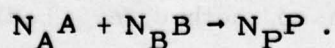
*Many of the ideas presented in this Section concerning the explanation of the observed Reynolds number effect were developed in discussions with Dr. Garry Brown and Professor Anatol Roshko. I am especially indebted to Dr. Brown for the many hours he spent thinking about this phenomenon and sharing his ideas with me.

VII. APPLICATIONS TO CHEMICALLY REACTING SHEAR FLOWS

7.1 Discussion of Toor's Analysis

The unmixedness results discussed in Section 5 are, for the most part, qualitative. Little more can be said in applying these results to chemically reacting shear flows than that one would expect more product produced for one flow than for the other. However, under certain restrictions, the concentration data obtained can be used to predict reaction rates for some special cases. An analysis of reactions under these conditions was first put forth by Toor²³. His analysis shows that if a few assumptions are made, the probability density functions of the concentrations of scalar contaminants in a nonreacting flow can be used to predict the amount of product formed in a reacting flow of similar geometry. This restriction of similarity between the reacting and nonreacting flows requires that the reaction be dynamically passive. This will be true if the reactants are dilute and the reaction releases only small amounts of heat.

The reacting and nonreacting flows for this analysis are illustrated in Figure 1. C_{i0} is the free-stream concentration of each reactant ($C_{i0} \ll 1$). In the nonreacting flow, the concentration of fluid 1 (C_H) is measured as a function of position and time. In the reacting flow, reactant A is assumed to be diluted in fluid 1 and reactant B in fluid 2; A and B are assumed to react irreversibly by the reaction



7.1

In order for this analysis to be valid, the diffusivities of all species in both flows must be equal ($D_A = D_B = D_P = D_1 = D_2$). Also, the reaction rate must be much faster than the diffusion rate. Many of these restrictions can be considerably relaxed before large errors are introduced.

The basic idea behind Toor's analysis as applied to the shear layer can be stated quite simply. Once the relative concentration of the two fluids in the nonreacting case are known for some position, then, given the free-stream concentrations of reactants for the reacting case, the relative concentrations of the reactants can be found for that position. However, since fast chemistry is assumed, the two reactants can not co-exist; they must react. Thus, for a given stoichiometry, the reactant that is in excess can be determined; the other reactant concentration will be equal to zero and the concentrations of the product and of the excess reactant can be calculated. Thus, the P. D. F.'s of the reactant and product concentrations can be found by calculating these concentrations for each scalar concentration and using the scalar P. D. F.'s to determine what percentage of time each occurs. The complete methodology of applying Toor's analysis to this investigation is given in Appendix D. It was found to be convenient to normalize all concentrations with the corresponding stoichiometric coefficients. Thus,

$$C_i = (\text{molar concentration of species } i) / N_i. \quad 7.2$$

7.2 "Equivalent Laminar Solution"

Another often used method for predicting the amount of product in a reacting shear flow is what can be called an

"equivalent laminar solution"²⁴. This method uses only mean profiles and neglects all concentration fluctuations. It is assumed that all fluid which is entrained into the layer is immediately mixed on a molecular level. Thus, for a given entrainment rate and a mean concentration profile, it is an upper bound on the amount of product which can be produced. By this analysis, \bar{C}_{AL} (the concentration of reactant A as calculated by the laminar solution) would be equal to $C_{Ao}\bar{C}_H$ and \bar{C}_{BL} would be equal to $C_{Bo}(1 - \bar{C}_H)$ except for the fact that the two reactants can not co-exist. Thus, one concentration must be reduced by the reaction and the other completely reacted away. Therefore,

$$\bar{C}_{AL} = C_{Ao}\bar{C}_H - C_{Bo}(1 - \bar{C}_H) \text{ if } \bar{C}_{AL} \geq 0, \quad 7.3$$

$$\bar{C}_{BL} = -C_{Ao}\bar{C}_H + C_{Bo}(1 - \bar{C}_H) \text{ if } \bar{C}_{BL} \geq 0, \quad 7.4$$

and
$$\begin{aligned} \bar{C}_{PL} &= C_{Ao}\bar{C}_H \text{ if } \bar{C}_{BL} > 0. \\ &= C_{Bo}(1 - \bar{C}_H) \text{ if } \bar{C}_{AL} > 0. \end{aligned} \quad 7.5$$

These equivalent laminar solutions will be used mainly to show the effect of the unmixedness of the gases on the amount of product formed.

7.3 Results and Discussion

Discussed in this section are the results of applying the analysis of Sections 7.1 and 7.2 to the three cases investigated.

Figure 18 shows the results of these calculations for the inhomogeneous shear layer at a Reynolds number above Re_C . The mean concentration profiles are shown in Figures 18a and c and the fluctuation profiles are shown in Figures 18b and d. Two different cases are shown here for comparison. In one case the ratio (α) of the entrained reactant A to the entrained reactant B is set equal to 1, and in the other case, this ratio is set equal to 3. The actual definition of α is

$$\alpha = \frac{C_{Ao} Ve_1}{C_{Bo} Ve_2} . \quad 7.6$$

Thus, the effect of changing freestream concentrations, entrainment rates, or stoichiometric coefficients (see Eq. 7.2) can be shown simply by changing α .

The effect of varying α can be seen by comparing Figure 18a with Figure 18c. For $\alpha = 1$, since $Ve_1 \doteq 3Ve_2$, C_{Bo} must be about three times as great as C_{Ao} . Thus, since C_{Bo} was unity for all calculations, \overline{C}_A/C_{Bo} approaches approximately 0.3 on the helium side and \overline{C}_B/C_{Bo} approaches 1.0. Obviously, since there is more reactant available for $\alpha = 3$ than for $\alpha = 1$, Figure 18c shows a higher concentration of product.

The equivalent laminar solution profiles are shown for the two cases by the dashed curves. The difference between the

laminar solution and the P.D.F. solution shows the effect of the unmixedness of the gases. For the laminar solution, A and B cannot exist at the same η location. Therefore, the profiles go to zero at the same location.

The RMS concentration fluctuations are shown in Figures 18c and d. $\sqrt{C_P'^2}$ is normalized with the value of C_P calculated for the laminar solution for the point at which both C_A and C_B go to zero.

The results for the inhomogeneous shear layer at a Reynolds number less than Re_C are shown in Figure 19. Again, two cases are shown: $\alpha = 1$ and $\alpha = 3$. The major differences to note between Figures 18 and 19 are that $\overline{C_P}$ is lower and the fluctuations are higher in Figure 19 than in Figure 18.

The homogeneous shear layer results are shown in Figure 20, and those for the wake are shown in Figure 21.

The effect that Reynolds number has on the extent of molecular mixing is shown in Figure 22. Plotted in Figure 22a is the integral of the product concentration normalized with the integral of the laminar product concentration as a function of Reynolds number for the inhomogeneous shear layer \tilde{P} and \tilde{P}_L are defined as

$$\tilde{P} = \int_{-\infty}^{\infty} \frac{\overline{C_P}}{\overline{C_{Bo}}} (y) dy$$

and

$$\tilde{P}_L = \int_{-\infty}^{\infty} \frac{\overline{C_{PL}}}{\overline{C_{Bo}}} (y) dy .$$

7.7

The rather sharp increase in the amount of product at the critical

Reynolds number again illustrates the increase in the extent of molecular mixing above Re_C . It is evident from this plot that the extent of molecular mixing is constant both above and below the critical Reynolds number, the mixing above Re_C being approximately 25% greater than that below Re_C . \tilde{P}/\tilde{P}_L for the homogeneous shear layer was found to be 0.75 and for the wake, 0.83. These values are for conditions above the critical Reynolds number estimated from the shadowgraphs for each case.

Since \tilde{P} has the dimensions of a length, it can be thought of as a measure of the "width" of the shear layer. Therefore, to show the effect that Reynolds number has on the growth rate based on this width, the Reynolds number based on \tilde{P} can be plotted as a function of the Reynolds number based on δ . This is shown in Figure 22b. The laminar solution is shown for comparison.

Some insight into a rather interesting problem can be gained by a further application of the results of this analysis. The problem is to determine how much excess of one reactant is required in order to completely react all of the other. For example, in this case, suppose reactant A is an oxidant and reactant B is a fuel. Then, the problem is to determine what freestream concentration of oxidant is required so that all of the entrained fuel will react. As a larger and larger percentage of fuel is being reacted, the variation of the flux of product past any streamwise station will approach the value of entrained fuel at that station. Therefore, the required excess of oxidant can be determined by finding the ratio of the streamwise variation of product flux to the entrained fuel as a function of the ratio of entrained oxidant to entrained fuel. Thus, if the flux of product

is defined as

$$\dot{\tilde{P}} = \int_{-\infty}^{\infty} \frac{C_P}{C_{Bo}} \frac{\bar{U}}{U_1} dy, \quad 7.8$$

what is required is a plot of $C_{Bo} \frac{d}{dx} (\dot{\tilde{P}}) / (Ve_2 C_{Bo} / U_1)$ as a function of $(Ve_1 C_{Ao} / Ve_2 C_{Bo})$. The results of this analysis are shown in Figure 23. Again, the Reynolds number effect is seen quite clearly in Figure 23a which shows the results for the inhomogeneous shear layer both above and below the critical Reynolds number. The results for the homogeneous shear layer and the wake are shown in Figures 23b and 23c, respectively. Figure 23d shows all four curves together for comparison.

The basic result of this analysis is that approximately ten times as much oxidant must be entrained as fuel in order to completely react the fuel. Thus, for the inhomogeneous shear layer and for unit stoichiometric coefficients, C_{Ao} would have to be a little over three times as great as C_{Bo} (since $Ve_1 / Ve_2 \doteq 3$). Likewise, for the wake, C_{Ao} must be approximately seven times as great as C_{Bo} (since $Ve_1 / Ve_2 \doteq 3/2$).

From the curves in Figure 23, the streamwise dependence of $\dot{\tilde{P}}$ can be determined. In other words,

$$(\dot{\tilde{P}})_{SL} = b_{SL}(x - x_0) \quad 7.9$$

for the shear layer and

$$\left(\frac{\dot{\tilde{P}}}{\theta} \right)_W = b_W \left(\frac{x - x_0}{\theta} \right)^{\frac{1}{2}} \quad 7.10$$

for the wake can be found. b_i is of course a function of α .

Thus, knowing this information, a comparison between the wake and the shear layer can be made. Such a comparison will determine which case produces more flux of product under similar conditions. Obviously, the answer depends on the x station at which the comparison is being made. As discussed in Section 5.3c, it is expected that the wake will initially have a larger product flux since it has better molecular mixing and, initially, more entrainment than the shear layer. This analysis will determine the x station at which the shear layer begins to have a larger product flux. In order for the comparison to be equitable, the reactant fluxes were arranged to be the same for both cases. This required that $(U_1 C_{A0})_{SL} = (U_1 C_{A0})_W$ and $(U_2 C_{B0})_{SL} = (U_2 C_{B0})_W$. Thus, for $(U_1)_{SL} = (U_1)_W$, the freestream concentrations would be $(C_{A0})_{SL} = (C_{A0})_W = 1.0$ and $(C_{B0})_{SL} = (C_{B0})_W / 0.38 = 1.0$. Therefore, since $(Ve_1/Ve_2)_{SL} = 3.4$ and $(Ve_1/Ve_2)_W = 1.4$, $\alpha_{SL} = 3.4$ and $\alpha_W = 3.7$. For these values of α

$$C_{B0} \frac{d}{dx} (\dot{P})_{SL} / (Ve_2 C_{B0} / U_1) = 0.88$$

and

$$C_{B0} \frac{d}{dx} (\dot{P})_W / (Ve_2 C_{B0} / U_1) = 0.77$$

Therefore,

$$C_{B0} (\dot{P})_{SL} = 0.018(x - x_0)$$

and

$$C_{B0} (\dot{P})_W = 0.091 \left(\frac{x - x_0}{\theta} \right)^{\frac{1}{2}}$$

Finally, the x station at which the product flux will be equal for both cases will be

$$(x - x_0) = 25\theta$$

or, for this case, $(x - x_0) = 2.8$ inches. This means that for these freestream concentrations of reactants, $C_{Bo}(\dot{\tilde{P}})_W$ will be larger than $C_{Bo}(\dot{\tilde{P}})_{SL}$ up to $(x - x_0) = 2.8$ inches.

For the range of α investigated ($0.1 < \alpha < 10$), the following empirical relationships between \tilde{P} and $\dot{\tilde{P}}$ were found:

for the inhomogeneous shear layer (Re_C^+),

$$(\tilde{P}/\dot{\tilde{P}}) = 1.73 + 0.13 \log \alpha, \quad 7.12$$

for the inhomogeneous shear layer (Re_C^-),

$$(\tilde{P}/\dot{\tilde{P}}) = 1.76 + 0.13 \log \alpha, \quad 7.13$$

for the homogeneous shear layer,

$$(\tilde{P}/\dot{\tilde{P}}) = 1.39 + 0.11 \log \alpha, \quad 7.14$$

and for the wake,

$$(\tilde{P}/\dot{\tilde{P}}) = 1.085 - 0.015 \log \alpha. \quad 7.15$$

Therefore, by combining the information in Figure 23 with that in Equations 7.12 and 7.15, this same comparison between the shear layer and the wake can be made on the basis of \tilde{P} instead of $\dot{\tilde{P}}$. When this was done it was found that $C_{Bo}\tilde{P}$ is larger for the wake than for the shear layer up to $(x - x_0) = 9\theta$ (1 inch).

One final comparison was made in which all freestream concentrations were set equal ($(C_{Ao})_{SL} = (C_{Ao})_W = (C_{Bo})_{SL} = (C_{Bo})_W$). It was found from this analysis that $C_{Bo}\dot{\tilde{P}}$ is larger for the wake than for the shear layer up to $(x - x_0) = 10.9$ inches and $C_{Bo}\tilde{P}$ is larger up to $(x - x_0) = 3.9$ inches. This increase in the trade off x station is of course due to the increase in freestream concentration flux.

Curves similar to those in Figure 23 were suggested by Garry Brown.

VIII. CONCLUDING REMARKS

This investigation was able to meet, to some extent, the goals that were stated in the Introduction to this work. The extent of molecular mixing was measured for several turbulent shear flows. It was determined that much of the engulfed fluid is still in a high state of unmixedness. Even the fluid which has been entrained into the turbulent regions is far from being perfectly mixed on the molecular level. It was further found that above a certain critical Reynolds number, the extent of molecular mixing increased. Accordingly, the fluctuations in the concentration decreased. These results were made more quantitative by using the data to predict the results when a diffusion-limited chemical reaction is incorporated into the flow. The results of this analysis showed the effect that the lack of molecular mixing has on the progress of a chemical reaction.

Further understanding of the growth and development of the large structures in turbulent shear flows came from a rather unexpected source. A three-dimensional instability associated with the large structure itself was discovered while attempting to find the cause of the effect varying the Reynolds number has on the extent of molecular mixing. It may now be seen that the large coherent structures are not only an integral part of the mechanism which controls the growth of the shear layer but also play a central role in the production of small scale, three-dimensional turbulence.

APPENDIX A

Concentration Probe

The probe being used to measure concentration histories in turbulent mixing regions is a development of the Brown-Rebollo probe in which the resolution has been improved by reduction in size. This is accomplished by stretching a hot-wire (5×10^{-5} inches in diameter) across the diameter of a small (0.2 mm) capillary tube (see Fig. 2a). The capillary tube is necked down upstream of the wire to a very small throat (0.01 mm) so that when a vacuum is applied to the downstream end of the capillary the flow in the throat is sonically choked. The flow past the wire is then independent of the freestream velocity (to order M_∞^2) and is dependent only on the throat conditions (γ^* , a^* , ρU^*). The conditions at the wire are thus functions only of the properties of the gas being sampled.

The probe is calibrated by placing it in a chamber in which the pressure (P_0) and the relative concentrations (C) of the two gases to be used in the experiment can be controlled. Thus, the voltage output $V_{\text{Probe}} = V(P_0, C)$ is determined. These data are then curve fitted to give $C = C(V_P, P_0)$.

Estimates of the spatial resolution of the probe can be made by calculating the captured streamtube diameter, which is a function of the sonic throat diameter and the freestream Mach number. For example, for a freestream velocity of 1000 cm/sec and a throat diameter of 0.01 mm, the streamtube diameter (and the lateral resolution) is approximately 0.1 mm. The streamwise

spatial resolution is a function of the hot-wire frequency response and the freestream velocity. Again, for a freestream velocity of 1000 cm/sec and a wire response of 100 kHz, the streamwise spatial resolution is 0.1 mm. The wire response is estimated from a standard square wave test for a constant temperature hot-wire. A sample square wave test response is shown in Fig. 2b. An interpretation of this response signal can be found in Ref. 25.

An operational calibration of the probe response was obtained by making use of the concentration signal ($C(t)$) itself. Interfaces in the mixing region provide very high values of dC/dt at the probe. Analysis of the frequency spectra of the signals obtained under various conditions (δ , U and x can be varied) shows whether any differences can be attributed to resolution limitations of the probe. In this way it was concluded that the probe has a frequency response of at least 45 kHz, which corresponds to a spatial resolution of 0.2 mm at $U_1 = 1000$ cm/sec.*

*Much of the work done to improve the concentration probe was done by Dr. Garry Brown.

APPENDIX B

Minimization of the Effect of Hydrostatic Forces

In the inhomogeneous shear flows studied, the difference in the densities of the two fluids produces hydrostatic forces which induce streamwise gradients in both pressure and velocity. The magnitude of this effect can be seen by a simple application of the steady Bernoulli equation, where ()_A is air,

$$P_o = p_s + \frac{1}{2}\rho U^2 + (\rho_A - \rho)gx . \quad B.1$$

The last term is included since the flow is vertical and, therefore, the relative hydrostatic forces must be taken into account when measuring pressures. Thus, the coefficient of pressure for the difference in pressure between two vertical points (subscripts a and b) is

$$C_P = \frac{p_{s_b} - p_{s_a}}{\frac{1}{2}\rho U_a^2} = 1 - \left(\frac{U_b}{U_a}\right)^2 - 2 \left(\frac{\rho_A - \rho}{\rho}\right) \frac{g\Delta h}{U_a^2} . \quad B.2$$

If the fluid is helium, then

$$C_{P_H} = 1 - H^2 - S_H \quad B.3$$

and if the fluid is nitrogen, then

$$C_{P_N} = 1 - N^2 - S_N , \quad B.4$$

where H is the ratio of the velocities at the two points (U_b/U_a) for helium, N is (U_b/U_a) for nitrogen and

$$S_i = \frac{\left(\frac{\rho_A - \rho_i}{\rho_i}\right) g\Delta h}{U_a^2} . \quad B.5$$

Since this experiment consists basically of two adjacent columns

of gas flowing in contact with each other, the static pressure will adjust itself (through changing velocities) so that the pressure will be approximately uniform at any streamwise station. Therefore, C_{PH} will be equal to C_{PN} since $\rho_N U_N^2 = \rho_H U_H^2$ for the inhomogeneous shear layer. Thus, Eqs. B.3 and B.4 can be combined to give

$$1 - H^2 - S_H = 1 - N^2 - S_N$$

or

$$N^2 - H^2 = S_H - S_N = S \quad B.6$$

Equations B.3, B.4 and B.6 show to what degree the hydrostatic forces will cause gradients in the pressure and velocity. For example, if C_{PH} and C_{PN} were adjusted to be zero (by positioning the side walls) and if the pressures measured were for ports at streamwise stations 10 cm apart, then the velocities could change by a total of more than 5% for low speed flows.

Since constant freestream velocities are desired, the static pressure should be adjusted so that N and H are as close to unity as possible. In other words, the pressure gradient should be adjusted to minimize the sum

$$(1 - H)^2 + (1 - N)^2 \quad B.7$$

Upon eliminating H in Eq. B.7 by using Eq. B.6 and using the standard minimization technique, the following fourth order equation for N is found:

$$N^4 - N^3 + N^2 S - NS + S/4 = 0 \quad B.8$$

The proper root of Eq. B.8 can then be substituted into Eq. B.4 to determine what pressure gradient will minimize the effect that the hydrostatic forces have on the velocities. By using this

technique, the decrease in freestream velocity on the helium side could be kept to less than 2% for $U_a = 1000$ cm/sec and less than 0.5% for $U_a = 2000$ cm/sec. The corresponding nitrogen freestream velocities increased by less than 2% and 0.5%. A similar procedure was used for the inhomogeneous wake.

APPENDIX C

Technique Used to Measure the Density of a Mixture of Gases

In order to study the mixing process in a constant density shear layer, two gases of equal density but different concentration probe response were needed. Two such gases are nitrogen and a homogeneous mixture of 1/3 helium and 2/3 argon. Since the mixing of the helium and argon could not easily be controlled, some means of measuring the density of the mixture was needed in order to determine if the mixture did indeed have the same density as nitrogen.

Such a measurement can simply be made by comparing the hydrostatic pressure of the mixture to that of a known gas. Since, for a stationary, vertical column of fluid of height h , the pressure at the top of the column (p_1) is related to the pressure at the bottom (p_2) by the equation

$$p_2 = p_1 + \rho gh, \quad \text{C.1}$$

this comparison of hydrostatic pressures can be made by measuring the pressure difference at the tops of two columns of fluid, one being the mixture and the other a known gas, and allowing the pressures at the bottoms to be equal. Thus, for the mixture column,

$$p_{2m} = p_{1m} + \rho_m gh$$

and for the known gas column

$$p_{2g} = p_{1g} + \rho_g gh.$$

Since p_{2m} and p_{2g} are arranged to be equal,

$$p_{1m} - p_{1g} = \Delta p_m = (\rho_g - \rho_m)gh . \quad C.2$$

The test column can be calibrated in the sense of determining gh by comparing two known gases in the above manner. Thus,

$$\Delta p_c = (\rho_g - \rho_c)gh \quad C.3$$

where the subscript c is used to denote calibration conditions.

Combining Eqs. C.2 and C.3 gives

$$\frac{\Delta p_m}{\Delta p_c} = \frac{(\rho_g - \rho_m)}{(\rho_g - \rho_c)}$$

which, upon solving for ρ_m becomes

$$\rho_m = \rho_g - \frac{\Delta p_m}{\Delta p_c} (\rho_g - \rho_c)$$

or

$$\frac{\rho_m}{\rho_{N_2}} = \frac{\rho_g}{\rho_{N_2}} - \frac{\Delta p_m}{\Delta p_c} \frac{(\rho_g - \rho_c)}{\rho_{N_2}} . \quad C.4$$

In the actual measurements, the gas that the mixture was compared with was air and the calibration gas was helium. The pressures at the bottoms of the columns were arranged to be equal simply by opening the bottoms to the atmosphere. This was a stable configuration since the mixture was lighter than air. A column was needed for the air to eliminate room currents. In order to insure at least 0.1% accuracy in the measure of density, the temperatures of the gases and the humidity of the air had to be monitored during both the calibration and test procedures. Taking this into account, Eq. C.4 becomes

$$\left(\frac{\rho_m}{\rho_{N_2}} \right)_T = \left(\frac{\rho_{air}}{\rho_{N_2}} \right)_T - \frac{\Delta p_m}{\Delta p_c} \frac{(\rho_{air} - \rho_m)_c}{(\rho_{N_2})_T} \quad C.5$$

where subscript T signifies test conditions.

This procedure was suggested by Dr. John LaRue of the University of California, San Diego.

APPENDIX D

Analysis for Predicting Chemical Reaction Rates from Scalar
Probability Density Functions

The idea of using the probability density functions of scalar contaminates in nonreacting flows to predict reaction rates for similar reacting flows was first proposed by Toor²³. The technique of applying these ideas to the present work are presented below. Some of the ideas put forth in Reference 24 are also incorporated.

For a nonreacting shear layer, it is assumed that the concentration histories of one of the gases (C_H) is known as a function of both position and time. Therefore, the P.D.F.'s of the concentration ($P_H[C_H]$) can be computed. For a similar shear layer in which reactant A is diluted in gas 1 and reactant B is diluted in gas 2 (see Fig. 1) and they react irreversibly according to



the concentrations of A, B, and P (C_A , C_B and C_P) are to be calculated as a function of time and position. Thus, for example, $\overline{C_P}$ and $\overline{C_P'^2}$ can be calculated as a function of η where $C_P = \overline{C_P} + C_P'$.

For this analysis, it is convenient to incorporate the stoichiometry of the reaction into the concentrations. Thus,

$$C_i = (\text{molar concentration of species } i)/N_i.$$

This will eliminate the necessity of carrying the N_i 's along in the analysis but the results will still be valid for all values of N_i .

Next, let

$$Z_1 = \frac{C_A + C_P}{C_{A0}} \quad \text{D. 2}$$

and

$$Z_2 = \frac{C_B + C_P}{C_{B0}} \quad \text{D. 3}$$

If the diffusivities of all species are equal ($D_A = D_B = D_P = D_1 = D_2$) and if the reaction rate is much faster than the diffusion rate, then

$$Z_1 = C_H \quad \text{D. 4}$$

and

$$Z_2 = 1 - C_H \quad \text{D. 5}$$

This is true since $C_A/C_{A0} = C_H$ except when C_A is reduced due to reacting. But C_A will be reduced by exactly C_P . Therefore the sum of C_A and C_P will be C_H . A similar analysis applies to Z_2 except that $C_B/C_{B0} = 1 - C_H$. Combining D. 2 and D. 3 with D. 4 and D. 5 gives

$$Y = \frac{C_A - C_B + C_{B0}}{C_{A0} + C_{B0}} = C_H \quad \text{D. 6}$$

Now, since $Y = Z_1 = C_H$, then their P.D.F.'s will be equal:

$$P_Y[Y] = P_{Z_1}[Z_1] = P_H[C_H] \quad \text{D. 7}$$

With the assumed very fast chemistry, A and B cannot exist at the same place at the same time, or

$$\overline{C_A C_B} = 0 \quad . \quad D. 8$$

Therefore, if

$$X = C_A - C_B \quad , \quad D. 9$$

then obviously,

$$\begin{aligned} C_A &= X \text{ if } X > 0 \\ &= 0 \text{ if } X < 0 \end{aligned} \quad D. 10$$

$$\begin{aligned} C_B &= -X \text{ if } X < 0 \\ &= 0 \text{ if } X > 0 . \end{aligned} \quad D. 11$$

Thus,

$$P_A[C_A] = P_X[C_A] \text{ for } C_A > 0 \quad D. 12$$

and

$$P_B[C_B] = P_X[-C_B] \text{ for } C_B > 0 . \quad D. 13$$

From the identity

$$P_X[X] dX \equiv P_Y[Y(X)] dX \frac{\partial Y}{\partial X} .$$

it can be shown that

$$P_X[X] = \frac{P_Y\left[\frac{X + C_{Bo}}{C_{Ao} + C_{Bo}}\right]}{C_{Ao} + C_{Bo}} \quad D. 14$$

using $\partial Y / \partial X = 1 / (C_{Ao} + C_{Bo})$, D. 6 and D. 9.

Therefore,

$$P_A[C_A] = P_H\left[\frac{C_A + C_{Bo}}{C_{Ao} + C_{Bo}}\right] / (C_{Ao} + C_{Bo}) \quad D. 15$$

and

$$P_B[C_B] = P_H \left[\frac{-C_B + C_{Bo}}{C_{Ao} + C_{Bo}} \right] / (C_{Ao} + C_{Bo}) . \quad D.16$$

Since P_H is known, P_A and P_B can be found. Thus, using the identities

$$\bar{C}_i \equiv \int_{C_i} C_i P_i[C_i] dC_i , \quad D.17$$

$$\bar{C}_i^2 \equiv \int_{C_i} C_i^2 P_i[C_i] dC_i , \quad D.18$$

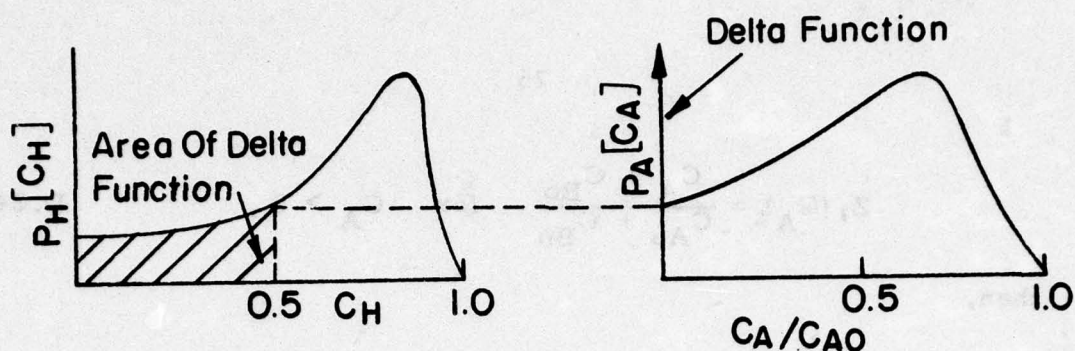
and

$$\bar{C}_i'^2 \equiv \bar{C}_i^2 - (\bar{C}_i)^2 , \quad D.19$$

\bar{C}_A , \bar{C}_B , $\sqrt{\bar{C}_A'^2}$ and $\sqrt{\bar{C}_B'^2}$ can be calculated.

Equation D.15 gives the P.D.F. for C_A for all time that $C_A > 0$. There is a delta function at $C_A = 0$ which accounts for all the time that B is in excess making $C_A = 0$. Although the area of this delta function can easily be calculated, it is not necessary to do so since the P.D.F.'s are only used as integrands when multiplied by their arguments (see D.17 and D.18). Thus, $C_A P[C_A] = 0$ for $C_A = 0$. As an example of the use of D.15, consider the following given shape for $P_H[C_A]$ and let $C_{Ao} = C_{Bo} = 0.5$. Then

$$\begin{aligned} P_A[C_A] &= \frac{1}{C_{Ao} + C_{Bo}} P_H \left[\frac{C_A + C_{Bo}}{C_{Ao} + C_{Bo}} \right] \text{ for } 0 < C_A \leq C_{Ao} \\ &= P_H[C_A + 0.5] \quad \text{for } 0 < C_A \leq 0.5 . \end{aligned}$$



In order to find $\overline{C_P}$, D.2 and D4 must be used. Thus

$$\frac{C_A + C_P}{C_{A0}} = C_H, \quad \text{D.20}$$

or

$$\overline{C_P} = C_{A0} \overline{C_H} - \overline{C_A}. \quad \text{D.21}$$

From D.19,

$$\overline{C_P'^2} = \overline{C_P^2} - (\overline{C_P})^2$$

Thus, in order to find $\overline{C_P'^2}$, $\overline{C_P^2}$ must be calculated. From D.20 and D.4,

$$\overline{C_P^2} = C_{A0}^2 \overline{Z_1'^2} - 2 C_{A0} \overline{Z_1 C_A} + \overline{C_A^2}. \quad \text{D.22}$$

Since $\overline{Z_1'^2} = \overline{C_H^2}$ and $\overline{C_A^2}$ are known, $\overline{Z_1 C_A}$ must be determined.

From P.D.F. analysis,

$$\overline{Z_1 C_A} = \int_{C_A} Z_1 (C_A) C_A P_A [C_A] dC_A. \quad \text{D.23}$$

Since

$$Z_1 = Y = \frac{X + C_{B0}}{C_{A0} + C_{B0}},$$

$$Z_1(C_A) = \frac{C_A + C_{Bo}}{C_{Ao} + C_{Bo}} \quad \text{for } C_A > 0, \quad \text{D.24}$$

then,

$$\overline{Z_1 C_A} = \int_{C_A} \left(\frac{C_A + C_{Bo}}{C_{Ao} + C_{Bo}} \right) \left(\frac{C_A}{C_{Ao} + C_{Bo}} \right) P_H \left[\frac{C_A + C_{Bo}}{C_{Ao} + C_{Bo}} \right] dC_A, \quad \text{D.25}$$

or,

$$\overline{Z_1 C_A} = \frac{\overline{C_A^2}}{C_{Ao} + C_{Bo}} + \frac{C_{Bo} \overline{C_A}}{C_{Ao} + C_{Bo}}. \quad \text{D.26}$$

Therefore,

$$\begin{aligned} \overline{C_P^{12}} &= C_{Ao}^2 \overline{C_H^2} + \left(\frac{C_{Bo} - C_{Ao}}{C_{Ao} + C_{Bo}} \right) \overline{C_A^2} \\ &\quad - 2 \frac{C_{Ao} C_{Bo} \overline{C_A}}{C_{Ao} + C_{Bo}} - (\overline{C_P})^2 \end{aligned} \quad \text{D.27}$$

It is interesting to note that the integral definition of unmixedness takes on physical significance when viewed in light of this analysis. This integral definition is, restated,

$$UM = \frac{t_1 \int_{t_1} (C - \overline{C}) dt_1 + t_2 \int_{t_2} (\overline{C} - C) dt_2}{\int_{t_1} (1 - \overline{C}) dt_1 + \int_{t_2} \overline{C} dt_2} \quad \text{D.28}$$

where t_1 is the time for $C > \overline{C}$ and t_2 is the time for $C < \overline{C}$.

From the definition of probability densities, it can be seen that

$$P_H[C] dC = dt/T$$

where T is the total time of the sample. This simply states that

$P_H[C] dC$ is the fraction of time that C is within the limits of dC .

Therefore, D.28 can be rewritten as

$$UM = \frac{\int_0^1 (C - \bar{C}) P_H[C] dC + \int_0^{\bar{C}} (\bar{C} - C) P_H[C] dC}{(1 - \bar{C}) \int_{\bar{C}}^1 P_H[C] dC + \bar{C} \int_0^{\bar{C}} P_H[C] dC} \quad D.29$$

These integrals can be evaluated by the following analysis. If the freestream concentrations are arranged for each \bar{C} such that

$$\frac{C_{Bo}}{C_{Ao} + C_{Bo}} = \bar{C}, \quad D.30$$

then, whenever $C = \bar{C}$, no reactants will be present, only product. The reactants will have exactly "burned" each other up. If $C > \bar{C}$, then A will be in excess and $C - \bar{C} = C_A / (C_{Ao} + C_{Bo})$. If $C < \bar{C}$, then B will be in excess and $C - \bar{C} = C_B / (C_{Ao} + C_{Bo})$. Using these two relationships, along with D.30, D.29 becomes

$$UM = \frac{\int_0^{C_{Ao}} \frac{C_A}{C_{Ao} + C_{Bo}} P_H \left[\frac{C_A + C_{Bo}}{C_{Ao} + C_{Bo}} \right] dC_A}{C_{Ao} \int_{\bar{C}}^1 P_H[C] dC + C_{Bo} \int_0^{\bar{C}} P_H[C] dC} + \frac{\int_0^{C_{Bo}} \frac{C_B}{C_{Ao} + C_{Bo}} P_H \left[\frac{-C_B + C_{Bo}}{C_{Ao} + C_{Bo}} \right] dC_B}{C_{Ao} \int_{\bar{C}}^1 P_H[C] dC + C_{Bo} \int_0^{\bar{C}} P_H[C] dC}$$

From Eqs. D.15 and D.16, it can be seen that the numerator is

simply the sum of the concentrations of the unburned reactants $(\bar{C}_A + \bar{C}_B)$ and the denominator is simply the freestream concentrations multiplied by the percentages of time that each would have occurred if the gases were perfectly unmixed. Therefore, UM finally can be interpreted as

$$UM = \frac{\bar{C}_A + \bar{C}_B}{(\bar{C}_A)_{UM} + (\bar{C}_B)_{UM}} \quad D. 31$$

where $(\bar{C}_i)_{UM}$ is the mean concentration that would have been measured if the gases were perfectly unmixed. Thus, if the gases are perfectly mixed ($C(t) = \bar{C}$ for all time), then $\bar{C}_A = \bar{C}_B = 0$ and $UM = 0$. Further, if the gases are perfectly unmixed ($C(t) = 1$ or 0), then $\bar{C}_A = (\bar{C}_A)_{UM}$ and $\bar{C}_B = (\bar{C}_B)_{UM}$ and $UM = 1$.

REFERENCES

1. Liepmann, H. W. and Laufer, J., "Investigation of Free Turbulent Mixing", Tech. Note No. 1257, N. A. C. A., 1947.
2. Wygnanski, I. and Fiedler, H. E., "The Two-dimensional Mixing Region", Journal of Fluid Mechanics, Vol. 41, 1970, pp. 327-361.
3. Brown, G. L. and Roshko, A., "On Density Effects and Large Structure in Turbulent Mixing Layers", Journal of Fluid Mechanics, Vol. 64, 1974, pp. 775-816.
4. Rebollo, M., "Analytical and Experimental Investigation of a Turbulent Mixing Layer of Different Gases in a Pressure Gradient", Ph. D. Thesis, California Institute of Technology, 1973.
5. Mollo-Christensen, E., "Intermittency in Large-Scale Turbulent Flows", Annual Review of Fluid Mechanics, Vol. 5, Annual Reviews, Palo Alto, 1973, pp. 101-118.
6. Winant, C. D. and Browand, F. K., "Vortex Pairing: the Mechanism of Turbulent Mixing-Layer Growth at Moderate Reynolds Number", Journal of Fluid Mechanics, Vol. 63, 1974, pp. 237-255.
7. Laufer, John, "New Trends in Experimental Turbulence Research", Annual Review of Fluid Mechanics, Vol. 7, Annual Reviews, Palo Alto, 1975, pp. 307-326.
8. Davies, P. O. A. L. and Yule, A. J., "Coherent Structures in Turbulence", Journal of Fluid Mechanics, Vol. 69, 1975, pp. 513-537.
9. Murthy, S. N. B. (ed.), Turbulent Mixing in Nonreactive and Reactive Flows, Plenum Press, New York, 1975.

10. Roshko, A., "Structure of Turbulent Shear Flows: A New Look", A.I.A.A. Paper No. 76-78.
11. Brown, G.L. and Rebollo, M.R., "A Small, Fast-Response Probe to Measure Composition of a Binary Gas Mixture", AIAA Journal, Vol. 10, No. 5, May 1972, pp. 649-652.
12. Cochran, William T. et al., "What is the Fast Fourier Transform?", IEEE Transactions on Audio and Electroacoustics, Vol. AU-15, No. 2, June 1967, pp. 45-55.
13. Bergland, G.D., "A guided tour of the fast Fourier transform", IEEE Spectrum, July 1969, pp. 41-52.
14. Murthy, S.N.B., "Turbulent Mixing in Nonreactive and Reactive Flows: A Review", Turbulent Mixing in Nonreactive and Reactive Flows, Plenum Press, New York, 1975, pp. 1-84.
15. Brown, G.L., "The Entrainment and Large Structure in Turbulent Mixing Layers", Fifth Australasian Conference on Hydraulics and Fluid Mechanics, Christchurch, New Zealand, December, 1974.
16. Fiedler, Heinrich F., "Transport of Heat Across a Plane Turbulent Mixing Layer", Advances in Geophysics (1974) 18A, pp. 93-109.
17. Dimotakis, P.E. and Brown, G.L., "Large Structure Dynamics and Entrainment in the Mixing Layer at High Reynolds Numbers", Tech. Report CIT-7-PU, Project SQUID, 1975.
18. Corcos, G.M. and Sherman, F.S., "Vorticity concentration and the dynamics of unstable free shear layers", Journal of Fluid Mechanics, Vol. 73, 1976, pp. 241-264.

19. Lord Rayleigh, "On the Dynamics of Revolving Fluids", Proceedings of the Royal Society, London, Series A, Vol. 93, 1916, pp. 148-154.
20. Taylor, G.I., "Stability of a Viscous Liquid Contained Between Two Rotating Cylinders", Philosophical Transactions, Series A, Vol. 223, 1923, pp. 289-343.
21. Coles, D., "A Note on Taylor Instability in Circular Couette Flow", Journal of Applied Mechanics, September 1967, pp. 529-534.
22. Roshko, A., "Experiments on the flow past a circular cylinder at very high Reynolds number", Journal of Fluid Mechanics, Vol. 10, 1961, pp. 345-356.
23. Toor, H.L., "Mass Transfer in Dilute Turbulent and Non-turbulent Systems with Rapid Irreversible Reactions and Equal Diffusivities", A.I.Ch.E. Journal, Vol. 8, No. 1, March, 1962, pp. 70-78.
24. Alber, Irwin E. and Batt, Richard G., "Diffusion-Limited Chemical Reactions in a Turbulent Shear Layer", AIAA Journal, Vol. 14, No. 1, pp. 70-76.
25. Cantwell, Brian J., "Matilda Meter Constant Temperature Anemometers", Graduate Aeronautical Laboratories Manual, California Institute of Technology, 1975.

- d_1 = STREAMWISE SPATIAL
RESOLUTION = 0.1mm
 d_2 = CAPTURED STREAMTUBE
DIAMETER = 0.1mm
 d_3 = CAPILLARY OPENING = 0.1mm
 d_4 = CAPILLARY DIAMETER
= 0.2mm

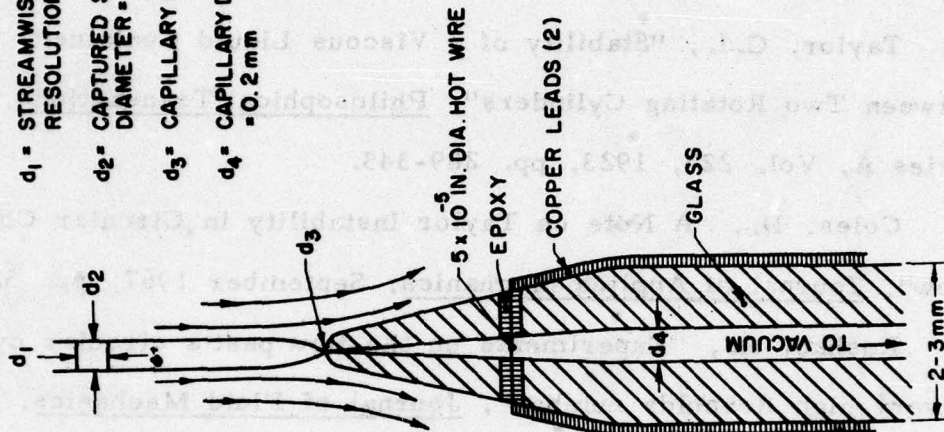


FIG. 2a CONCENTRATION PROBE

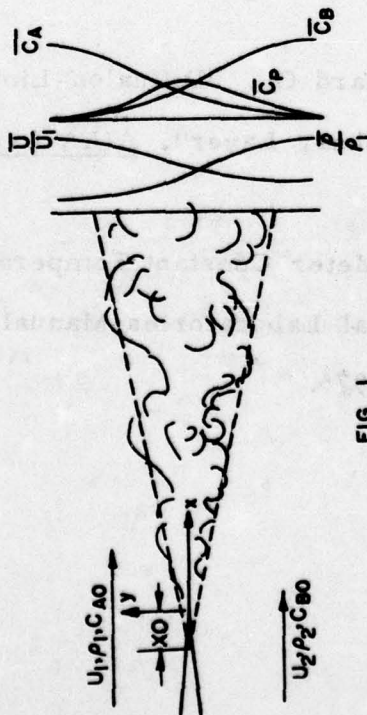


FIG. 1



FIG. 2b HOTWIRE TIME RESPONSE

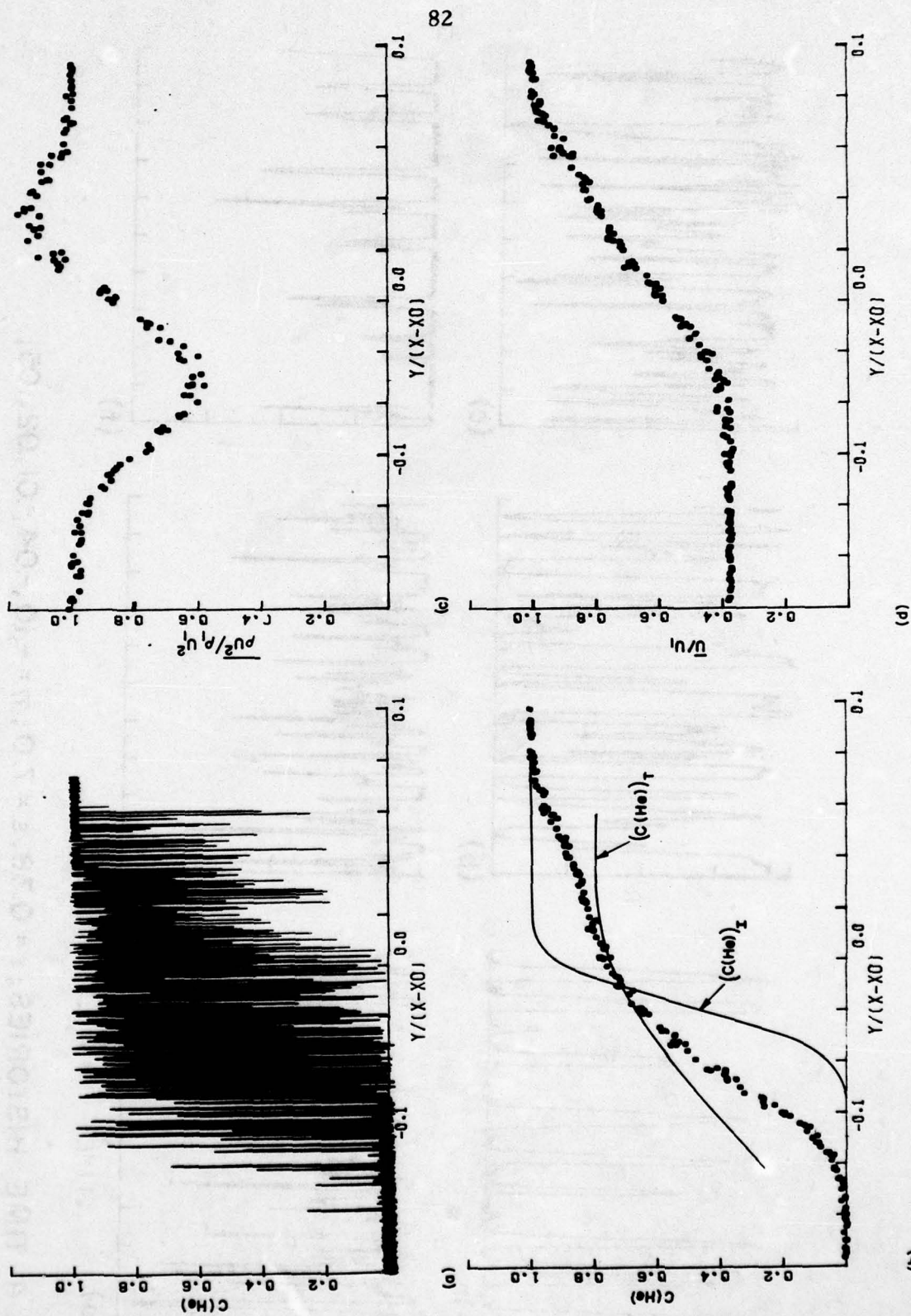


FIG. 3 TRAVERSE PROFILES; $r = 0.38$, $s = 7.0$

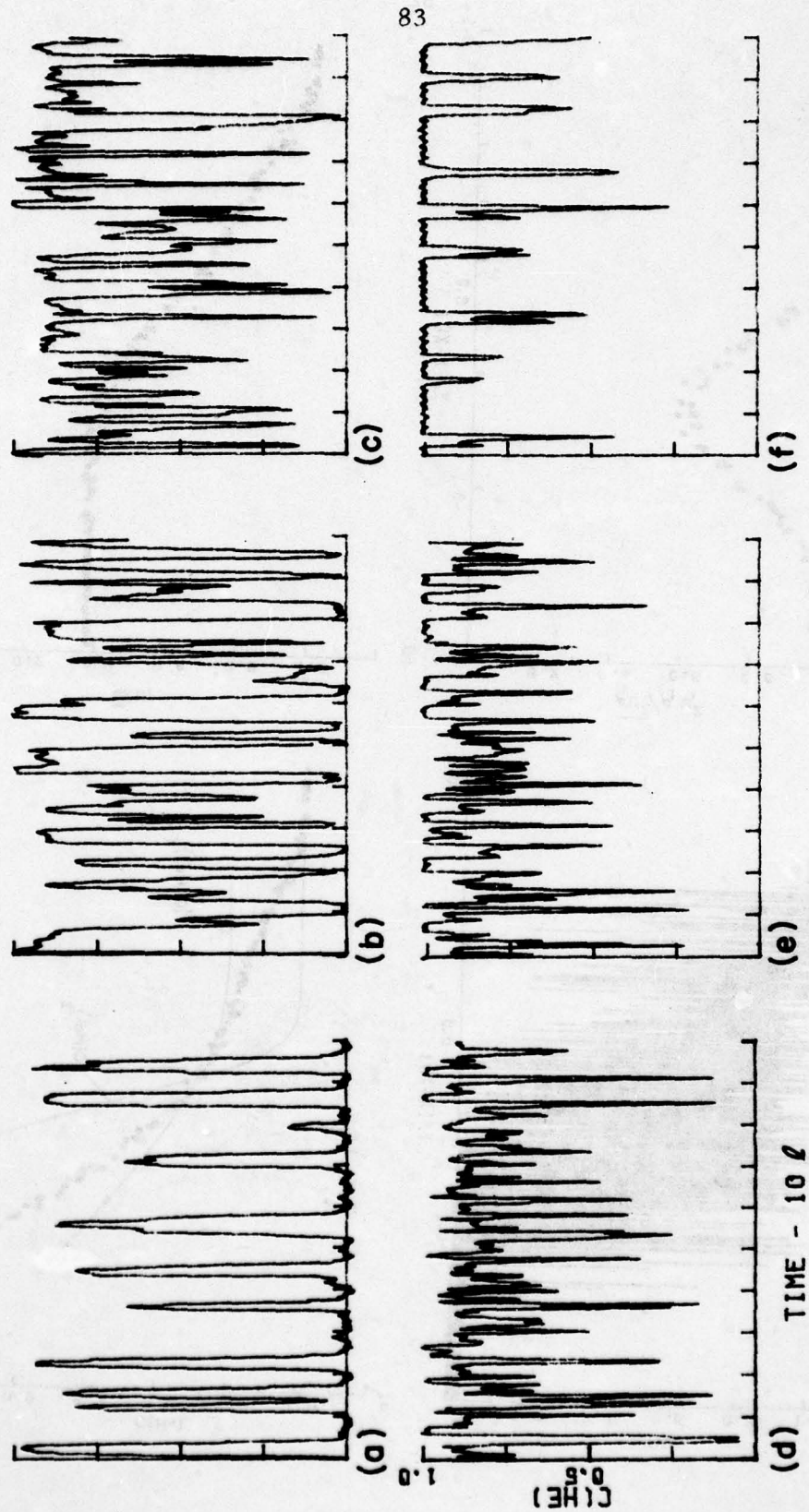


FIG. 4 TIME HISTORIES; $r = 0.38$, $s = 7.0$; $\eta = -.10, -.04, -.01, .02, .05$;
 $\ell \doteq$ SCALE OF LARGE STRUCTURES

AD-A036 349

PURDUE UNIV LAFAYETTE IND PROJECT SQUID HEADQUARTERS

F/G 20/4

AN EXPERIMENTAL INVESTIGATION OF MIXING IN TWO-DIMENSIONAL TURB--ETC(U)

DEC 76 J H KONRAD

N00014-75-C-1143

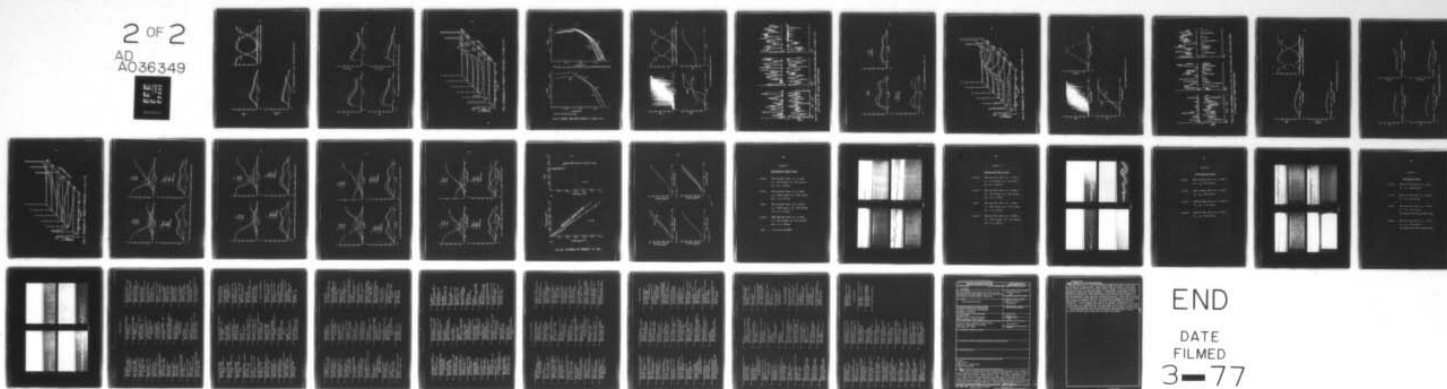
UNCLASSIFIED

SQUID-CIT-8-PU

NL

2 OF 2

AD
A036349



END

DATE
FILMED
3-77

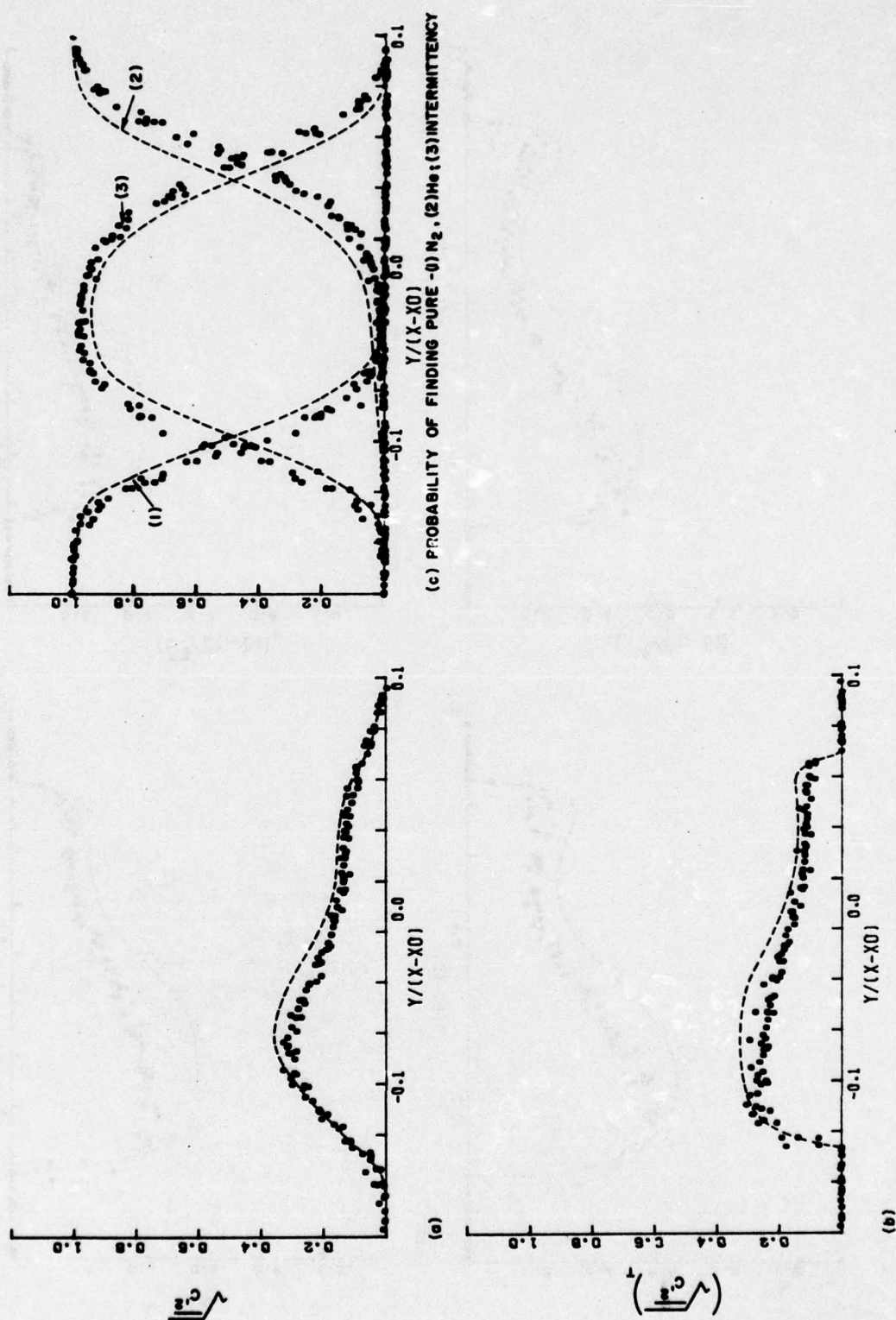


FIG. 5 TRAVERSE PROFILES; $r=0.38$, $s=7.0$; POINTS- Re_c^+ , DASHED- Re_c^-

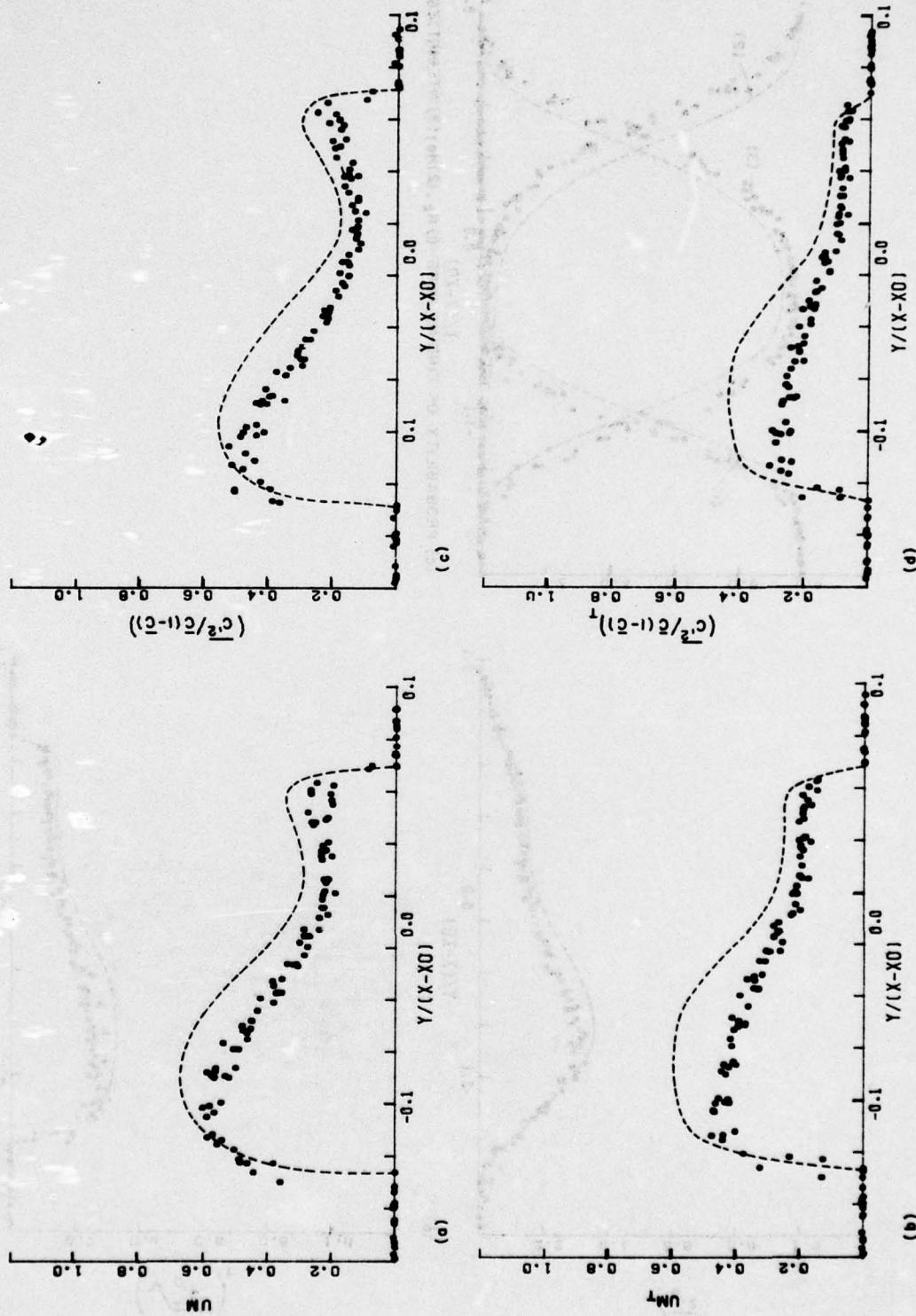


FIG. 6 UNMIXEDNESS PROFILES; $r = 0.38$, $s = 70$; POINTS - Re_C^+ , DASHED - Re_C^-

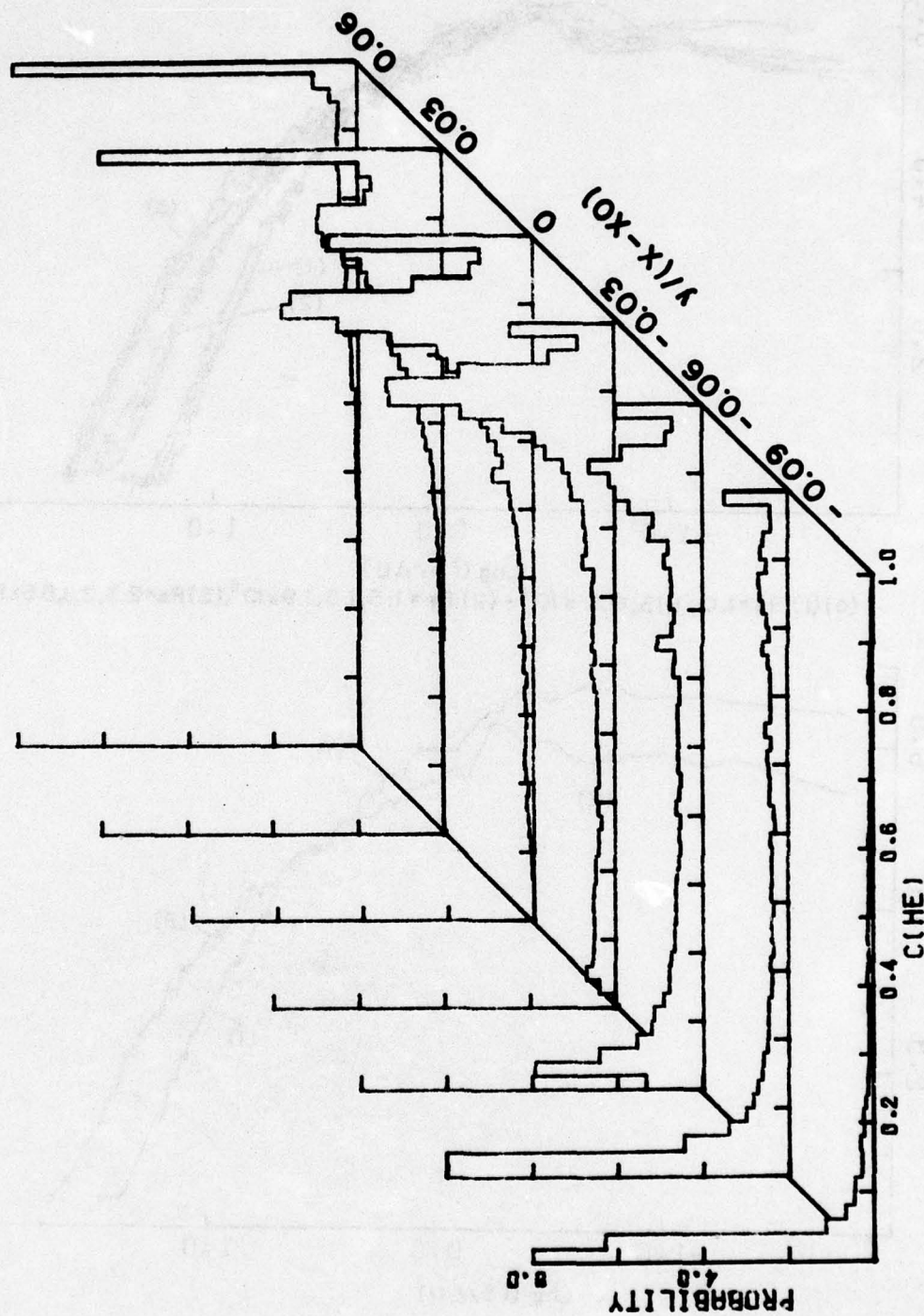
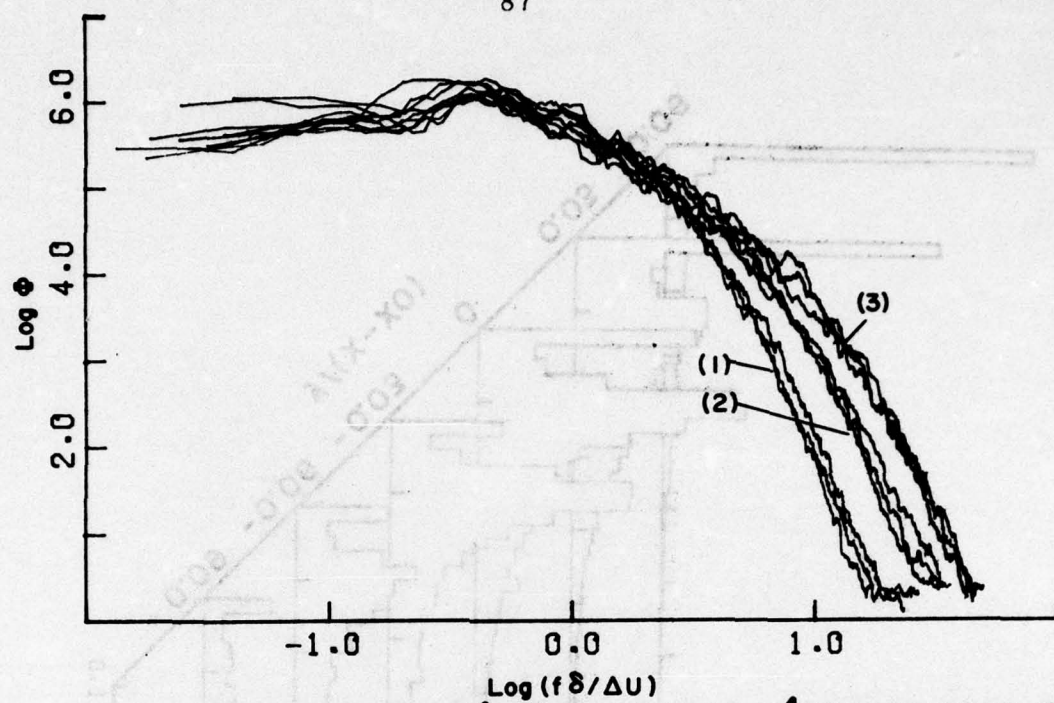
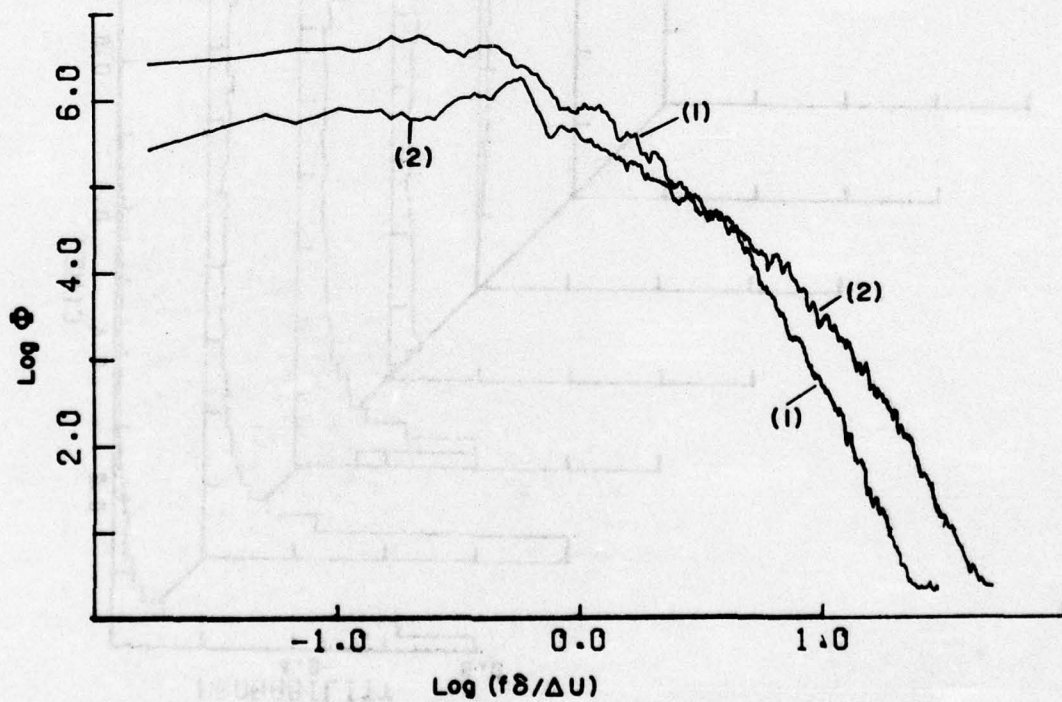


FIG.7 PROBABILITY DENSITY FUNCTION; $r = 0.38$, $s = 7.0$

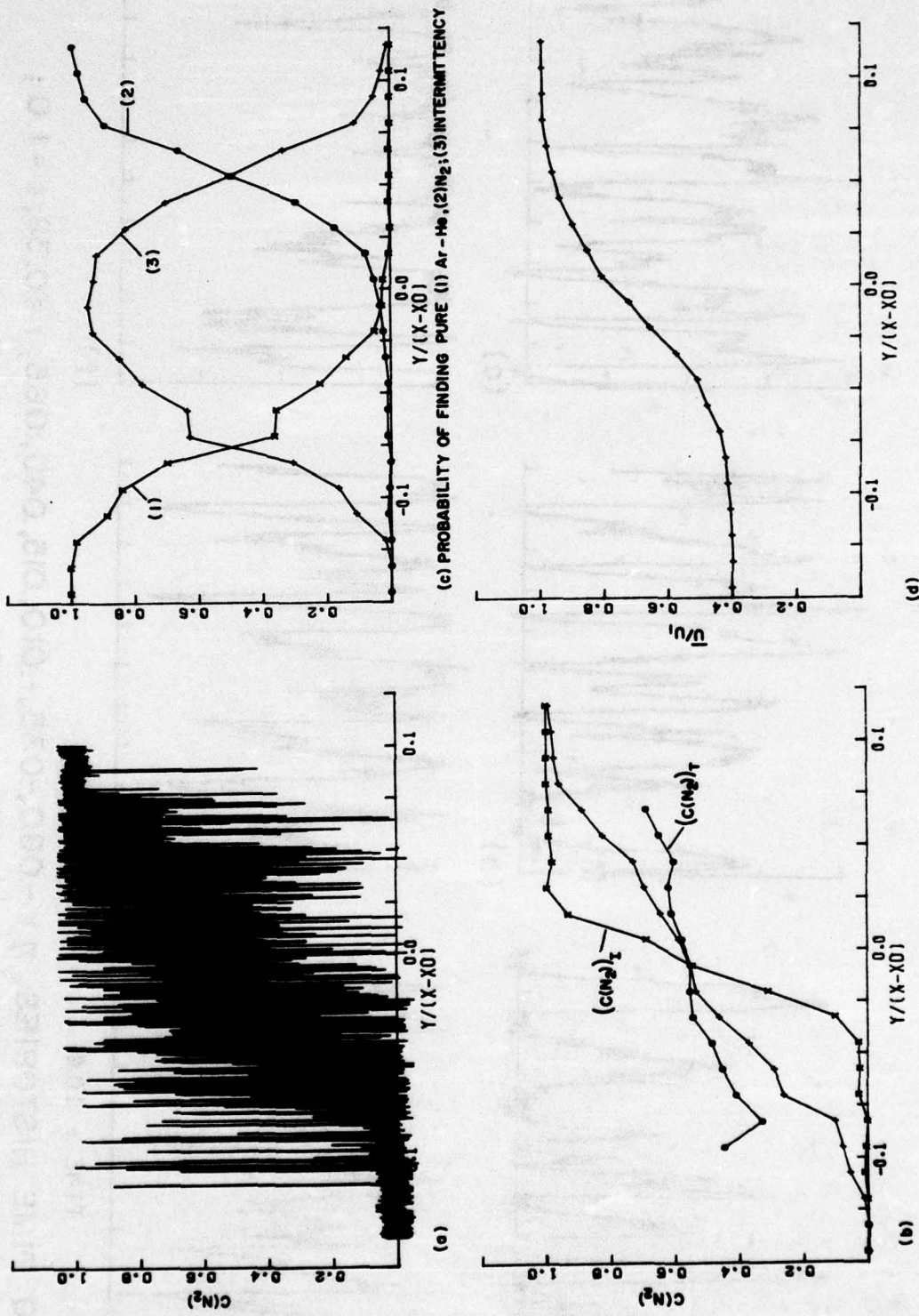


(a) (1) $\text{Re} = 1.0, 1.13, 0.6 \times 10^4$; (2) $\text{Re} = 1.5, 1.8, 1.9 \times 10^4$; (3) $\text{Re} = 2.3, 2.8, 5.5 \times 10^4$



(b) (1) $\eta = -0.10$, (2) $\eta = 0.00$

FIG. 8 POWER SPECTRUM CURVES; $r = 0.38, s = 7.0$

FIG. 9 TRAVERSE PROFILES; $r = 0.38, s = 1.0$

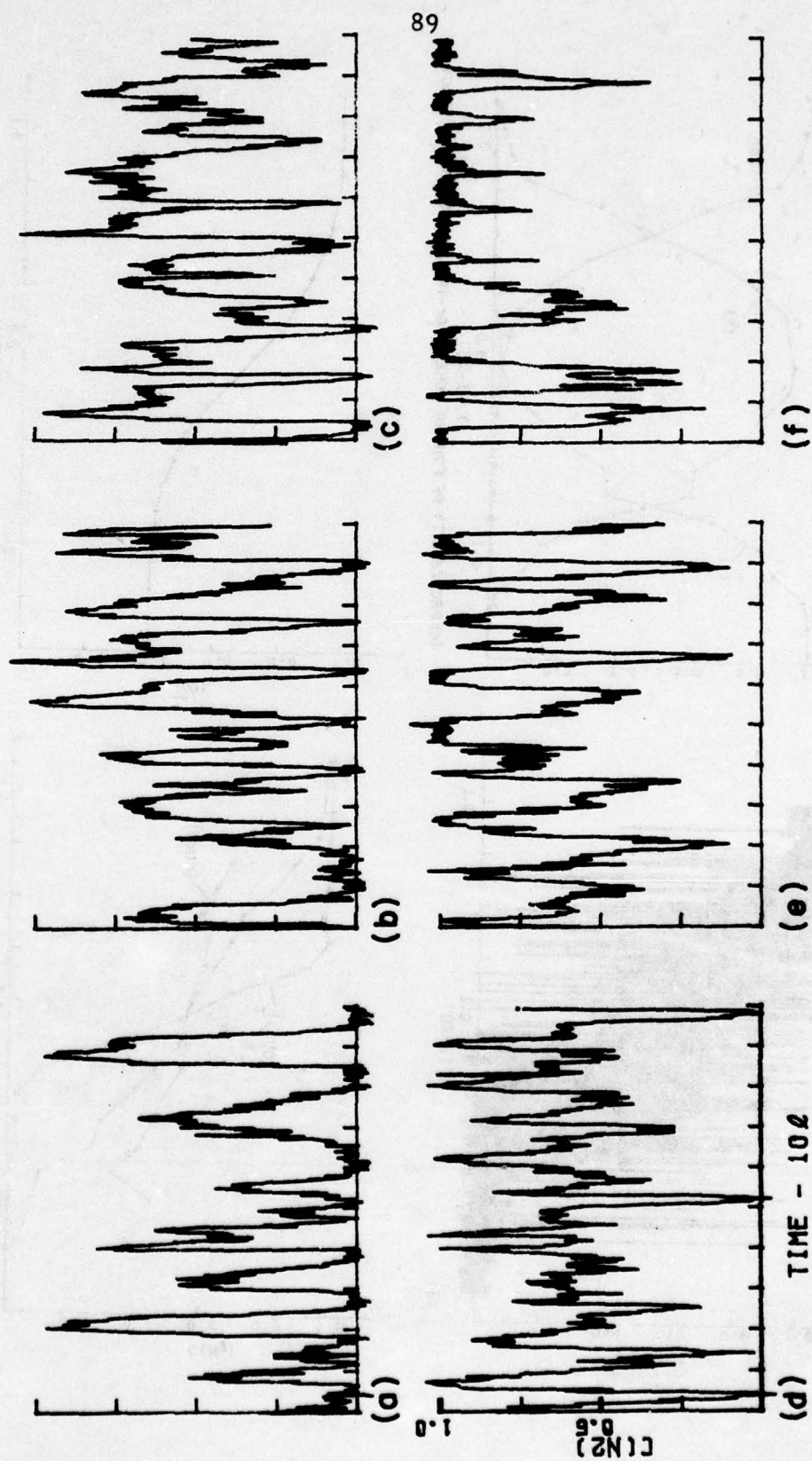
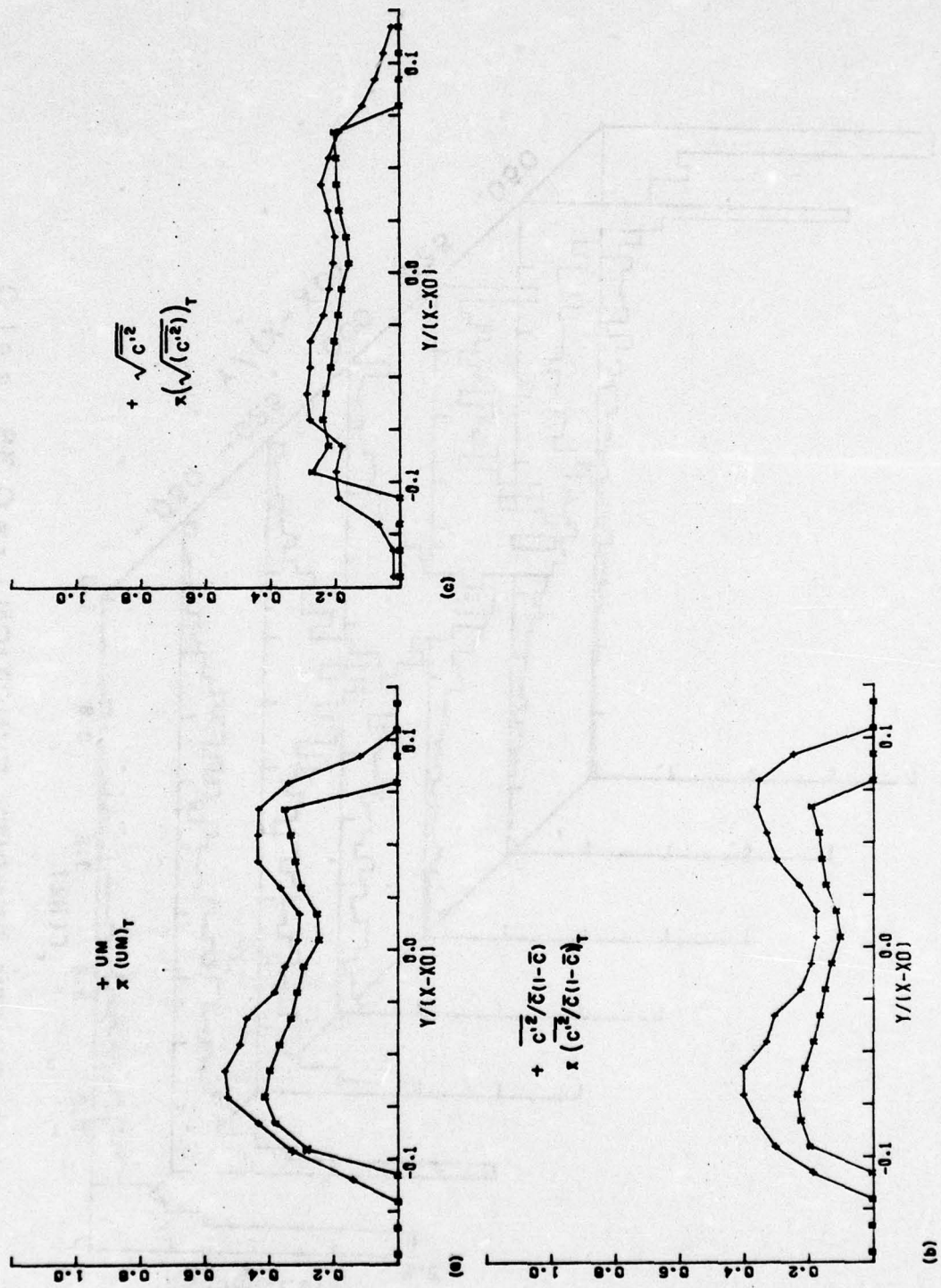


FIG.10 TIME HISTORIES, $\eta = -0.060, -0.035, -0.010, 0.015, 0.040, 0.065$; $r = 0.38, s = 1.0$;
 $l \neq$ SCALE OF LARGE STRUCTURES

FIG. II UNMIXEDNESS PROFILES; $r = 0.38$, $s = 1.0$

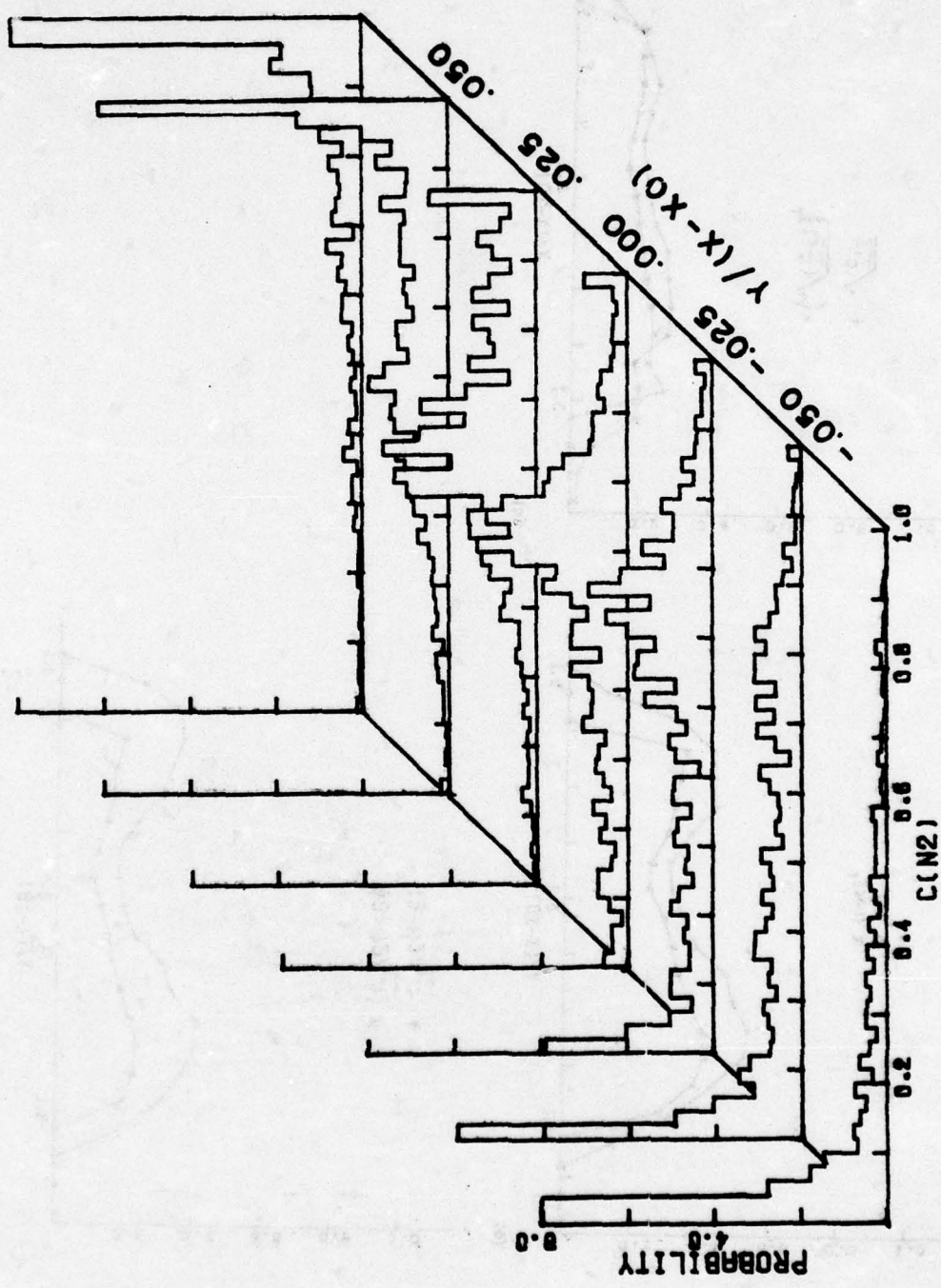
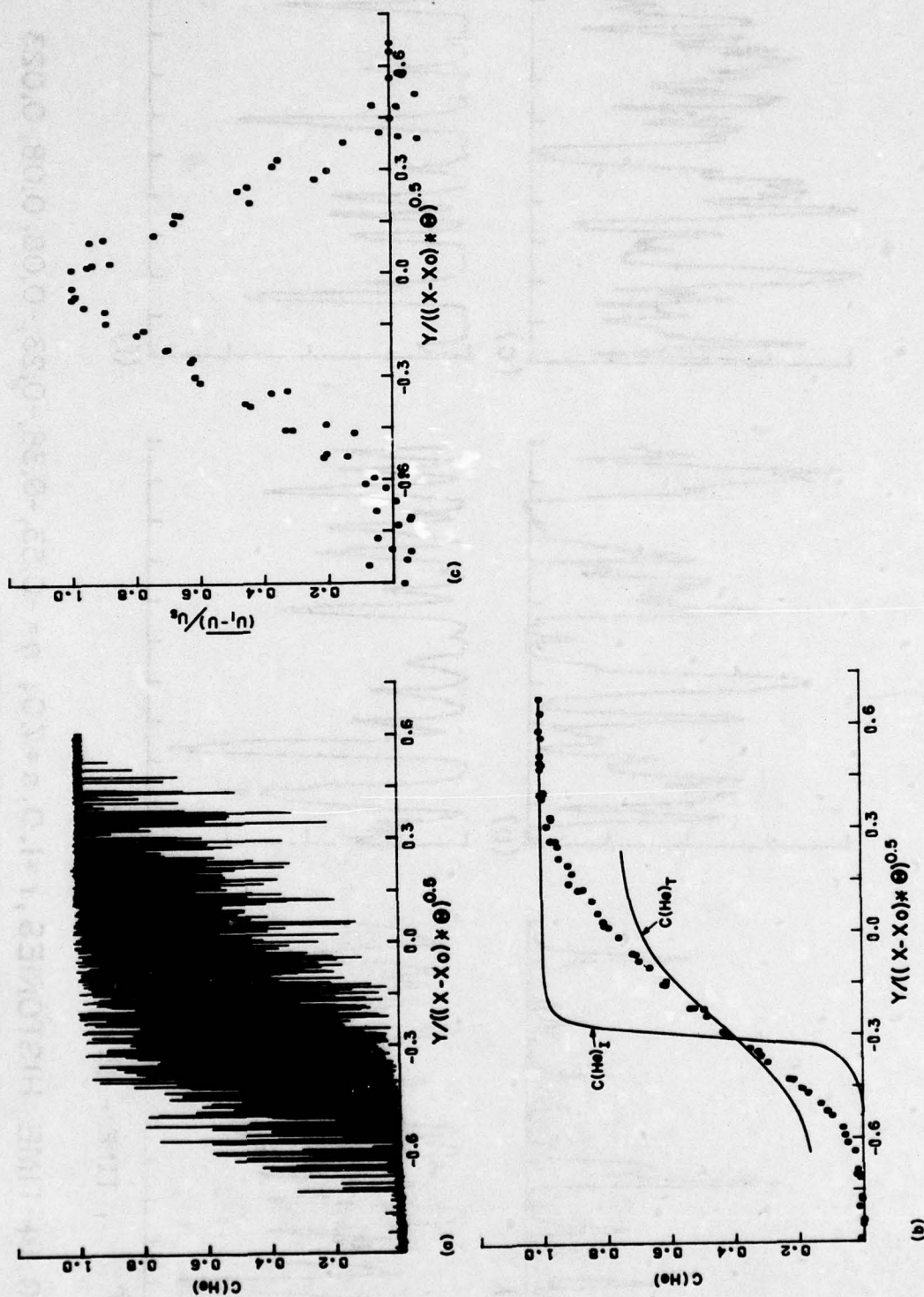


FIG. 12 PROBABILITY DENSITY FUNCTION ; $r = 0.38$, $s = 1.0$

FIG.13 TRAVERSE PROFILES; $r=1.0$, $s=7.0$

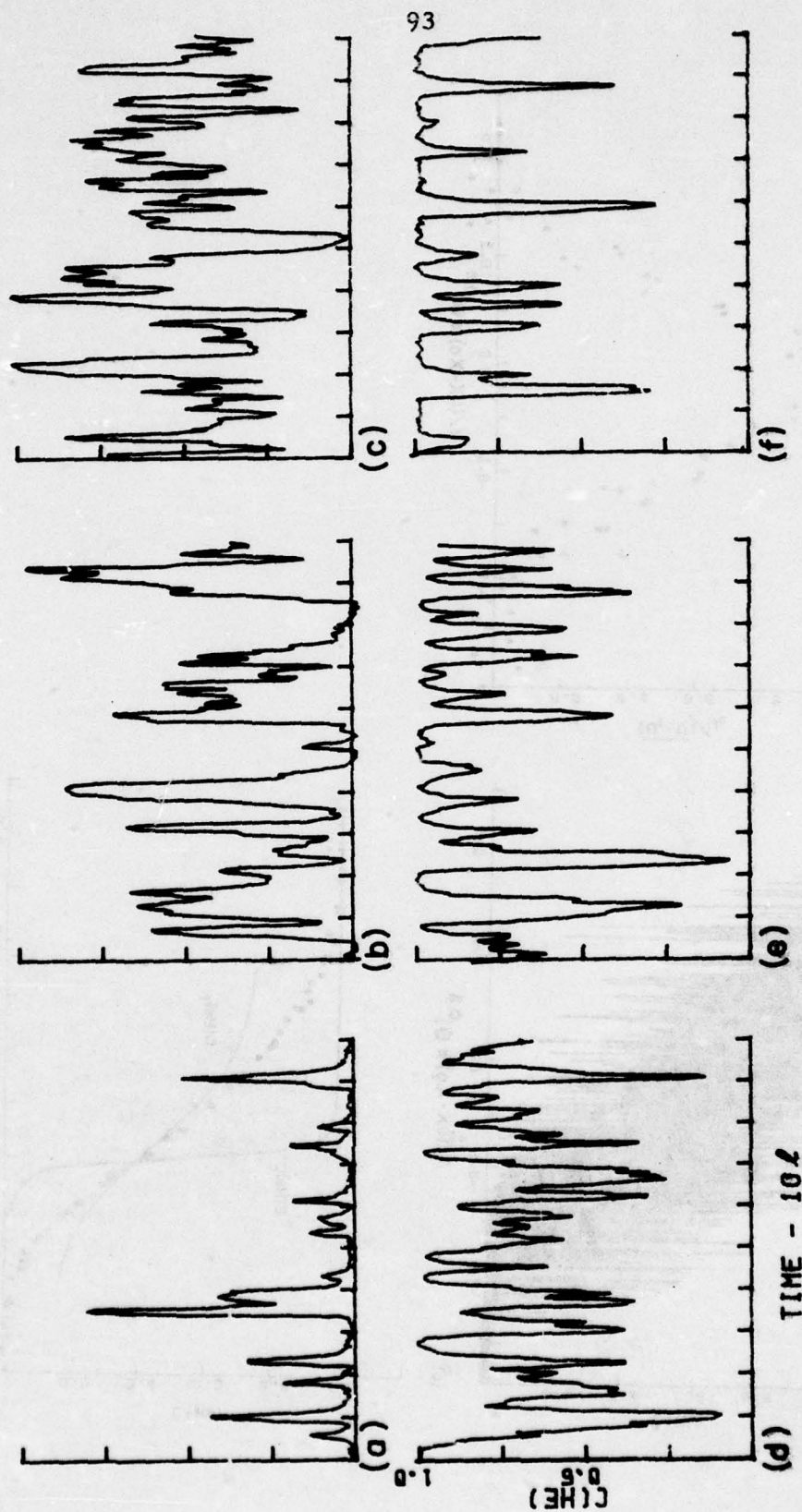


FIG. 14 TIME HISTORIES, $r=1.0$, $s=7.0$; $\eta = -0.53, -0.38, -0.23, -0.08, 0.08, 0.023$
 $l \doteq$ SCALE OF LARGE STRUCTURE

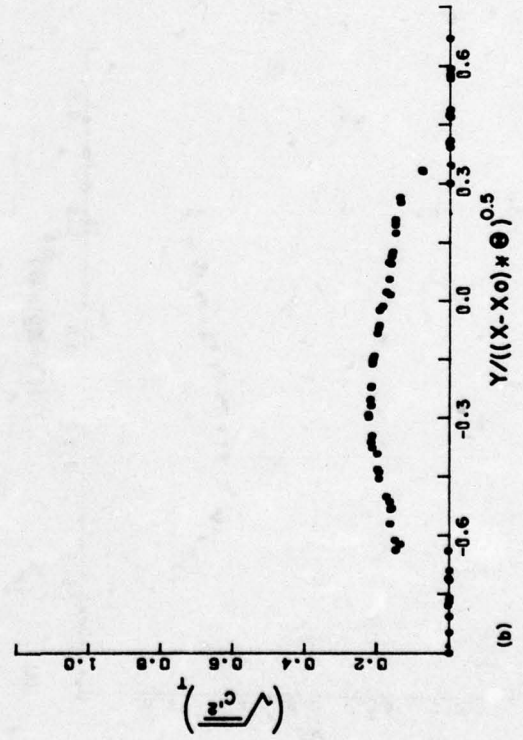
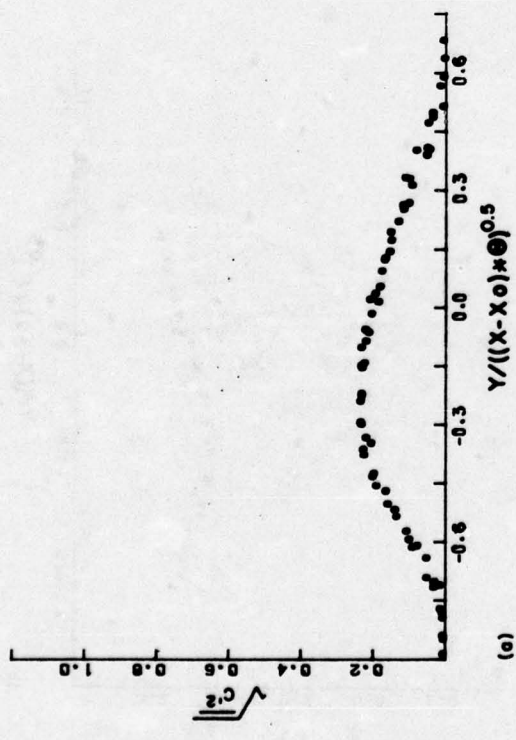
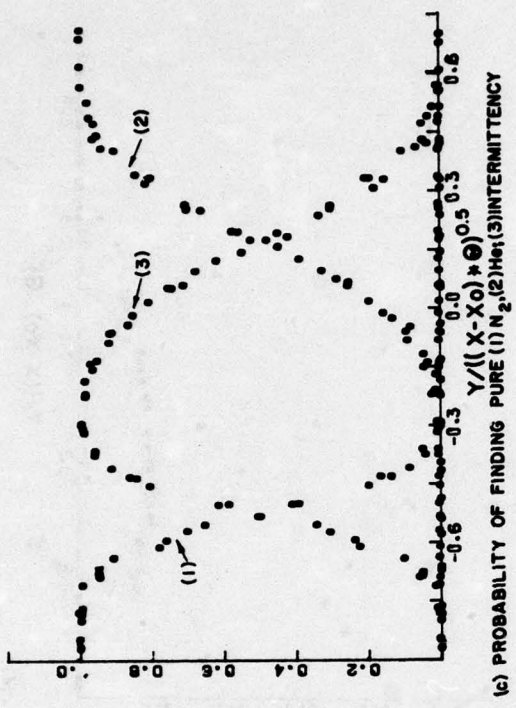
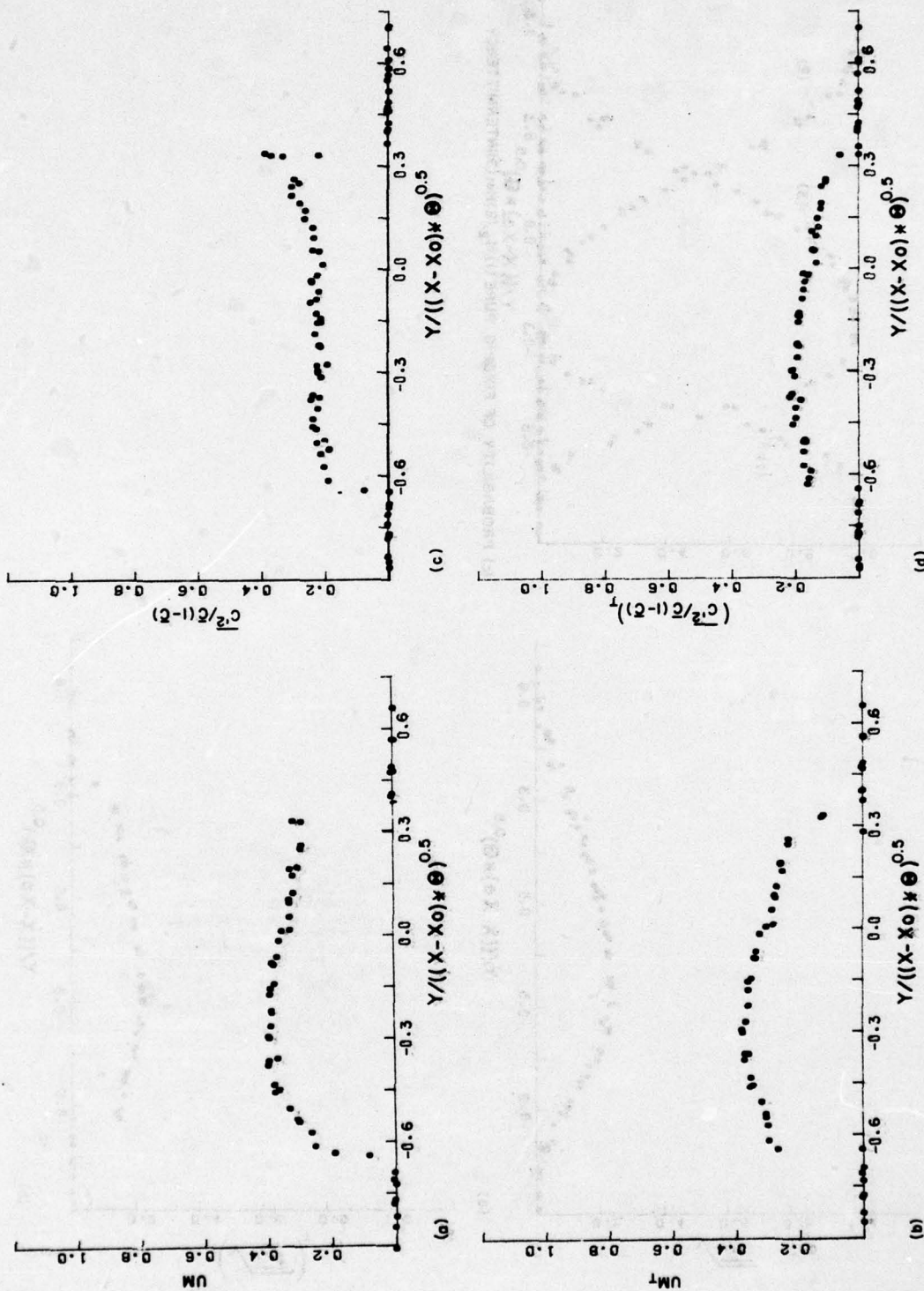


FIG. 15 TRAVERSE PROFILES, $r=1.0$, $s=7.0$

FIG. 16 UNMIXEDNESS PROFILES; $r=1.0$, $s=7.0$

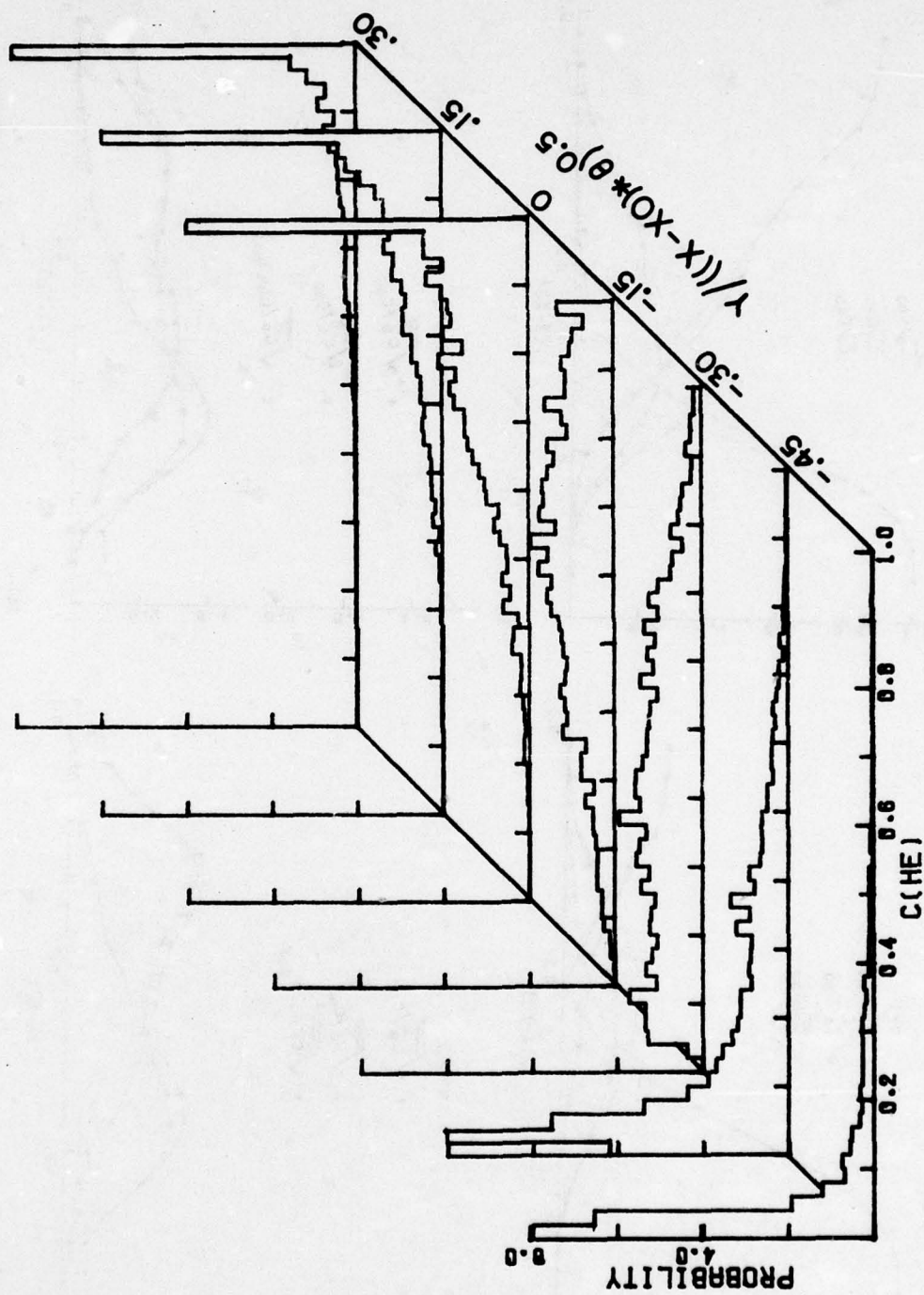


FIG. 17 PROBABILITY DENSITY FUNCTION; $r = 1.0$, $s = 7.0$

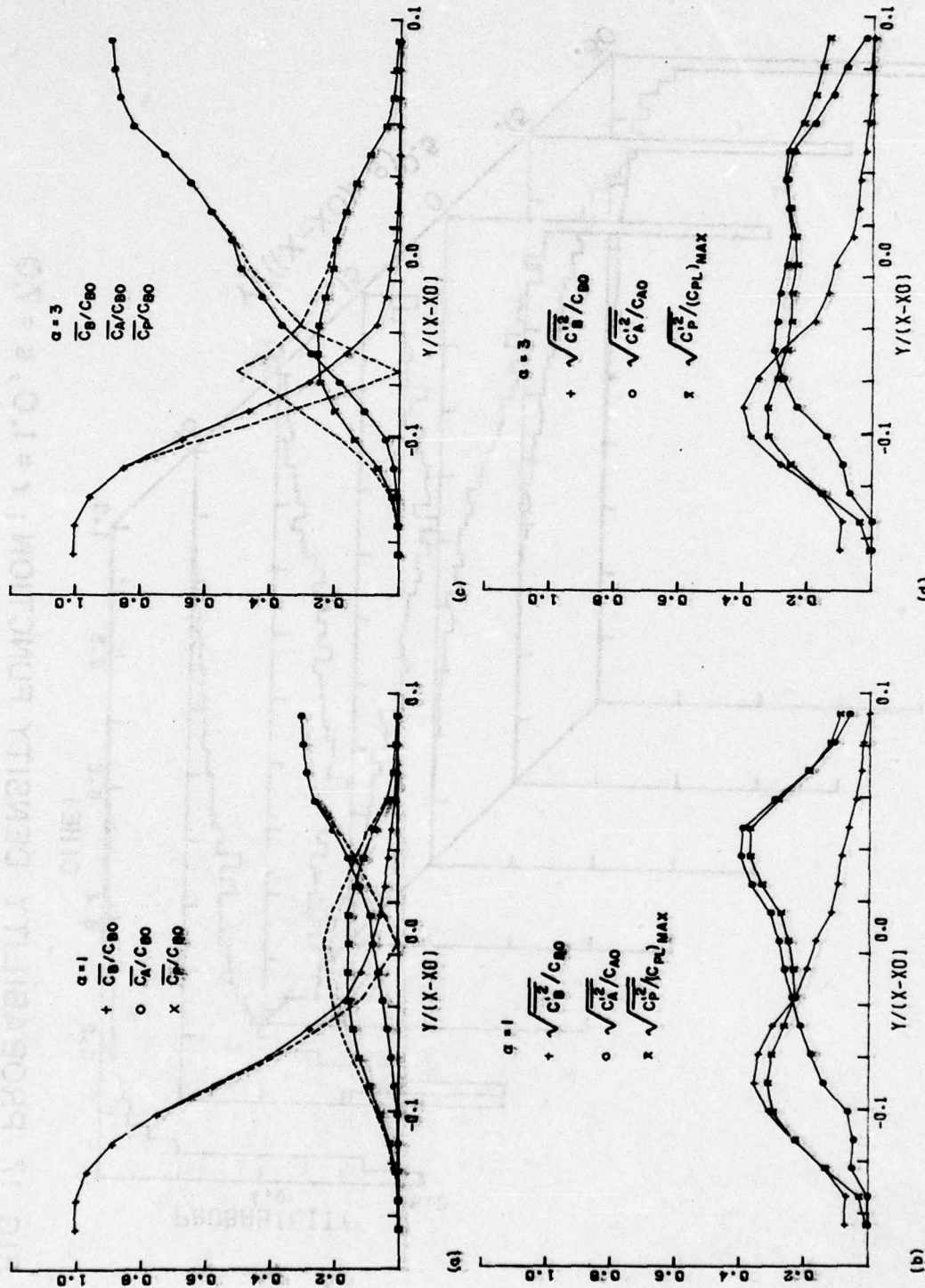


FIG. 18 CHEMICALLY REACTING SHEAR LAYER PROFILES, $r = 0.38, s = 70, Re_c^\dagger$; DASHED - "LAMINAR" SOLUTION

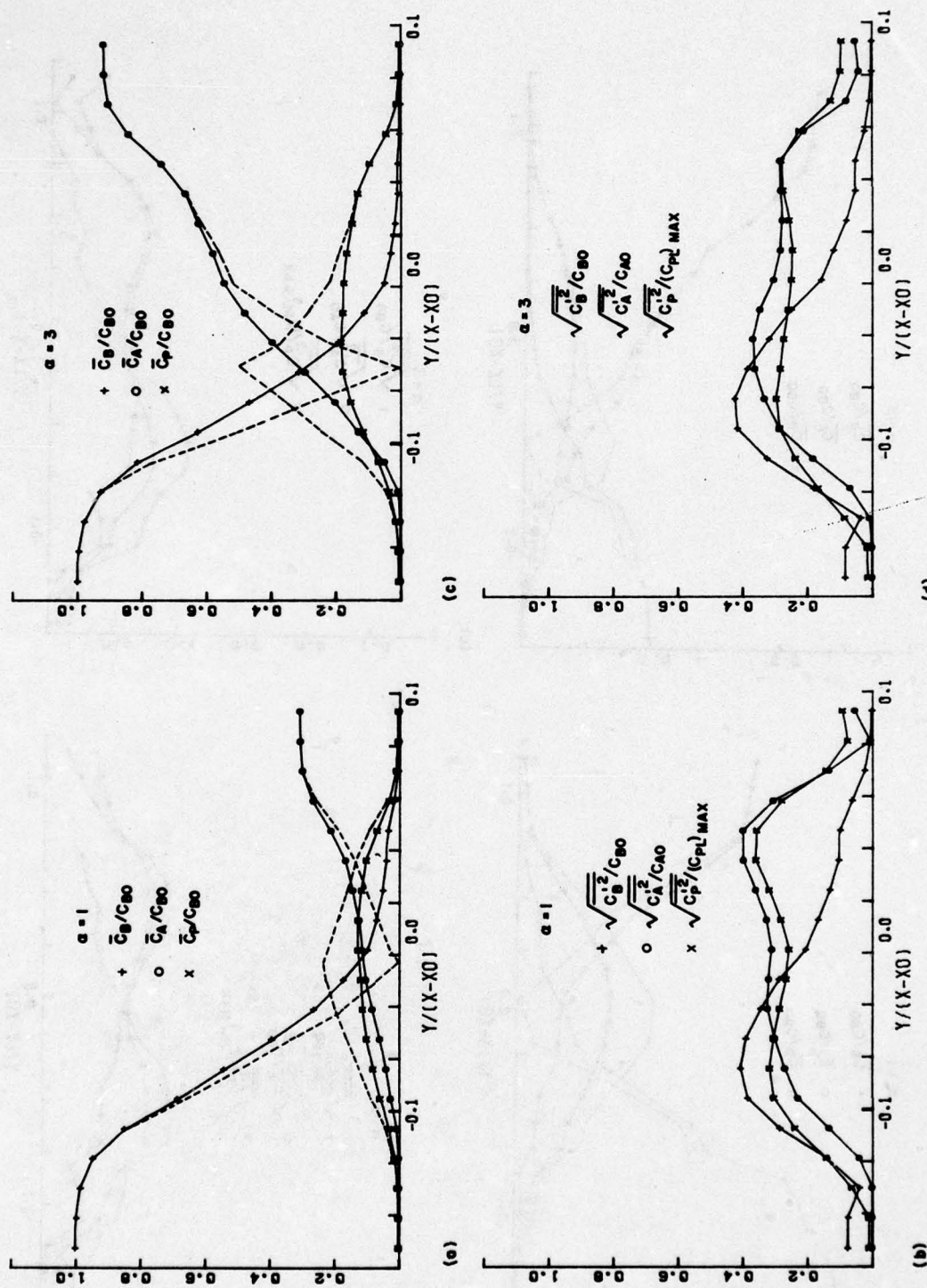


FIG. 19 CHEMICALLY REACTING SHEAR LAYER PROFILES; $r = 0.38$, $s = 7.0$; Re_c^- ; DASHED-"LAMINAR" SOLUTION

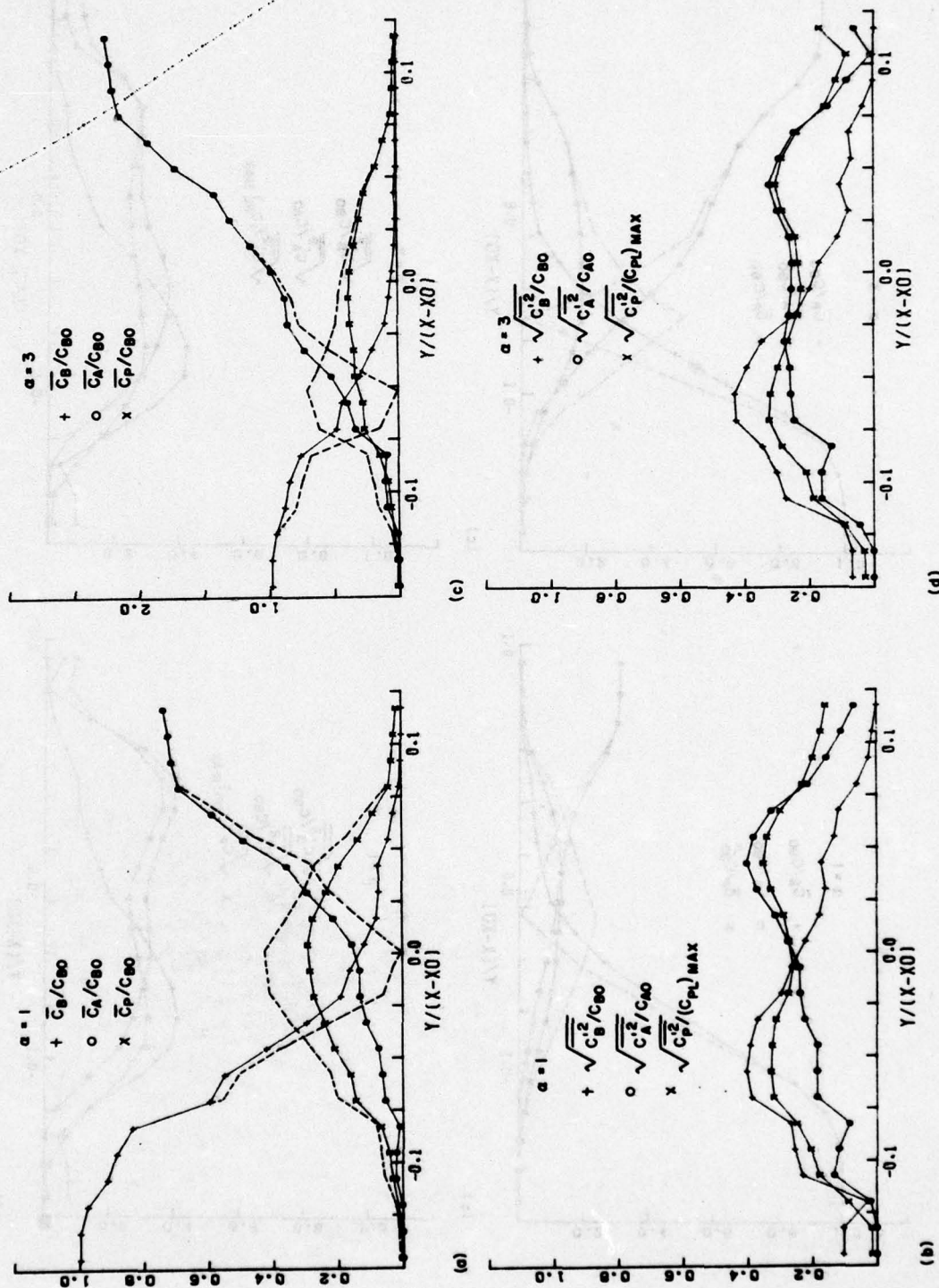


FIG. 20 CHEMICALLY REACTING SHEAR LAYER PROFILES; $r = 0.38$, $s = 1.0$; DASHED - "LAMINAR" SOLUTION

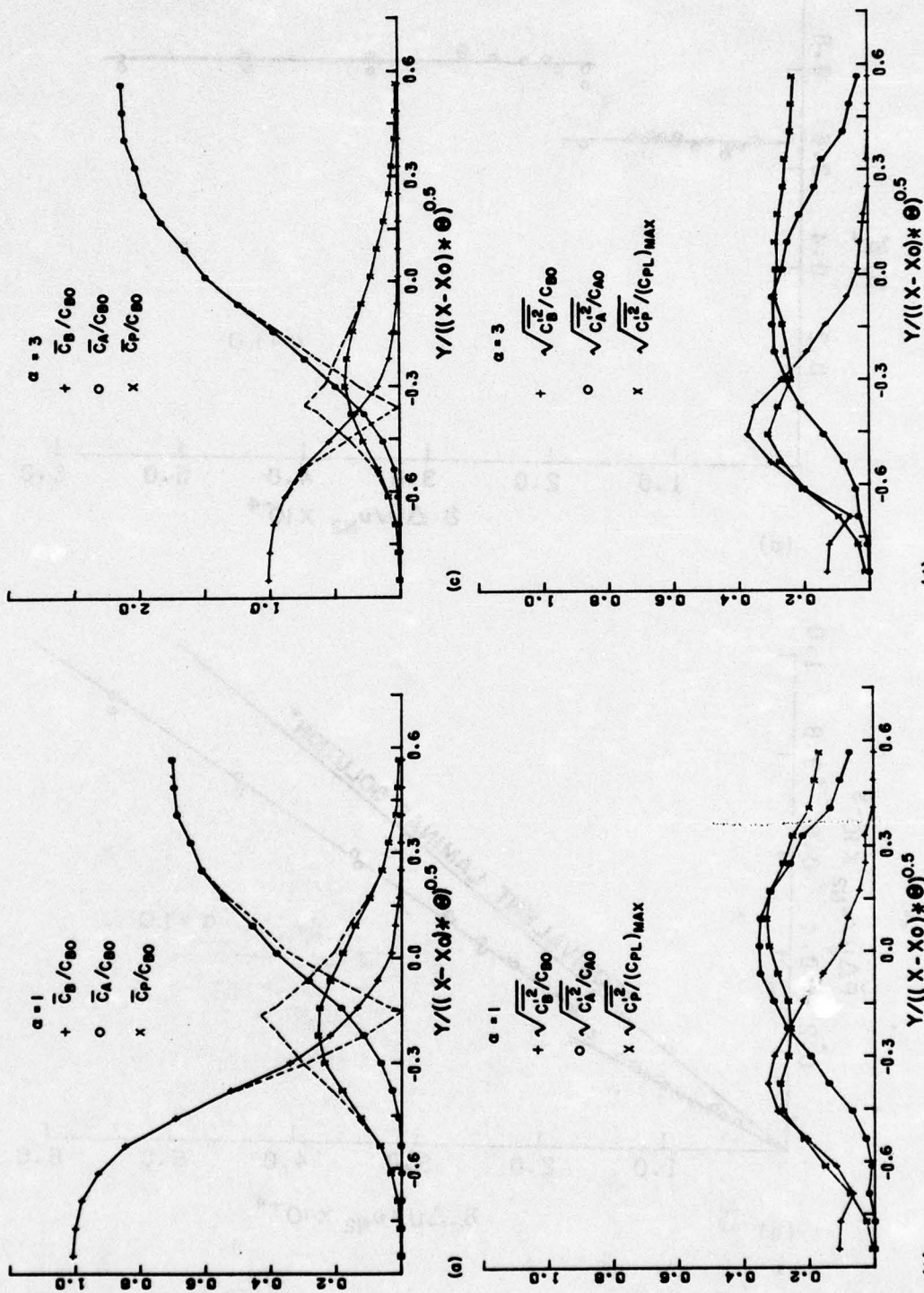


FIG. 21 CHEMICALLY REACTING WAKE PROFILES; $r = 1.0$, $s = 7.0$; DASHED - "LAMINAR" SOLUTION

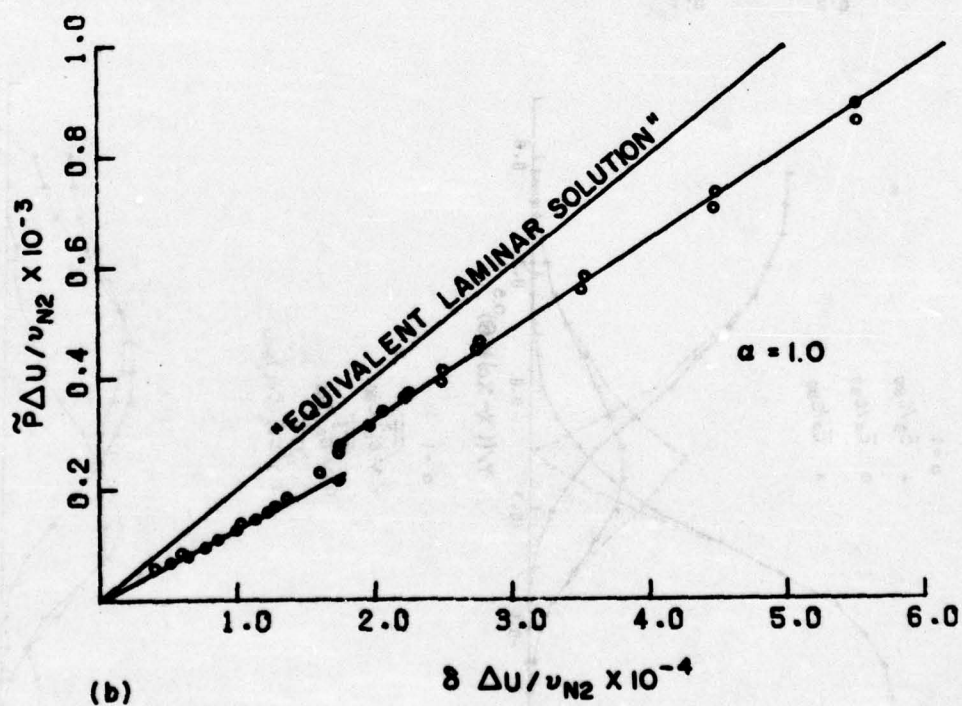
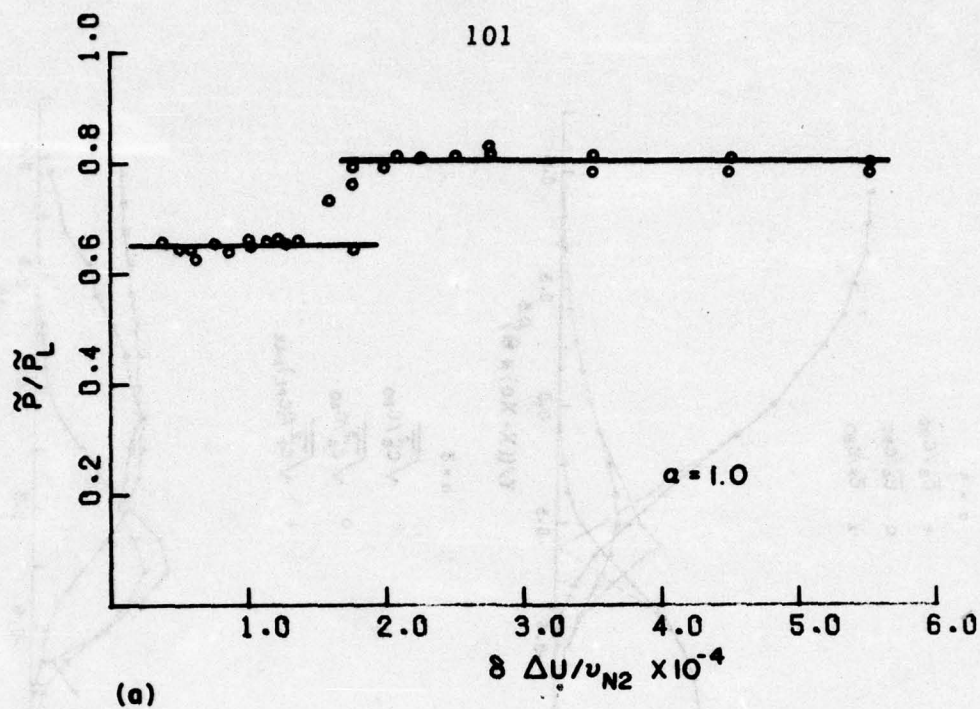


FIG. 22 INTEGRAL OF PRODUCT VS. Re_δ

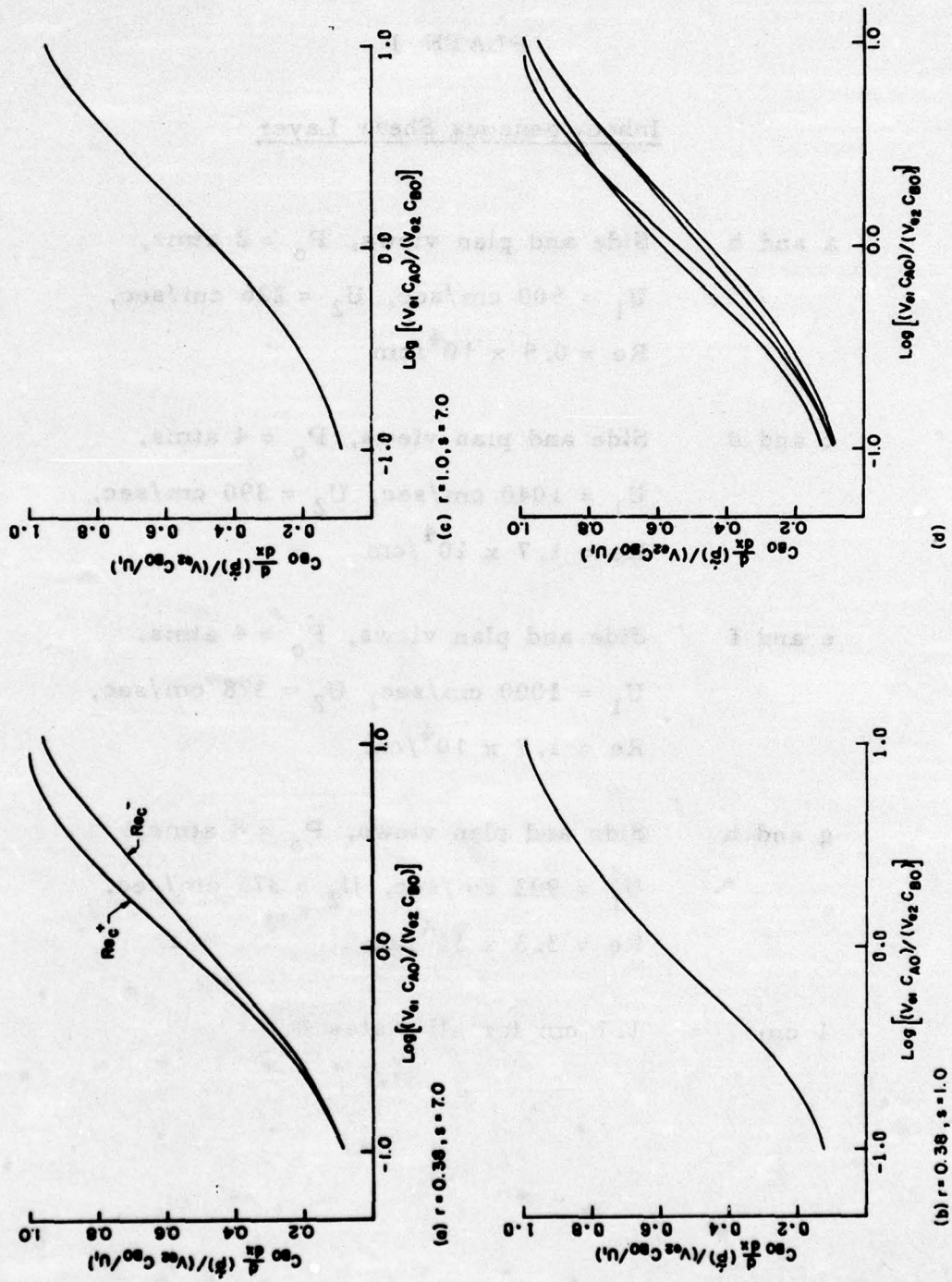


FIG. 23

PLATE 1

Inhomogeneous Shear Layer

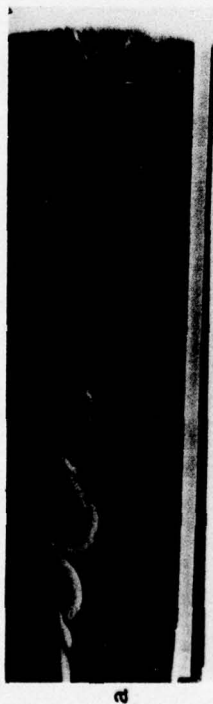
a and b Side and plan views, $P_0 = 2$ atms,
 $U_1 = 600$ cm/sec, $U_2 = 226$ cm/sec,
 $Re = 0.5 \times 10^4$ /cm

c and d Side and plan views, $P_0 = 4$ atms,
 $U_1 = 1040$ cm/sec, $U_2 = 390$ cm/sec,
 $Re = 1.7 \times 10^4$ /cm

e and f Side and plan views, $P_0 = 4$ atms,
 $U_1 = 1000$ cm/sec, $U_2 = 378$ cm/sec,
 $Re = 1.7 \times 10^4$ /cm

g and h Side and plan views, $P_0 = 8$ atms,
 $U_1 = 993$ cm/sec, $U_2 = 375$ cm/sec,
 $Re = 3.3 \times 10^4$ /cm

1 cm = 1.7 cm for all plates



a



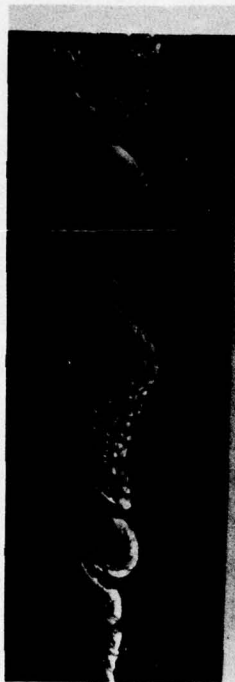
b



c



d



e



f



g



h

Plate 1

PLATE 2

Homogeneous Shear Layer

- a and b Plan and side views, $P_o = 4$ atms,
 $U_1 = 250$ cm/sec, $U_2 = 95$ cm/sec,
 $Re = 0.4 \times 10^4/cm$
- c and d Plan and side views, $P_o = 4$ atms,
 $U_1 = 500$ cm/sec, $U_2 = 189$ cm/sec,
 $Re = 0.8 \times 10^4/cm$
- e and f Plan and side views, $P_o = 4$ atms,
 $U_1 = 1000$ cm/sec, $U_2 = 378$ cm/sec,
 $Re = 1.7 \times 10^4/cm$
- g and h Plan and side views, $P_o = 8$ atms,
 $U_1 = 1000$ cm/sec, $U_2 = 378$ cm/sec,
 $Re = 3.3 \times 10^4/cm$

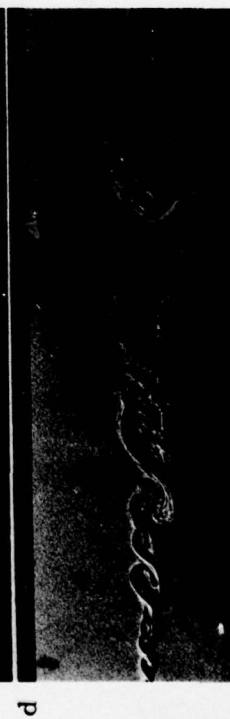
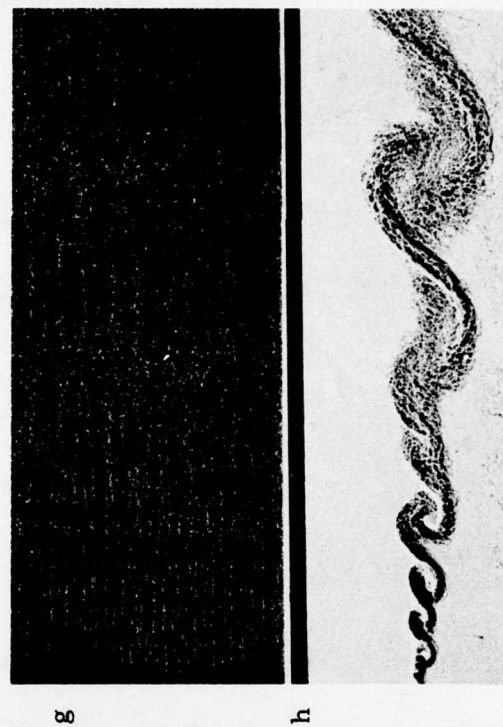
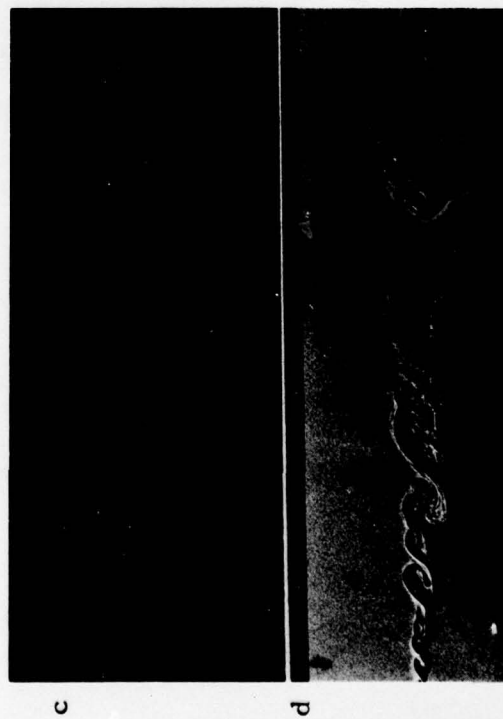
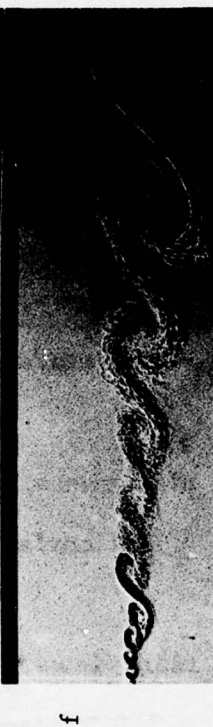
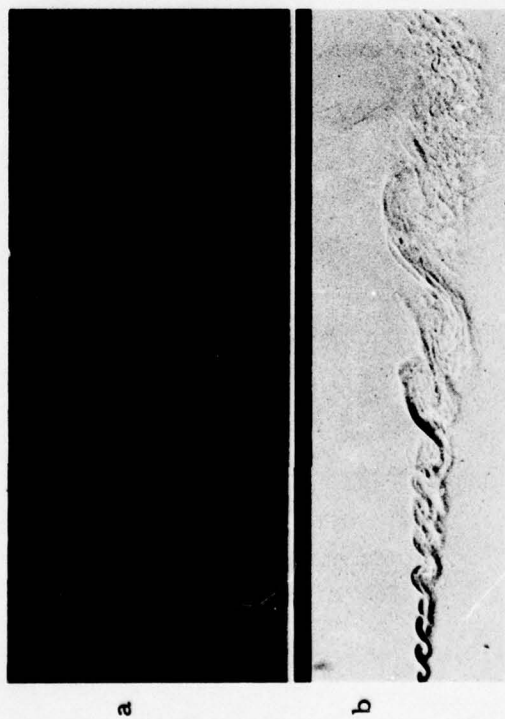


Plate 2

PLATE 3

Inhomogeneous Wake

- a and b Side and plan views, $P_o = 2$ atms,
 $U_1 = U_2 = 306$ cm/sec
- c and d Side and plan views, $P_o = 4$ atms,
 $U_1 = U_2 = 400$ cm/sec
- e and f Side and plan views, $P_o = 4$ atms,
 $U_1 = U_2 = 710$ cm/sec
- g and h Side and plan views, $P_o = 7$ atms,
 $U_1 = U_2 = 900$ cm/sec

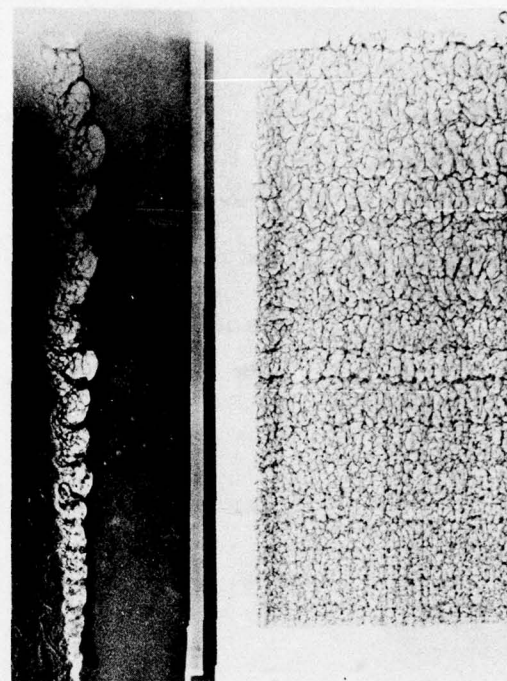
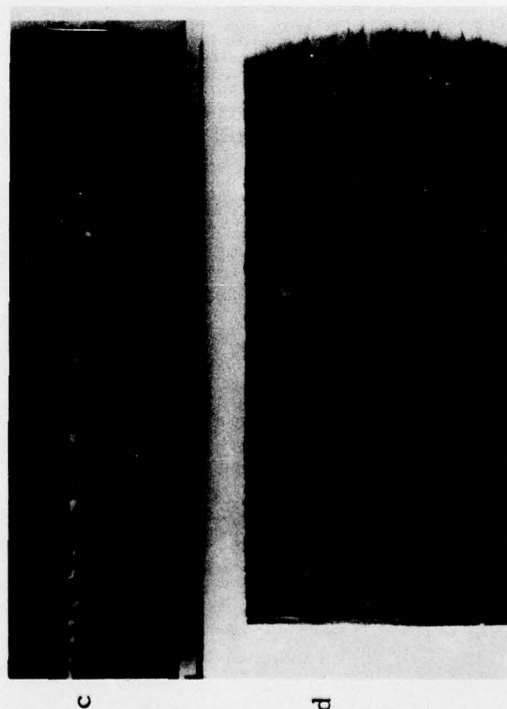
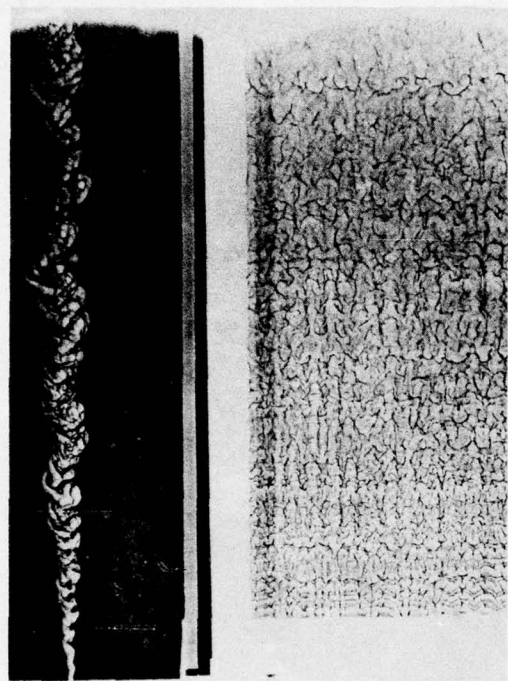


Plate 3

PLATE 4

Homogeneous Wake

- a and b Plan and side views, $P_o = 1 \text{ atm}$,
 $U_1 = U_2 = 1000 \text{ cm/sec}$
- c and d Plan and side views, $P_o = 8 \text{ atms}$,
 $U_1 = U_2 = 960 \text{ cm/sec}$
- e and f Plan and side views, $P_o = 4 \text{ atms}$,
 $U_1 = U_2 = 100 \text{ cm/sec}$,
one-quarter inch thick splitter plate
- g and h Plan and side views, $P_o = 4 \text{ atms}$,
 $U_1 = U_2 = 600 \text{ cm/sec}$,
one-quarter inch thick splitter plate

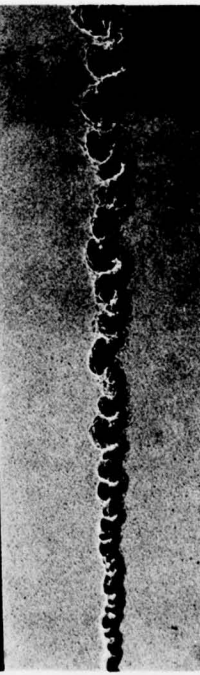
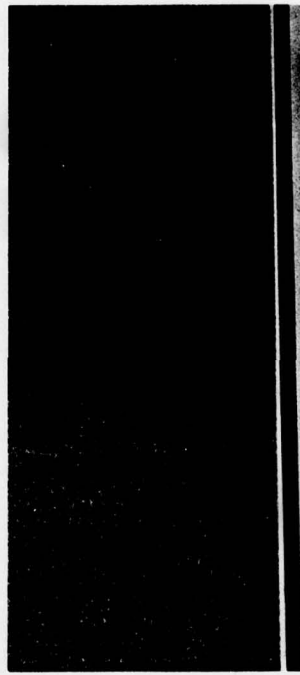
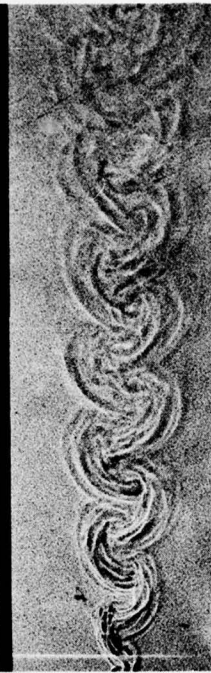
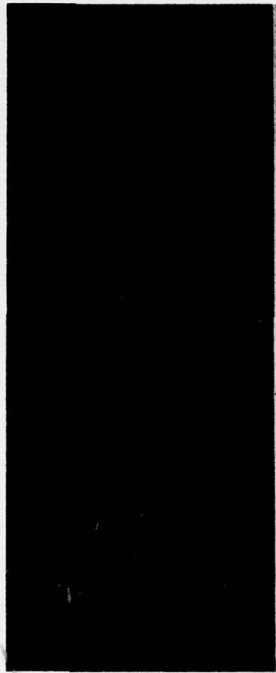
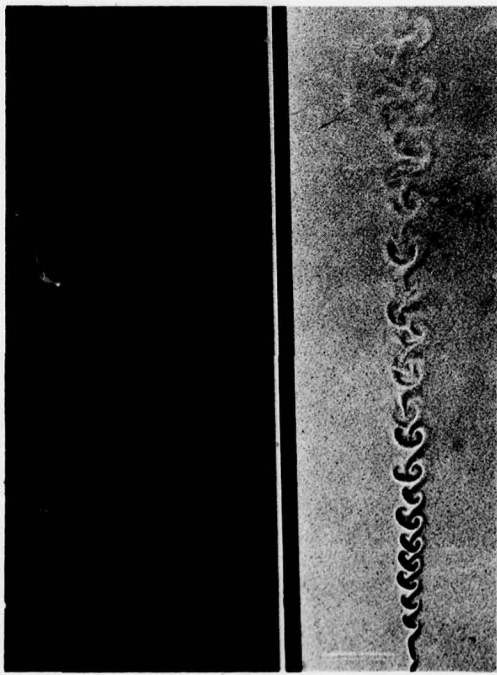


Plate 4

GOVERNMENT AGENCIES

1. British Embassy
3100 Massachusetts Avenue, N.W.
Washington, D.C. 20008
ATTN: Mr. J. Barry Jamieson
Propulsion Officer
2. Central Intelligence Agency
Washington, D.C. 20505
ATTN: CRS/ADD/Publications
3. Institute for Defense Analyses
400 Army-Navy Drive
Arlington, Virginia 22202
ATTN: Dr. Hans G. Wolfhard,
Sen. Staff
4. Defense Documentation Center
Cameron Station
Alexandria, Virginia 22314
5. EPA Technical Center
Research Triangle Park
North Carolina 27711
ATTN: Dr. W. Herget, P-222
6. Esso Research and Engineering Company
Government Research Laboratory
P.O. Box 8
Linden, New Jersey 07036
ATTN: Dr. William F. Taylor
7. Arnold Air Force Station
Tennessee 36389
ATTN: AEDC (DYF)
8. Arnold Air Force Station
Tennessee 37389
ATTN: R.E. Smith, Jr., Chief
T-Cells Division
Engine Test Facility
9. Air Force Aero Propulsion Laboratory
Wright-Patterson Air Force Base
Ohio 45433
ATTN: STINFO Office
10. Air Force Eastern Test Range
MU-135
Patrick Air Force Base
Florida 32925
ATTN: AFETR Technical Library
11. Air Force Office of Scientific Research
Bolling Air Force Base, Building 410
Washington, D.C. 20332
ATTN: Dr. Joseph F. Masi
12. Air Force Aero Propulsion Laboratory
Wright-Patterson AFB, Ohio 45433
ATTN: AFAPL/TBC
Dr. Kervyn Mach
13. Air Force Aero Propulsion Laboratory
Wright-Patterson AFB, Ohio 45433
ATTN: AFAPL/TBC
Francis R. Ostdek
14. Air Force Rocket Propulsion Laboratory
Department of Defense
Edwards AFB, California 93523
ATTN: LKCG (Mr. Selph)
15. U.S. Army Air Mobility Research and
Development Laboratory
Eustis Directorate
Fort Eustis, Virginia 23604
ATTN: Propulsion Division
(SAVDL-EU-PP)
16. U.S. Army Artillery Combat
Developments Agency
Fort Sill, Oklahoma 73503
ATTN: Commanding Officer
17. U.S. Army Missile Command
Redstone Arsenal, Alabama 35809
ATTN: AMSMI-RR
18. U.S. Army Missile Command
Redstone Scientific Information Center
Redstone Arsenal, Alabama 35809
ATTN: Chief, Document Section
19. Indiana State Library
140 North Senate Avenue
Indianapolis, Indiana 46204
ATTN: Patricia Matkovic
Reference Librarian
% Indiana Division
20. NASA Headquarters
600 Independence
Washington, D.C. 20546
ATTN: Dr. Gordon Banerian
21. NASA Headquarters
Aeronautical Propulsion Division
Code RL, Deputy Director
Office of Advanced Research & Technology
Washington, D.C. 20546
ATTN: Mr. Nelson F. Rekos
22. NASA Ames Research Center
Deputy Chief Aeronautics Division
Mail Stop 27-4
Moffett Field, California 94035
ATTN: Mr. Edward W. Perkins
23. NASA Ames Research Center
Aerodynamics Branch 227-8
Moffett Field, California 94305
ATTN: Mr. Ira R. Schwartz
24. NASA Lewis Research Center
21000 Brookpark Road
Cleveland, Ohio 44135
ATTN: D. Morris, Mail Stop 60-3
25. NASA Lewis Research Center
Hypersonic Propulsion Section
Mail Stop 6-1
21000 Brookpark Road
Cleveland, Ohio 44135
ATTN: Dr. Louis A. Povinelli
26. NASA Marshall Space Flight Center
S&E ASTN-P
Huntsville, Alabama 35812
ATTN: Mr. Keith Chandler
27. National Science Foundation
Engineering Energetics
Engineering Division
Washington, D.C. 20550
ATTN: Dr. George Lee
28. National Science Foundation
Engineering Energetics
Engineering Division
Washington, D.C. 20550
ATTN: Dr. M. Ojalvo
29. National Science Foundation
Engineering Energetics
Engineering Division
Washington, D.C. 20550
ATTN: Dr. Royal Rostenbach
30. Naval Air Development Center
Commanding Officer (AD-5)
Warminster, Pennsylvania 18974
ATTN: NADC Library
31. Naval Air Propulsion Test Center (R&T)
Trenton, New Jersey 08628
ATTN: Mr. Al Martino

32. Naval Air Systems Command
Department of the Navy
Washington, D.C. 20360
ATTN: Research Administrator
AIR 310
33. Naval Air Systems Command
Department of the Navy
Washington, D.C. 20360
ATTN: Propulsion Technology Admin.
AIR 330
34. Naval Air Systems Command
Department of the Navy
Washington, D.C. 20360
ATTN: Technical Library Division
AIR 604
35. Naval Ammunition Depot
Research and Development Department
Building 190
Crane, Indiana 47522
ATTN: Mr. B.E. Douda
36. Naval Ordnance Laboratory Commander
White Oak
Silver Springs, Maryland 20910
ATTN: Library
37. Naval Ordnance Systems Command
Department of the Navy
Washington, D.C. 20360
ATTN: ORD 0331
38. Naval Postgraduate School
Department of Aeronautics, Code 57
Monterey, California 93940
ATTN: Dr. Allen E. Fuhs
39. Naval Postgraduate School
Library (Code 2124)
Monterey, California 93940
ATTN: Superintendent
40. Naval Postgraduate School
Monterey, California 93940
ATTN: Library (Code 0212)
41. Office of Naval Research Branch Office
1030 East Green Street
Pasadena, California 91106
ATTN: Dr. Rudolph J. Marcus
42. Office of Naval Research Branch Office
536 South Clark Street
Chicago, Illinois 60605
ATTN: Commander
43. Office of Naval Research Branch Office
495 Summer Street
Boston, Massachusetts 02210
ATTN: Commander
44. Office of Naval Research
Power Branch, Code 473
Department of the Navy
Arlington, Virginia 22217
45. Office of Naval Research
Fluid Dynamics Branch, Code 438
Department of the Navy
Washington, D.C. 22217
ATTN: Mr. Morton Cooper
46. Naval Research Lab
Code 7710
Washington, D.C. 20390
ATTN: W.W. Balwanz
47. Naval Research Laboratory Director
Washington, D.C. 20390
ATTN: Technical Information Division
48. Naval Research Laboratory Director
Washington, D.C. 20390
ATTN: Library Code 2629 (ONRL)
49. Naval Ship Research and Development Center
Annapolis Division
Annapolis, Maryland 21402
ATTN: Library, Code A214
50. Naval Ship Systems Command
Department of the Navy
Washington, D.C. 20360
ATTN: Technical Library
51. Naval Weapons Center Commander
China Lake, California 93555
ATTN: Airbreathing Propulsion Branch
Code 4583
52. Naval Weapons Center
Chemistry Division
China Lake, California 93555
ATTN: Dr. William S. McEwan
Code 605
53. Naval Weapons Center
Commander
China Lake, California 93555
ATTN: Technical Library
54. Naval Weapons Center
Code 608, Thermochemistry Group
China Lake, California 93555
ATTN: Mr. Edward W. Price, Head
55. Naval Weapons Laboratory
Dahlgren, Virginia 22448
ATTN: Technical Library
56. Naval Undersea Research and Development Center
San Diego, California 92132
ATTN: Technical Library
Code 1311D
57. Naval Underwater Systems Center
Fort Trumbull
New London, Connecticut 06320
ATTN: Technical Library
58. Naval Underwater Systems Center
Code 5B-331
Newport, Rhode Island 02840
ATTN: Dr. Robert Lazar
59. Picatinny Arsenal
Commanding Officer
Dover, New Jersey 07801
ATTN: Technical Information Library
60. State Documents Section
Exchange and Gift Division
Washington, D.C. 20540
ATTN: Library of Congress
61. AeroChem Research Laboratories, Inc.
P.O. Box 12
Princeton, New Jersey 08540
ATTN: Dr. Arthur Fontijn
62. AeroChem Research Laboratories, Inc.
P.O. Box 12
Princeton, New Jersey 08540
ATTN: Library
63. Aerojet Liquid Rocket Company
P.O. Box 13222
Sacramento, California 95813
ATTN: Technical Information Center
64. Aeronautical Research Association
of Princeton
50 Washington Road
Princeton, New Jersey 08540
ATTN: Dr. C. Donaldson
65. AeroProjects, Inc.
West Chester
Pennsylvania 19380

U.S. INDUSTRIES AND LABORATORIES

66. The Aerospace Corporation
P.O. Box 92957
Los Angeles, California 90009
ATTN: Mr. Alexander Muraszew
67. Atlantic Research Corporation
5390 Cherokee Avenue
Alexandria, Virginia 22314
ATTN: Dr. Andrej Macek
68. Atlantic Research Corporation
5390 Cherokee Avenue
Alexandria, Virginia 22314
ATTN: Librarian
69. Atlantic Research Corporation
5390 Cherokee Avenue
Alexandria, Virginia 22314
ATTN: Dr. Kermit E. Woodcock
Manager, Propulsion
70. Avco Everett Research Laboratory
Everett, Massachusetts 02149
ATTN: Librarian
71. Avco Lycoming Corporation
550 South Main Street
Stratford, Connecticut 06497
ATTN: Mr. John W. Schrader
72. Ballistics Research Laboratory
Commanding Officer
Aberdeen Proving Ground, Maryland 21005
ATTN: Librarian
73. Battelle
Columbus Laboratories
505 King Avenue
Columbus, Ohio 43201
ATTN: Mr. Abbott A. Putnam
Atmospheric Chemistry &
Combustion Systems Division
74. Beech Aircraft Corporation
9709 East Central
Wichita, Kansas 67201
ATTN: William M. Byrne, Jr.
75. Bell Aerospace Company
P.O. Box 1
Buffalo, New York 14240
ATTN: Technical Library
76. Bureau of Mines
Bartlesville Energy Research Center
Box 1398
Bartlesville, Oklahoma 74003
77. Calspan Corporation
4455 Genessee Street
Buffalo, New York 14221
ATTN: Head Librarian
78. Computer Genetics Corporation
Wakefield, Massachusetts 01880
ATTN: Mr. Donald Leonard
Technical Director
79. Convair Aerospace Division
Manager of Propulsion
P.O. Box 748
Fort Worth, Texas 76101
ATTN: L. H. Schreiber
80. Detroit Diesel Allison Division
P.O. Box 894
Indianapolis, Indiana 46206
ATTN: Dr. Sanford Fleeter
81. Dynalysis of Princeton
20 Nassau Street
Princeton, New Jersey 08540
ATTN: Dr. H.J. Herring
82. Fairchild Industries
Fairchild Republic Division
Farmingdale, New York 11735
ATTN: Engineering Library
83. Flame Research, Inc.
P.O. Box 10502
Pittsburgh, Pennsylvania 15235
ATTN: Dr. John Manton
84. Forest Fire and Engineering Research
Pacific Southwest Forest & Range
Experiment Station
P.O. Box 245
Berkeley, California 94701
ATTN: Assistant Director
85. Garrett Corporation
AIREsearch Manufacturing Company
Sky Harbor Airport
402 South 36th Street
Phoenix, Arizona 85034
ATTN: Mr. Aldo L. Romanin, Mgr.
Aircraft Propulsion Engine
Product Line
86. General Dynamics
Electro Dynamic Division
P.O. Box 2507
Pomona, California 91766
ATTN: Library MZ 620
87. General Dynamics
P.O. Box 748
Fort Worth, Texas 76101
ATTN: Technical Library MZ 2246
88. General Electric Company
AEG Technical Information Center
Mail Drop N-32, Building 700
Cincinnati, Ohio 45215
ATTN: J.J. Brady
89. General Electric Company
SP0-Bldg, 174AE
1000 Western Avenue
West Lynn, Massachusetts 01910
ATTN: Mr. W. Bruce Gist
90. General Electric Space Sciences Lab
Valley Forge Space Technology Center
Room M-9144
P.O. Box 8555
Philadelphia, Pennsylvania 19101
ATTN: Dr. Theodore Baurer
91. General Motors Corporation
Detroit Diesel Allison Division
P.O. Box 894
Indianapolis, Indiana 46206
ATTN: Mr. P.C. Tram
92. General Motors Technical Center
Passenger Car Turbine Development
General Motors Engineering Staff
Warren, Michigan 48090
ATTN: T.F. Nagey, Director
93. Grumman Aerospace Corporation
Manager Space Vehicle Development
Bethpage, New York 11714
ATTN: Mr. O.S. Williams
94. Mr. Daniel L. Harshman
11131 Embassy Drive
Cincinnati, Ohio 45240
95. Hercules Incorporated
Allegany Ballistics Laboratory
P.O. Box 210
Cumberland, Maryland 21502
ATTN: Mrs. Louise S. Derrick
Librarian
96. Hercules Incorporated
P.O. Box 98
Magna, Utah 84044
ATTN: Library 100-H

97. LTV Vought Aeronautics Company
Flight Technology, Project Engineer
P.O. Box 5907
Dallas, Texas 75222
ATTN: Mr. James C. Utterback
98. Lockheed Aircraft Corporation
Lockheed Missiles and Space Company
Huntsville, Alabama 35804
ATTN: John M. Banefield
Supervisor Propulsion
99. Lockheed-Georgia Company
Dept. 72-47, Zone 259
Marietta, Georgia 30060
ATTN: William A. French
100. Lockheed Missiles and Space Company
2251 Hanover Street
Palo Alto, California 94304
ATTN: Palo Alto Library 52-52
101. Lockheed Propulsion Company
Scientific and Technical Library
P.O. Box 111
Redlands, California 92373
ATTN: Head Librarian
102. Los Alamos Scientific Laboratory
P.O. Box 1663
Los Alamos, New Mexico 97544
ATTN: J. Arthur Freed
103. The Marquardt Company
CCI Aerospace Corporation
16555 Saticoy Street
Van Nuys, California 91409
ATTN: Library
104. Martin-Marietta Corporation
P.O. Box 179
Denver, Colorado 90201
ATTN: Research Library 6617
105. Martin-Marietta Corporation
Orlando Division
P.O. Box 5837
Orlando, Florida 32805
ATTN: Engineering Library, mp-30
106. McDonnell Aircraft Company
P.O. Box 516
St. Louis, Missouri 63166
ATTN: Research & Engineering Library
Dept. 218 - Bldg. 101
107. McDonnell Douglas Corporation
Project Propulsion Engineer
Dept. 243, Bldg. 66, Level 25
P.O. Box 516
St. Louis, Missouri 63166
ATTN: Mr. William C. Paterson
108. McDonnell Douglas Astronautics Company
5301 Bolsa Avenue
Huntington Beach, California 92647
ATTN: A3-328 Technical Library
109. Nielsen Engineering and Research, Inc.
510 Clyde Avenue
Mountain View, California 94040
ATTN: Dr. Jack N. Nielsen
110. Northrop Corporation
Ventura Division
1515 Rancho Conejo Boulevard
Newbury Park, California 91230
ATTN: Technical Information Center
111. Mr. J. Richard Perrin
16261 Darcia Avenue
Encino, California 91316
112. Philco-Ford Corporation
Aeronutronic Division
Ford Road
Newport Beach, California 92663
ATTN: Technical Information Center
113. Pratt and Whitney Aircraft
Project Engineer, Advanced
Military System
Engineering Department - 28
East Hartford, Connecticut 06108
ATTN: Mr. Donald S. Rudolph
114. Pratt and Whitney Aircraft Division
United Aircraft Company
400 South Main Street
East Hartford, Connecticut 06108
ATTN: Mr. Dana B. Waring
Manager-Product Technology
115. Pratt and Whitney Aircraft
Program Manager, Advanced
Military Engineer
Engineering Department - 28
East Hartford, Connecticut 06108
ATTN: Dr. Robert I. Strough
116. Pratt and Whitney Aircraft
Florida Research and Development Company
P.O. Box 2691
West Palm Beach, Florida 33402
ATTN: Mr. William R. Alley
Chief of Applied Research
117. Rocket Research Corporation
11441 Willow Road
Redmond, Washington 98052
ATTN: Thomas A. Groudie
118. Rocketdyne Division
North American Rockwell
6633 Canoga Avenue
Canoga Park, California 91304
ATTN: Technical Information Center
D 596-108
119. Sandia Laboratories
P.O. Box 969
Livermore, California 94550
ATTN: Dr. Dan Hartley, Div. 8115
120. Sandia Laboratories
Livermore, California 94550
ATTN: Robert Gallagher
121. Sandia Laboratories
P.O. Box 5800
Albuquerque, New Mexico 87115
ATTN: Technical Library, 3141
122. Solar
2200 Pacific Highway
San Diego, California 92112
ATTN: Librarian
123. Standard Oil Company (Indiana)
P.O. Box 400
Naperville, Illinois 60540
ATTN: R. E. Pritz
124. Stauffer Chemical Company
Richmond, California 94802
ATTN: Dr. J. H. Morgenthaler
125. Teledyne CAE
1330 Laskey Road
Toledo, Ohio 43601
ATTN: Technical Library
126. TRW Systems
One Space Park
Redondo Beach, California 90278
ATTN: Mr. F.E. Fendell (R1/1004)
127. TRW Systems Group
One Space Park
Bldg. 0-1 Room 2080
Redondo Beach, California 90278
ATTN: Mr. Donald H. Lee Manager
128. United Technologies Research Center
East Hartford, Connecticut 06108
ATTN: Librarian
129. Valley Forge Sapce Technology Center
P.O. Box 8555
Philadelphia, Pennsylvania 19101
ATTN: Dr. Bert Zauderer
130. Vought Missiles and Space Company
P.O. Box 6267
Dallas, Texas 75222
ATTN: Library - 3-41000

U.S. COLLEGES AND UNIVERSITIES

131. Boston College
Department of Chemistry
Chestnut Hill, Massachusetts 02167
ATTN: Rev. Donald MacLean, S.J.
Associate Professor
132. Brown University
Division of Engineering
Box D
Providence, Rhode Island 02912
ATTN: Dr. R. A. Dobbins
133. California Institute of Technology
Department of Chemical Engineering
Pasadena, California 91109
ATTN: Professor W. H. Corcoran
134. California Institute of Technology
Jet Propulsion Laboratory
4800 Oak Grove Drive
Pasadena, California 91103
ATTN: Library
135. University of California, San Diego
Dept. of Engineering Physics
P.O. Box 109
La Jolla, California 92037
ATTN: Professor S.S. Penner
136. University of California
School of Engineering and
Applied Science
7513 Boelter Hall
Los Angeles, California 90024
ATTN: Engineering Reports Group
137. University of California
Lawrence Radiation Laboratory
P.O. Box 808
Livermore, California 94550
ATTN: Technical Information Dept. L-3
138. University of California
General Library
Berkeley, California 94720
ATTN: Documents Department
139. Case Western Reserve University
10900 Euclid Avenue
Cleveland, Ohio 44106
ATTN: Sears Library - Reports
Department
140. Case Western Reserve University
Division of Fluid Thermal and
Aerospace Sciences
Cleveland, Ohio 44106
ATTN: Professor Eli Reshotko
141. Colorado State University
Engineering Research Center
Fort Collins, Colorado 80521
ATTN: Mr. V. A. Sandborn
142. The University of Connecticut
Department of Mechanical Engineering
U-139
Storrs, Connecticut 06268
ATTN: Professor E. K. Dabora
143. Cooper Union
School of Engineering and Science
Cooper Square
New York, New York 10003
ATTN: Dr. Wallace Chintz
Associate Professor of ME
144. Cornell University
Department of Chemistry
Ithaca, New York 14850
ATTN: Professor Simon H. Bauer
145. Franklin Institute Research Laboratories
Philadelphia, Pennsylvania 19103
ATTN: Dr. G.P. Wachtell
146. George Washington University
Washington, D.C. 20052
ATTN: Dr. Robert Goulard
Dept. of Civil, Mechanical and
Environmental Engineering
147. George Washington University Library
Washington, D.C. 20006
ATTN: Reports Section
148. Georgia Institute of Technology
Atlanta, Georgia 30332
ATTN: Price Gilbert Memorial Library
149. Georgia Institute of Technology
School of Aerospace Engineering
Atlanta, Georgia 30332
ATTN: Dr. Ben T. Zinn
150. University of Illinois
Department of Energy Engineering
Box 4348
Chicago, Illinois 60680
ATTN: Professor Paul H. Chung
151. University of Illinois
College of Engineering
Department of Energy Engineering
Chicago, Illinois 60680
ATTN: Dr. D. S. Hacker
152. The Johns Hopkins University
Applied Physics Laboratory
Johns Hopkins Road
Laurel, Maryland 20810
ATTN: Chemical Propulsion
Information Agency
153. The Johns Hopkins University
Applied Physics Laboratory
Johns Hopkins Road
Laurel, Maryland 20810
ATTN: Document Librarian
154. The Johns Hopkins University
Applied Physics Laboratory
Johns Hopkins Road
Laurel, Maryland 20810
ATTN: Dr. A. A. Westenberg
155. University of Kentucky
Department of Mechanical Engineering
Lexington, Kentucky 40506
ATTN: Dr. Robert E. Peck
156. Massachusetts Institute of Technology
Department of Chemical Engineering
Cambridge, Massachusetts 02139
ATTN: Dr. Jack B. Howard
157. Massachusetts Institute of Technology
Libraries, Room 14 E-210
Cambridge, Massachusetts 02139
ATTN: Technical Reports
158. Massachusetts Institute of Technology
Room 10-408
Cambridge, Massachusetts 02139
ATTN: Engineering Technical Reports

FOREIGN INSTITUTIONS

159. Massachusetts Institute of Technology
Dept. of Mechanical Engineering
Room 3-350
Cambridge, Massachusetts 02139
ATTN: Dr. M. Cardillo
160. Massachusetts Institute of Technology
Dept. of Mechanical Engineering
Room 3-246
Cambridge, Massachusetts 02139
ATTN: Professor James Fay
161. Midwest Research Institute
425 Volker Boulevard
Kansas City, Missouri 64100
ATTN: Dr. T. A. Milne
162. New Mexico State University
Dept. of Mechanical Engineering
Box 3450
Las Cruces, New Mexico 88003
ATTN: Dr. Dennis M. Zallen
163. New York Institute of Technology
Wheatley Road
Old Westbury, New York 11568
ATTN: Dr. Fox
164. University of North Carolina
Periodicals and Serials Division
Drawer 870 Library
Chapel Hill, North Carolina 27514
ATTN: Mr. Stephen Berk
165. University of Notre Dame
Serials Record
Memorial Library
Notre Dame, Indiana 46556
ATTN: B. McIntosh
166. University of Notre Dame
College of Engineering
Notre Dame, Indiana 46556
ATTN: Dr. Stuart T. McComas
Assistant Dean for Research
and Special Projects
167. Ohio State University
Dept. of Chemical Engineering
140 West 19th Avenue
Columbus, Ohio 43210
ATTN: Dr. Robert S. Brodkey
168. The Pennsylvania State University
Room 207, Old Main Building
University Park, Pennsylvania 16802
ATTN: Office of Vice President
for Research

169. Princeton University
Dept. of Aerospace and Mechanical
Sciences
James Forrestal Campus
Princeton, New Jersey 08540
ATTN: Dr. Martin Summerfield
170. Princeton University
James Forrestal Campus Library
P.O. Box 710
Princeton, New Jersey 08540
ATTN: V. N. Simosko, Librarian
171. Rice University
Welch Professor of Chemistry
Houston, Texas 77001
ATTN: Dr. Joseph L. Franklin
172. University of Rochester
Dept. of Chemical Engineering
Rochester, New York 14627
ATTN: Dr. John R. Ferron
173. Stanford University
Dept. of Aeronautics and Astronautics
Stanford, California 94305
ATTN: Dr. Walter G. Vincenti
174. State University of New York - Buffalo
Dept. of Mechanical Engineering
228 Parker Engineering Building
Buffalo, New York 14214
ATTN: Dr. George Rudinger
175. Stevens Institute of Technology
Department of Mechanical Engineering
Castle Point Station
Hoboken, New Jersey 07030
ATTN: Professor Fred Sisto
176. University of Virginia
Department of Aerospace Engineering
School of Engineering and Applied Science
Charlottesville, Virginia 22901
ATTN: Dr. John E. Scott
177. University of Virginia
Science/Technology Information Center
Charlottesville, Virginia 22901
ATTN: Dr. Richard H. Austin
178. Yale University
Mason Laboratory
9 Hillhouse Avenue
New Haven, Connecticut 06520
ATTN: Professor Peter P. Wegener

179. A/S Kongsberg Vaapenfabrikk
Gas Turbine Division
3601 Konsber, NORWAY
ATTN: R.E. Stanley
Senior Aerodynamicist
180. Conservatoire National des Arts
et Metiers
292, Rue Saint-Martin
75141 Paris Cedex 03, FRANCE
ATTN: Professor J. Gossee
Chaire de Thermique
181. DFVLR-Forschungszentrum Göttingen
Institut für Strömungsmechanik
Abteilung Theoretische Gashydraulik
D-3400 Göttingen
Bunsenstrasse 10, GERMANY
ATTN: Professor Klaus Oswatitsch
182. Ecole Royale Militaire
30 Avenue de la Renaissance
Bruxelles B-1040, BELGIUM
ATTN: Professor Emile Tits
183. Fysisch Laboratorium
Fijksuniversiteit Utrecht
Sorbonnelaan, Utrecht,
THE NETHERLANDS
ATTN: Dr. F. Van der Valk
184. Imperial College
Department of Chemical Engineering
London SW7, ENGLAND
ATTN: Professor F. J. Weinberg
185. Imperial College of Science
and Technology
Department of Mechanical Engineering
Exhibition Road
London, SW7, ENGLAND
ATTN: Professor Gaydon
186. Imperial College of Science
and Technology
Department of Mechanical Engineering
Exhibition Road
London SW7, ENGLAND
ATTN: D. E. Spalding
- 187/1 Laboratoire de Mécanique des Fluides
36, Route de Dardilly, 36
B.P. No. 17
69130 Ecully, FRANCE
ATTN: G. Assassa

- 187/2 Laboratoire de Mecanique des Fluides
Ecole Centrale Lyonnaise
36, Route de Dardilly
69130 Ecully, FRANCE
ATTN: Dr. K. Papiliou
188. Ministry of Defense
Main Building, Room 2165
Whitehall Gardens
London SW1, ENGLAND
ATTN: Mr. L.D. Nicholson ED, idc
Vice Controller of Aircraft
Procurement Executive
189. Mitglied des Vorstands der Fried
Krump GmbH
43 Essen, Altendorferstrabe 103
GERMANY
ATTN: Professor Dr.-Ing.
Wilhelm Dettmering
190. National Aerospace (NLR)
Voorsterweg 31
Noord-Oost-Polder-Emmelord
THE NETHERLANDS
ATTN: Mr. F. Jaarsma
191. National Research Council
Division of Mechanical Engineering
Montreal Road, Ottawa
Ontario, CANADA K1A 0R6
ATTN: Dr. R.B. Whyte
192. Nissan Motor Co., LTD.
3-5-1, Momoi, Suginami-Ku
Tokyo, JAPAN 167
ATTN: Dr. Y. Toda
193. Norwegian Defense Research Establishment
Superintendent NDRE
P.O. Box 25
2007 Kjeller, NORWAY
ATTN: Mr. T. Krog
194. ONERA
Energie and Propulsion
29 Avenue de la Division Leclure
92 Chatillon sous Bagneux, FRANCE
ATTN: Mr. M. Barre
195. ONERA
Energie and Propulsion
29 Avenue de la Division Leclure
92 Chatillon sous Bagneux, FRANCE
ATTN: Mr. J. Fabri
196. ONERA
Energie and Propulsion
29 Avenue de la Division Leclure
92 Chatillon sous Bagneux, FRANCE
ATTN: Mr. Viaud
197. ONERA-DED
External Relations and Documentation
Department
29, Avenue de la Division Leclure
92320 Chatillon, sous Bagneux, FRANCE
ATTN: Mr. M. Salmon
198. Orta Dogu Teknik Universities
Mechanical Engineering Department
Ankara, TURKEY
ATTN: Professor H. Sezgen
199. Queen Mary College
Department of Mechanical Engineering
Thile Eld Road
London E1, ENGLAND
ATTN: Professor M. W. Thring
200. Rolls-Royce (1971) Limited
Derby Engine Division
P.O. Box 31
Derby DE2 8BJ
London, ENGLAND
ATTN: C. Freeman, Installation
Research Department
201. Rome University
Via Bradano 28
00199 Rome, ITALY
ATTN: Professor Gaetano Salvatore
202. Sener
Departamentao de Investigation
Km. 22.500 de la antigua carretera
Madrid - Barcelona, SPAIN
ATTN: Mr. J. T. Diez Roche
203. Service Technique Aeronautique Moteurs
4 Avenue de la Parte d'Issy
75753 Paris Cedex 15, FRANCE
ATTN: Mr. M. Pianko, Ing. en chef
204. The University of Sheffield
Dept. of Chemical Engineering
and Fuel Technology
Mappin Street, Sheffield S1 3JD
ENGLAND
ATTN: Dr. Norman Chigier
205. Sophia University
Science and Engineering Faculty
Kioi 7 Tokyo-Chiyoda JAPAN 102
ATTN: Professor M. Susuki
206. The University of Sydney
Dept. of Mechanical Engineering
N.S.W. 2006
Sydney, AUSTRALIA
ATTN: Professor R. W. Bilger
207. Technical University of Denmark
Fluid Mechanics Department
Building 404 2800 Lyngby
DK-DENMARK
ATTN: Professor K. Refslund
208. University of Leeds
Leeds, ENGLAND
ATTN: Professor Dixon-Lewis
209. Universite de Poitiers Laboratoire
D'energetique et de Detonique
(L.A. au C.N.R.S. No. 193)
ENSMA - 86034 Poitiers, FRANCE
ATTN: Professor N. Manson
210. University of Tokyo
Department of Reaction Chemistry
Faculty of Engineering
Bunkyo-ku
Tokyo, JAPAN 113
ATTN: Professor T. Hikita
211. Vrije Universiteit Brussel
Fac. Toeg. Wetensch.
A. Buyllaan 105
1050 Brussels, BELGIUM
ATTN: Ch. Hirsch
- PROJECT SQUID CONTRACTORS
1975-76 and 1976-77 (New)
212. AeroChem Research Laboratory, Inc.
Reaction Kinetics Group
P.O. Box 12
Princeton, New Jersey 08540
ATTN: Dr. Arthur Fontijn
213. Aeronautical Research Associates of
Princeton, Inc.
P.O. Box 2229
50 Washington Road
Princeton, New Jersey 08540
ATTN: Dr. Ashok K. Varma
214. California Institute of Technology
Div. of Engineering and
Applied Science
Mail Stop 205-50
Pasadena, California 91109
ATTN: Dr. Anatol Roshko
215. Case Western Reserve University
Div. of Fluid, Thermal and Aerospace
Sciences
Cleveland, Ohio 44106
ATTN: Dr. J.S. T'ien

216. Colorado State University
Engineering Research Center
Foothills Campus
Fort Collins, Colorado 80521
ATTN: Dr. Willy Z. Sadeh
217. General Electric Company
Corporate Research and Development
P.O. Box 8
Schenectady, New York 12301
ATTN: Dr. Marshall Lapp
218. Massachusetts Institute of Technology
Chemistry Department, Room 6-123
77 Massachusetts Avenue
Cambridge, Massachusetts 02139
ATTN: Dr. John Ross
219. Michigan State University
Department of Mechanical Engineering
East Lansing, Michigan 48824
ATTN: Dr. John Foss
220. Pennsylvania State University
Applied Research Laboratory
University Park, Pennsylvania 16802
ATTN: Dr. Edgar P. Bruce
221. Polytechnic Institute of New York
Department of Aerospace Engineering
and Applied Mechanics
Farmingdale, New York 11735
ATTN: Dr. Samuel Lederman
222. Southern Methodist University
Thermal and Fluid Sciences Center
Institute of Technology
Dallas, Texas 75275
ATTN: Dr. Roger L. Simpson
223. Stanford University
Mechanical Engineering Department
Stanford, California 94305
ATTN: Dr. James P. Johnston
224. Stanford University
Mechanical Engineering Department
Stanford, California 94305
ATTN: Dr. S. J. Kline
225. Stanford University
Mechanical Engineering Department
Stanford, California 94305
ATTN: Dr. Sidney Self
226. TRW Systems
Engineering Sciences Laboratory
One Space Park
Redondo Beach, California 90278
ATTN: Dr. J. E. Broadwell
227. United Technologies Research Center
400 Main Street
East Hartford, Connecticut 06108
ATTN: Mr. Franklin O. Carta
228. United Technologies REsearch Center
400 Main Street
East Hartford, Connecticut 06108
ATTN: Dr. Alan C. Eckbreth
229. University of California - San Diego
Department of Aerospace and
Mechanical Engineering
La Jolla, California 92037
ATTN: Dr. Paul Libby
230. University of Colorado
Department of Aerospace
Engineering Sciences
Boulder, Colorado 80304
ATTN: Dr. Mahinder S. Uberoi
231. University of Michigan
Department of Aerospace Engineering
Ann Arbor, Michigan 48105
ATTN: Dr. T. C. Adamson, Jr.
232. University of Michigan
Department of Aerospace Engineering
Ann Arbor, Michigan 48105
ATTN: Dr. Martin Sichel
233. University of Missouri - Columbia
Department of Chemistry
Columbia, Missouri 65201
ATTN: Dr. Anthony Dean
234. University of Southern California
Department of Aerospace Engineering
University Park
Los Angeles, California 90007
ATTN: Dr. F. K. Browand
235. University of Washington
Department of Mechanical Engineering
Seattle, Washington 98195
ATTN: Dr. F.B. Gessner
236. Virginia Polytechnic Institute and
State University
Mechanical Engineering Department
Blacksburg, Virginia 24601
ATTN: Dr. Walter F. O'Brien, Jr.
237. Virginia Polytechnic Institute and
State University
Mechanical Engineering Department
Blacksburg, Virginia 24061
ATTN: Dr. Hal L. Moses
238. Yale University
Engineering and Applied Science
Mason Laboratory
New Haven, Connecticut 06520
ATTN: Dr. John B. Fenn
239. School of Aeronautics and Astronautics
Grissom Hall
West Lafayette, Indiana 47907
ATTN: Library
240. School of Mechanical Engineering
Mechanical Engineering Building
West Lafayette, Indiana 47907
ATTN: Library
- 241-250. Purdue University Advisors

REPORT DOCUMENTATION PAGE		READ INSTRUCTIONS BEFORE COMPLETING FORM
1. REPORT NUMBER CIT-8-PU	2. GOVT ACCESSION NO.	3. RECIPIENT'S CATALOG NUMBER
4. TITLE (and Subtitle) An Experimental Investigation of Mixing in Two-Dimensional Turbulent Shear Flows with Applications to Diffusion-Limited Chemical Reactions		5. TYPE OF REPORT & PERIOD COVERED Technical Report 1977
7. AUTHOR(s) John Harrison Konrad		6. PERFORMING ORG. REPORT NUMBER
9. PERFORMING ORGANIZATION NAME AND ADDRESS Graduate Aeronautical Laboratories California Institute of Technology Pasadena, California		8. CONTRACT OR GRANT NUMBER(s) N00014-75-C-1143 NR-098-038
11. CONTROLLING OFFICE NAME AND ADDRESS Project SQUID, Chaffee Hall, Purdue University West Lafayette, Indiana 47907		10. PROGRAM ELEMENT, PROJECT, TASK AREA & WORK UNIT NUMBERS
14. MONITORING AGENCY NAME & ADDRESS (if different from Controlling Office) Office of Naval Research, Power Program Code 473, Department of the Navy Arlington, VA 22217		12. REPORT DATE January 1977
		13. NUMBER OF PAGES 130
		15. SECURITY CLASS. (of this report) Unclassified
		15a. DECLASSIFICATION/DOWNGRADING SCHEDULE
16. DISTRIBUTION STATEMENT (of this Report)		
17. DISTRIBUTION STATEMENT (of the abstract entered in Block 20, if different from Report)		
18. SUPPLEMENTARY NOTES		
19. KEY WORDS (Continue on reverse side if necessary and identify by block number) Mixing Shear Flows Diffusion - Limited Flows Chemical Reactions		
20. ABSTRACT (Continue on reverse side if necessary and identify by block number) The extent of molecular mixing in several two-dimensional free turbulent shear flows was measured using a concentration probe with a frequency response of 100 kHz and a spatial resolution of 0.1 mm. The flows investigated were (i) a shear layer in which the gases on either side of the layer are of unequal density, (ii) a shear layer in which the gases on either side of the layer are of equal density, and (iii) a wake in which the gases on either side of the wake are of unequal densities. The extent of mixing was measured as a function of Reynolds number for the first case. NOT PREP		

Unclassified

SECURITY CLASSIFICATION OF THIS PAGE(When Data Entered)

It was found that at a critical Reynolds number the extent of molecular mixing sharply increased (25%). Power spectral density curves of the concentration time histories also indicated a marked increase in the high frequency fluctuations above this Reynolds number. A shadowgraph investigation of this phenomenon revealed that three-dimensional Taylor-type vortices whose axes of rotation are basically in the flow direction exist in the flow in addition to the two-dimensional large structures previously observed. These Taylor vortices were found to be unstable above the critical Reynolds number and were producing the increase in molecular mixing. The growth and development of the two-dimensional large structures were found to be basically unaffected by this instability. It is proposed that the fully developed turbulence of shear flows is maintained by a combination of the development of the large structures and of the coupling between the large structures and these unstable Taylor vortices.

These data were also used to predict results for shear flows in which diffusion-limited chemical reactions have been incorporated.

Unclassified

SECURITY CLASSIFICATION OF THIS PAGE(When Data Entered)